Effects of Topography and Subsurface Irregularities on Strong Ground Motion(Dissertation_全文)

AUTHOR(S):

Kawase, Hiroshi

Effects of Topography and Subsurface Irregularities on Strong Ground Motion

Hiroshi Kawase

March, 1990

Effects of Topography and Subsurface Irregularities on Strong Ground Motion

Hiroshi Kawase

March, 1990

Acknowledgement

I wish to sincerely thank Keiiti Aki for his encouragement, helpful advice, and stimulative ideas in various aspects. I am grateful to have an opportunity to work with Kei, without which it would be impossible to complete this work. I wish to thank Ryoichiro Minai for his generous guidance and valuable advice in preparation of the dissertation. Gratitude is also extended to Tuneyoshi Nakamura and Kiyoshi Kaneta for their advice to improve the dissertation. I would like to express my deep gratitude to Takuji Kobori for his continuous encouragement from the beginning of my career.

I am grateful to Kojiro Irikura and Yuzo Shinozaki for their constructive criticism and suggestions. What I have learned through the discussions with them are immeasurable. Also thanks are given to Francisco J. Sánchez-Sesma for the discussions with him that were always stimuluous me greatly.

I thank Yorihiko Ohsaki and Hiroshi Yamahara for their understanding and support of my study. I have benefited greatly from collaboration and discussions with my colleagues in ORI, especially Toshiaki Sato, Kazuhiro Yoshida, and Yasuhiro Hayashi.

During my stay at USC, numerous discussions with Rafael Benites have enhanced my efforts. Also helps provided by Valerie Ferrazzini, Sandra Steasy, Syhhong Chang, and John McRaney are appreciated.

Most of this work was done while the author was a visiting scholar at the Department of Geological Sciences, University of Southern California on leave from Ohsaki Research Institute, Shimizu Corporation. This work was partially supported by the grand from the National Science Foundation of the United States. Part of the calculation is done by Cray X/MP in San Diego Supercomputer Center.

Abstract

The effects of topography and subsurface irregularities in a two-dimensional elastic half-space for various types of incident seismic waves are investigated. For this purpose the author proposes the discrete wavenumber boundary element method, in which the direct boundary element method is combined with the discrete wavenumber Green functions. The validity of the method is successfully tested with the previous results. The method is then applied to the actual topography and subsurface irregularities where severe damage concentration was observed during the recent major earthquakes in order to scrutinize possible explanations for the damage concentration.

First the proposed method is fully described for both direct boundary element method and the discrete wavenumber Green functions. Analytical evaluation of the element integration is presented. As a result of these combination, efficiency in computation, flexibility for boundary configurations, and the accuracy and the stability of the solution are achieved. It is easy to extend the method to the three-dimensional wave field. An economical technique of the Green function evaluation is also briefly mentioned.

Next the effects of surface irregularities in a two-dimensional half-space are studied for plane SH, SV, and P waves and a Rayleigh wave. The shapes of irregularities studied are cylindrical canyons and a ridge. The validity of the method is confirmed by comparing its results with published ones in frequency domain. The time histories of the surface motion are then calculated to understand the wave scattering phenomena for different types of incident waves. It is worth to note that in in-plane wave field Rayleigh waves carry significant portion of energy along the free-surface, but that in anti-plane wave field the direct and reflected waves play a major role. Also the author points out the importance of time-domain solution which provide us a complete picture of complicated physical process of wave scattering.

Then the DWBEM is applied to the actual ground problem in which heavy damage concentration was observed during the Whittier Narrows, California earth-

quake of 1987. It is intended to show the possibility that this anomalous damage concentration is due to the amplification by the topographic irregularity when SV waves are near-critical incidence. The author calculates the response of a two-dimensional hill with the height 0.3 km and the width 2.4 km to i) a plane SV wave with a nearly critical angle of incidence, ii) a horizontal line force, iii) a Haskell-type 2D dislocation source, and iv) a Bouchon-type 2D multiple crack source. The results show that the amplification due to the hill relative to the flat surface is more than 1.5 for all four sources. Since this amplification is nearly independent of the source type and spectrum, it is concluded that the combined effect of the topographic irregularity and critically incident SV waves might be responsible for the concentration of damage observed during the Whittier Narrows earthquake.

Finally responses of soft basins are studied to understand the cause of very long duration observed in Mexico City during Michoacan, Mexico earthquake of 1985. First the author shows that the normal amplification effect of soft surface layers cannot explain the large spectral amplification observed in Mexico City and that such large amplification is due to the later part of the observed seismogram which is very difficult to simulate. To see the effects of a deep basin structure two types of soft basin models that reflect the underground structure of Mexico City are considered. In either cases it is found that Love waves in anti-plane field or Rayleigh waves in in-plane field are generated at the edges of the basin and propagate back and forth inside the basin. Special amplification phenomena is observed in case of SV wave incidence with the critical angle. These deep basin models can create a later part of 20 seconds at most, whose amplitude is monotonically decreasing. The author tries further to prolong the duration by introducing another softer layer inside the basin. As a result of interaction between the deep basin and the soft surface layer, we have a later part of more than 80 seconds with large amplitude well separated from the main part. The author discusses the capability and limitations of the proposed model as a candidate that might cause the severe damage in Mexico City.

As a conclusion it is proved that the proposed method is powerful enough to solve various kinds of seismic wave scattering problems with topography and subsurface irregularities for various kinds of incident waves. From the results of

simulation analyses it is found that the geological settings around or underneath the sites might be responsible for the observed damage concentration. It should be emphasized that topographic or subsurface irregularities affect the responses in such a way that they not only amplify the response at certain frequencies but also prolong its duration. The latter effects cannot be overemphasized because of its importance to the nonlinear response of structures and hence to the structural damage in future earthquakes. It is concluded that the precise information on the geological structures of ground is crucial for the quantitative simulation of observed records and the definitive prediction for design-basis strong ground motions. Therefore the author recommends not only to proceed further the current programs of observation network scattered throughout the soft basin but also to gather information further on the geological structures of ground underneath as wide and deep as possible for the seismic hazard mitigation in future.

Contents

List of Figures

List of Tables

Chapter 1

Introduction

1.1 Objectives and scope

The correlation between the local geological characteristics and the severity of damage has been clearly observed in most of the earthquakes in the past. Researchers have been trying to establish quantitative relationship between certain geological parameters such as soil types or shear wave velocity of the surface layer and strength of the ground motion such as amplification factor or response spectra by which we can predict the expected input motion to the structure at a certain site and hence we can estimate potential damages for future earthquakes. However, their attempt has been mostly limited to the flat layer assumption. It usually works as far as the predominant frequency of the input motion is a primary concern. But it fails to capture the real physical process of seismic wave propagation generated by the laterally varying geological structures in the ground, in which complex wave reflection, refraction and diffraction are taking place. The effect of such surface and subsurface irregularities on the seismic response have been recognized recently from the observation of damage concentrated areas in several earthquakes.

One extreme example appeared in Mexico City during the Michoacan, Mexico earthquake 1985: in the soft-soil zone more than five hundreds of buildings collapsed while in the hill zone no buildings were damaged. It is of no doubt that the soft, lacstrine layers which covers the whole city except for the hill zone amplified the seismic waves considerably so that the maximum acceleration and velocity exceeded the limit of the structural resistance capacity. However, the strong motion record obtained during the earthquake showed another extraordinary feature. The duration of one station was more than three minutes and others on the lacstrine layers were also significantly longer than those on the hill. This long duration might also contribute the severe damages in the soft-soil zone since nonlinear deformation of

structures would be accumulated more and more as the input ground motion lasts longer. Several researchers have tried to explain what caused this long duration, but no one seems to succeed so far. As described in the next section, the previous methods of analysis may not be sufficient to study this long duration time of records observed in Mexico City because they lack the capability to calculate a very long time history with sufficient accuracy for arbitrary shape of irregularity.

Another example was obtained by the Whittier Narrow earthquake occurred on October 1, 1987 in Whittier, California. In this earthquake the damaged buildings and houses were concentrated to the small areas located several kilometers away from the epicenter. The most curious observation is that only the hillside area in Whittier was suffered from severe damages. This is extraordinary since usually hillside area is considered as the place where the level of the ground motion is lower than hilltop area or flat part with soft sediments. The difficulty of simulation in this Whittier case is not due to the long duration but the short predominant period of strong motion observed in the epicentral area.

Major purpose of this thesis is first to provide the method powerful enough to analyze various types of irregular structures in the ground for various types of incident waves both in time and frequency domain and then to study the wave scattering phenomena due to surface topography and lateral inhomogeneities of the ground by using the proposed method in order to scrutinize the possible causes of the extraordinary feature observed in the actual destructive earthquakes.

1.2 Review

In recent years, the effect of topography and subsurface inhomogeneities on the seismic response have been recognized widely as an important factor and extensive theoretical and experimental works have been carried out on the subject. So far, however, the clear delineation of such effects on the observed records have not been demonstrated, and theoretical works still occupy a main portion of these studies.

A pioneering work of such theoretical studies was done by Aki and Larner (1970), who proposed a practical method using discrete wavenumber representation of wave field under the so-called Rayleigh assumption. Trifunac (1971) presented the

exact solution for a semicircular alluvial valley subject to incident SH waves by using a Hankel function expansion. Both of these methods found wide applicability as evidenced by follow-up works carried out since then (e.g., for the Aki-Larner method, Bouchon, 1973; Bard and Bouchon, 1980a, 1980b; Bard, 1982; Bard and Bouchon, 1985; Kohketsu, 1987; and for the eigenfunction expansion method, Trifunac, 1973; Wong and Trifunac, 1974; Lee, 1982). However, these methods have well-known limitations, namely the Rayleigh ansatz error for the former and the restricted geometry of eigenfunctions for the latter.

Numerical techniques such as finite difference or finite element can represent unrestricted boundary configurations (e.g., Boore, 1970; Boore *et al.*, 1971; Boore, 1972; Drake, 1972; Ilan, 1977; Fuyuki and Matsumoto, 1980; Boore *et al.*, 1981; Ohtsuki and Harumi, 1983). However, one of the shortcomings of these methods is the bounded region of analysis. In order to avoid the influence of reflected waves at the artificial boundary, it becomes necessary to model a large region of the ground around an irregular part. This is expensive in terms of computational time, especially for the analysis of a large irregularity over a wide range of frequency and duration time.

Another method to solve the problem of surface or subsurface irregularities is the so-called ray method. A very simple example is the study on a dipping layer with fixed slope done by Ishii and Ellis (1970) who neglected the diffracted waves. After the development of more rigorous techniques such as the glorified optics or the Gaussian beam, their applications to the irregular ground have emerged (e.g., Hong and Helmberger, 1978; Nowack and Aki, 1984; Moczo *et al.*, 1987). Although these methods use approximations valid only in high frequency range, surprisingly good agreement with the results obtained by other method in relatively low frequency input is reported. Recently Benites and Aki (1989) developed a new method which uses the Gaussian beam in a different fashion, that is, to calculate the Green function in the boundary integral equation method. Since the numbers of multi-reflected rays grow explosively in the usual ray methods as time goes by, their approach may be advantageous in such a case.

To describe outgoing waves through an infinite body correctly, the Boundary Integral Equation Method (BIEM) is more suitable because it satisfies the radiation

condition implicitly. The first application of BIEM to the irregular ground analysis was done by Wong and Jennings (1975), who used the formulation proposed by Banaugh and Goldsmith (1963) to obtain the response of a canyon with an arbitrary shape. Since then a number of authors have investigated the effects of irregularities by using different types of integral equations and their numerical treatments (e.g., Kobori and Shinozaki, 1978; Sánchez-Sesma, 1978; Wong, 1979; Sánchez-Sesma and Esquivel, 1979; Dravinski, 1982; Wong, 1982; Sánchez-Sesma *et al.*, 1985; Dravinski and Mossessian, 1987). The author also applied the direct Boundary Element Method (BEM) to the subsurface inhomogeneity problems (Kawase *et al.*, 1982; Kawase *et al.*, 1985; Fukushima and Kawase, 1986; Kawase, 1987). The advantage of the direct BEM over the indirect BIEM is its excellent applicability and reliability without much precautions, since it expresses the boundary values directly through the Green function.

The biggest disadvantage of BIEM and BEM is the time-consuming effort to evaluate the Green function for a half-space since it cannot be expressed in a simple form except for the anti-plane case. The easiest way to overcome this difficulty is to use the Green function of an unbounded medium and to express the free-surface condition by using additional boundary elements. The problem with this alternative lies in the reliability of its results without pre-study, because the required size of the surface to simulate a half-space depends upon the frequency, the shape of irregularity, and the type of incident wave. This problem requires careful scrutiny.

The Green function for a half-space in frequency domain can be expressed in the form of an infinite integral with respect to the horizontal wavenumber. Most previous researchers who analyzed in-plane problems used this type of formulation (e.g., Wong, 1979, 1982; Dravinski 1982; Dravinski and Mossessian, 1987). However, in the process of the simulation for synthetic seismograms, Bouchon and Aki (1977) have shown that such infinite integrals can be transformed into infinite sums over discrete wavenumbers under the assumption of periodicity. As a result of this transformation, the evaluation of the Green function becomes much easier. The effect of adjacent fictitious sources can be eliminated using complex frequency and the corresponding time window correction as described in their paper.

In this thesis the author proposes the Discrete Wavenumber Boundary El-

ement Method (DWBEM) in which the direct BEM is combined with the discrete wavenumber Green function evaluated as infinite sums. The advantage of this method is its efficiency in computation and flexibility for boundary configurations. Moreover exact term-by-term evaluation is used for the element integrations which may contain singularity in the integrand. As a result, both the accuracy and the stability of the solution, especially in high frequency range, are assured. Because of its computational efficiency, accuracy, and stability for wide frequency range it becomes possible to calculate synthetic seismograms on the surface of topography or sediment-filled valley for very high frequency input-motions or for very long duration, as proved later in Chapters 3 to 5.

As one of the applications of the discrete wavenumber method, Bouchon (1985) and Campillo and Bouchon (1985) have proposed a method which can be considered as a kind of BIEM and looks very efficient. However, their method cannot treat steep boundaries without losing efficiency as shown by Bouchon (1985) for a semicircular canyon, because it discretizes the boundary in the horizontal direction with equal-sized elements, not along the boundary itself with variable-sized elements as in the DWBEM. The DWBEM allows us to discretize the boundaries of arbitrary shapes by the elements of arbitrary sizes as far as our computer resource permits.

As for the simulation analyses where a comparison of the calculated ground motions with the observed data is made, we only have several papers so far. Among them successful examples are rare.

Recently, Geli *et al.* (1988) made a review on the effect of ridges comparing observed data obtained by Davis and West (1973), Griffith and Bollinger (1979), and Tucker *et al.* (1984) with theoretical results calculated by Boore (1972), Smith (1975), Sills (1978), Bard (1982), and Zahradnik and Urban (1984). They found that the large amplification observed at some ridge crests is too large to be attributed to the simple topography effect considered in the simulation. As a possible cause of the discrepancy Bard and Tucker (1985) and Geli *et al.* (1988) suggested the combined effects of the topography with the low velocity layers and adjacent ridges, however, the simulation results in which these effects were taken into account still showed smaller amplification than the observed.

On the effect of a sediment-filled valley, Bard and Tucker (1987) made a com-

parison of theory and observation for the Chusal Valley, Garm, USSR. The transverse component of the velocity seismograms observed along the line perpendicular to the major axis of the valley showed in-phase motion and maximum amplitude at the valley center, which can be simulated by the theory. Another example of good agreement between observed and calculated motions was obtained by Ohtsuki *et al.* (1984) and Fukuwa *et al.* (1985) for the same very low velocity sediment-filled valley developed as a riverbed in Fujisawa City, Japan. The agreement is quite satisfactory both for time-histories and spectra of acceleration or displacement. However, both these two good examples are the case of a small-size valley whose lateral extent is the order of 100 meters. Also the velocity contrast between soft surface layers and the bedrock is relatively large. As a result the coherent motion inside the valley will be well developed (Bard and Bouchon, 1985), which makes the simulation easier.

For larger basin problems the quantitative simulation becomes much more difficult because

1. the observation network should be of large scale,
2. the geological structure beneath the surface should be collected in the large scale,
3. the incident wave type should be identified,
4. the incident wave motion should be defined correctly,
5. and the effects of source and path should be taken into account if the basin is in the near-field.

Recently, in consequence of the development of powerful computers, the simulation of large basin responses have been tried by a couple of researchers. Remarkably successful result is presented by Vidale and Helmberger (1988) who used a 2D finite difference method combined with the decomposed 3D point source to obtain the responses of the San Fernando Valley and Los Angeles Basin for the 1971 San Fernando earthquake. One important fact that should be noted to evaluate their results is that they used the deconvoluted source-time function and amplitude using one observation point at Santa Monica Mountains as a control point.

Another simulation using 2D finite difference method is done by Yamanaka *et al.* (1989) who calculate the displacement at Tokyo JMA station for the 1984 western

Nagano earthquake by the velocity model determined by the seismic refraction survey. Also Sato (1989) shows satisfactory result for the Osaka basin by using the thin layer element method. The above two papers compare the observed records at only one station in the basin so that it is still a question to answer whether the surface waves were developed and propagated inside the basin as those in the synthetics.

1.3 Organization

The main body of this study is organized in four chapters. Figure 1.1 shows conceptual flow of the study. The method proposed here, the DWBEM, is efficient in computation and accurate even at very high frequency so that the application becomes possible to the actual ground with the surface or subsurface irregularities where heavy damage concentration was observed during major earthquakes.

In Chapter 2, the method of analysis is fully described for both two and three dimensional wave field, though the numerical results presented in this thesis are limited to the two dimensional one. The analytical evaluation of the element integration is also described. The economical way to calculate the Green function by using the idea of the Hilbert transform is briefly shown.

In Chapter 3, first the validity of the proposed method is presented. Then the responses of canyons and a ridge in time domain are shown to understand the fundamental feature of the scattering phenomena by the topographic irregularities. The assumed incident waves are plane SH, SV, and P waves and a Rayleigh wave. The shape of irregularities considered here is very simple, however, we can learn a great deal from comparing the time domain responses due to different incident waves. A statement of caution on the interpretation of the spectral amplitude distribution often discussed in the literature is given.

In Chapter 4, the method is applied to the actual ground topography in order to explain the extraordinary damage concentration along the Puente Hills in Whittier during the Whittier Narrows, California earthquake of 1987. First the observed records are examined to find how we can use them. The nearest station to downtown Whittier where heaviest damage was concentrated is the station at 7215

Bright Ave. in Whittier. To find out the influence of a ten-story reinforced concrete building on the basement response, the system function analysis is made. Then the principal directions of observed records at twelve stations are compared with those of synthetics calculated by a simple fault model. A remarkable agreement between theory and observation suggests a relatively simple fault process. It also supports the hypothesis of SV wave dominance in Whittier. Next the response of a small hill whose geometry is taken from the actual geometry of Puente Hills which lies in the north of downtown Whittier. The sources assumed here are a plane SV wave, a horizontal line force, a Haskell-type fault, and a Bouchon-type fault. The time-domain responses as well as the peak amplitude distributions are shown for four different sources. A discussion on the other possible explanations is made at the end.

In Chapter 5, the method is applied to the large scale sediment-filled valley to explain the very long duration observed in Mexico City during the Michoacan, Mexico earthquake of 1985. First the incapability of 1D models to reproduce the later phases observed at the stations on the soft surface layer is presented. Then a deep basin structure is modeled whose material property is determined from available information on the Mexico City sediment. Since the size of irregularity is large and the duration of motion is long, the improved version of the DWBEM is used for more efficient computation. The incident wave considered here is plane SH, SV, and P waves and a Rayleigh wave with the shape of a Ricker wavelet for several different characteristic frequencies. A statement of caution on the length of the periodicity in the in-plane analysis is made. Finally a deep basin structure with a shallow surface layer is constructed to generate longer duration with larger amplitude. A discussion on the capability and the limitations of the proposed structure is made at the end.

In Chapter 6, the author summarizes the entire work and then makes his conclusion including the suggestion on the direction for further study on the subject.

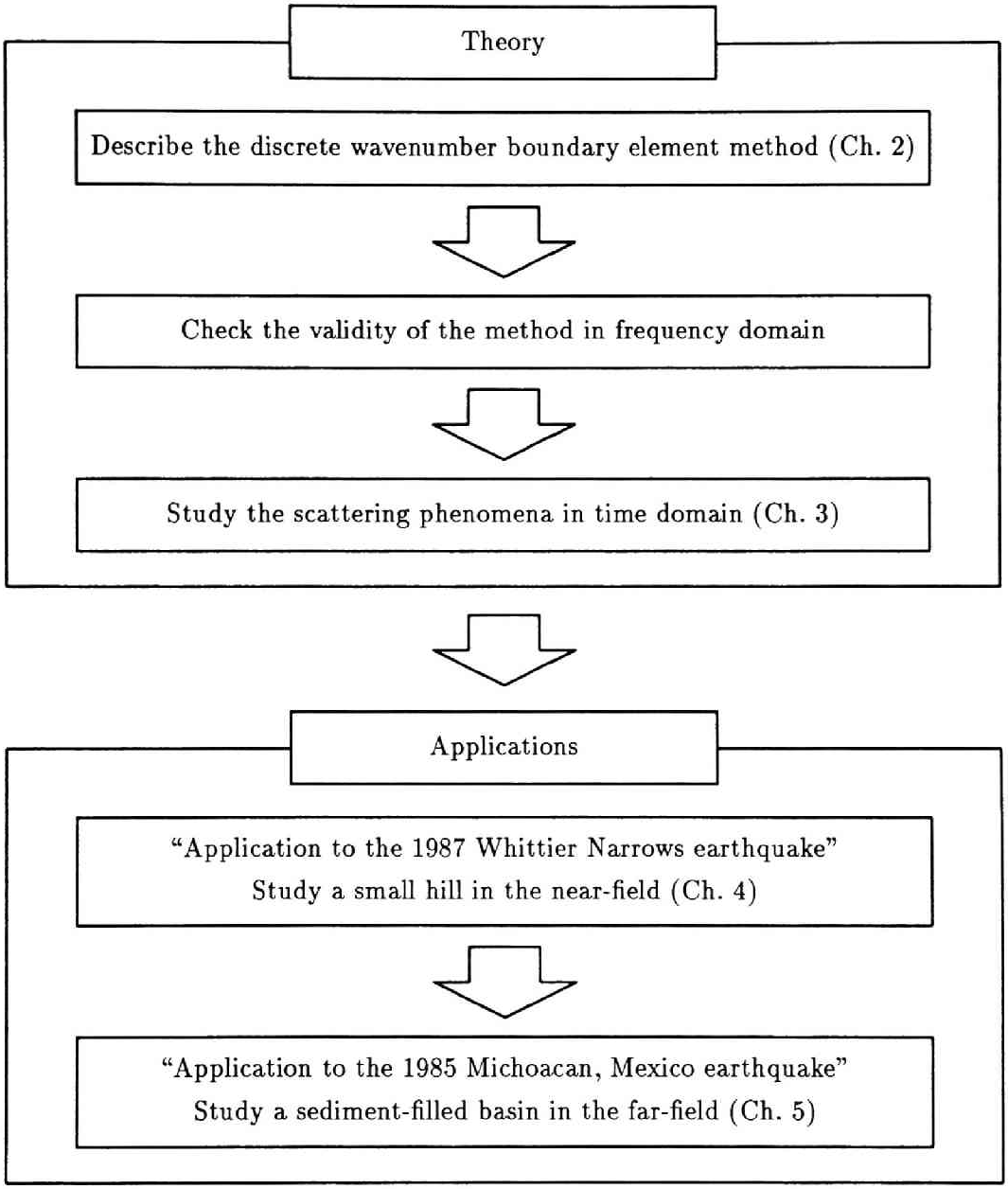

Figure 1.1: Conceptual flow of the study

Chapter 2

Method of Analysis

2.1 Description of the problem

Consider a general three-dimensional homogeneous isotropic elastic medium subject to a harmonic excitation of an incident wave. The coordinates used in this thesis are shown in Figure 2.1.

In this chapter the author introduces the Discrete Wavenumber Boundary Element Method (DWBEM) in which the direct BEM is combined with the discrete wavenumber Green function (Kawase, 1988). The advantage of this method is its efficiency in computation and flexibility for boundary configurations.

First the fundamental equations of BEM will be shown using the representation theorem. Then the Green function for full- and half-spaces in two and three dimensional wave fields by the discrete wavenumber method will be summarized. Most of the procedure to find the Green function follows the work done by Bouchon and Aki (1977). Analytical evaluation scheme of the element integration is also presented.

2.2 Direct boundary element method

First the fundamental equations of direct boundary element method will be shown using a representation theorem (Aki and Richards, 1980). Although these formulations can be found in earlier studies (e.g., Brebbia, 1978; Kawase *et al.*, 1982), they are shown for a complete description of the method used here.

The representation theorem for a general three-dimensional medium with the implicit time dependence $e^{i\omega t}$ ($i = \sqrt{-1}$ and ω a circular frequency) is,

$$u_i(\mathbf{x}^*) = \iiint_V G_{ji}(\mathbf{x};\mathbf{x}^*) \cdot f_j(\mathbf{x})\, dV$$

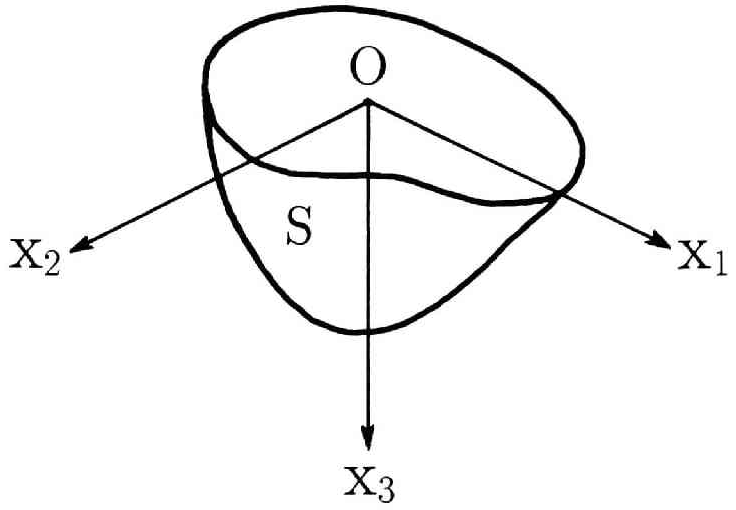

Figure 2.1: The system coordinates used in the analysis.

$$+ \iint_S \{G_{ji}(\mathbf{x};\mathbf{x}^*) \cdot t_j(\mathbf{x},\mathbf{n}) - H_{ji}(\mathbf{x},\mathbf{n};\mathbf{x}^*) \cdot u_j(\mathbf{x})\}\, dS\,. \qquad (2.1)$$

where, $u_i(\mathbf{x}^*)$ is i-th component of displacement at an arbitrary point $\mathbf{x}^*$, $f_j(\mathbf{x})$ is j-th component of a body-force at $\mathbf{x}$, $u_j(\mathbf{x})$ and $t_j(\mathbf{x},\mathbf{n})$ are j-th component of displacement and traction on the boundary S, $G_{ji}(\mathbf{x};\mathbf{x}^*)$ and $H_{ji}(\mathbf{x},\mathbf{n};\mathbf{x}^*)$ are the j-th components of the displacement and traction at $\mathbf{x}$ due to a point force in the i-th direction at $\mathbf{x}^*$, and $\mathbf{n}$ is a unit outward normal of the boundary S. Neglecting a body-force term equation (2.1) yields the fundamental equation of boundary integral representation as

$$u_i(\mathbf{x}^*) = \iint_S \{G_{ji}(\mathbf{x};\mathbf{x}^*) \cdot t_j(\mathbf{x},\mathbf{n}) - H_{ji}(\mathbf{x},\mathbf{n};\mathbf{x}^*) \cdot u_j(\mathbf{x})\}\, dS\,. \qquad (2.2)$$

In the direct BEM formulation, we need the expression in which a point $\mathbf{x}^*$ lies on the boundary S. This can be obtained by considering the limit $\mathbf{x}^* \to \mathbf{x}$ as

$$C \cdot u_i(\mathbf{x}^*) = \iint_S \{G_{ji}(\mathbf{x};\mathbf{x}^*) \cdot t_j(\mathbf{x},\mathbf{n}) - H_{ji}(\mathbf{x},\mathbf{n};\mathbf{x}^*) \cdot u_j(\mathbf{x})\}\, dS\,, \qquad (2.3)$$

where, C is a constant determined by the boundary shape around $\mathbf{x}^*$ and equal to $1/2$ in case of a smooth boundary. This equation shows that the boundary values are

directly related to each other through the Green function. Note that the integration contains a singularity in $G_{ii}(\mathbf{x};\mathbf{x}^*)$.

To solve this equation for arbitrary boundary shape and conditions, the discretization of both boundary shape and boundary values $u_j(\mathbf{x})$ and $t_j(\mathbf{x},\mathbf{n})$ should be introduced in the same manner as the finite element method (Brebbia, 1978). The simplest boundary element is a constant-value element with fixed slope, which allows to express the integral equation by means of

$$C \cdot u_i(\mathbf{x}_n) = \sum_{m=1}^{M} \tilde{G}_{ji}(m;\mathbf{x}_n) \cdot t_j(\mathbf{x}_m) - \sum_{m=1}^{M} \tilde{H}_{ji}(m;\mathbf{x}_n) \cdot u_j(\mathbf{x}_m)\,. \tag{2.4}$$

In this equation M is the total number of elements, $\mathbf{x}_n$ is the center of the n-th element, and $\tilde{G}_{ji}(m;\mathbf{x}_n)$ and $\tilde{H}_{ji}(m;\mathbf{x}_n)$ are the element integrations over the surface of the m-th element S_m expressed as

$$\tilde{G}_{ji}(m;\mathbf{x}_n) = \iint_{S_m} G_{ji}(\mathbf{x};\mathbf{x}_n)\,ds_m \tag{2.5}$$

$$\tilde{H}_{ji}(m;\mathbf{x}_n) = \iint_{S_m} H_{ji}(\mathbf{x},\mathbf{n};\mathbf{x}_n)\,ds_m\,. \tag{2.6}$$

By combining equations for different n we obtain the final simultaneous linear equation to be solved for the unknown boundary values. Then displacements at any point in the medium can be calculated by the discretized form of equation (2.2).

Consider next the problem with an incident wave (Figure 2.2**a**). Denoting the incoming wave field as $\mathbf{u}^{in}$ and the wave field scattered by the irregularity S as $\mathbf{u}^{sc}$, total wave field $\mathbf{u}$ is

$$\mathbf{u} = \mathbf{u}^{in} + \mathbf{u}^{sc}\,. \tag{2.7}$$

In case of a half-space problem the incoming wave field $\mathbf{u}^{in}$ means the incident wave field plus the reflected wave field at the free-surface. In case of a full-space problem or a surface-wave incidence, the incoming wave field means simply the incident wave field.

Since equation (2.3) can be applied to the wave field $\mathbf{u}^{sc}$ in the region outside of the boundary S (Figure 2.2**b**), we have

$$C \cdot u_i^{sc}(\mathbf{x}^*) = \iint_S \{G_{ji}(\mathbf{x};\mathbf{x}^*) \cdot t_j^{sc}(\mathbf{x},\mathbf{n}) - H_{ji}(\mathbf{x},\mathbf{n};\mathbf{x}^*) \cdot u_j^{sc}(\mathbf{x})\}\,dS\,. \tag{2.8}$$

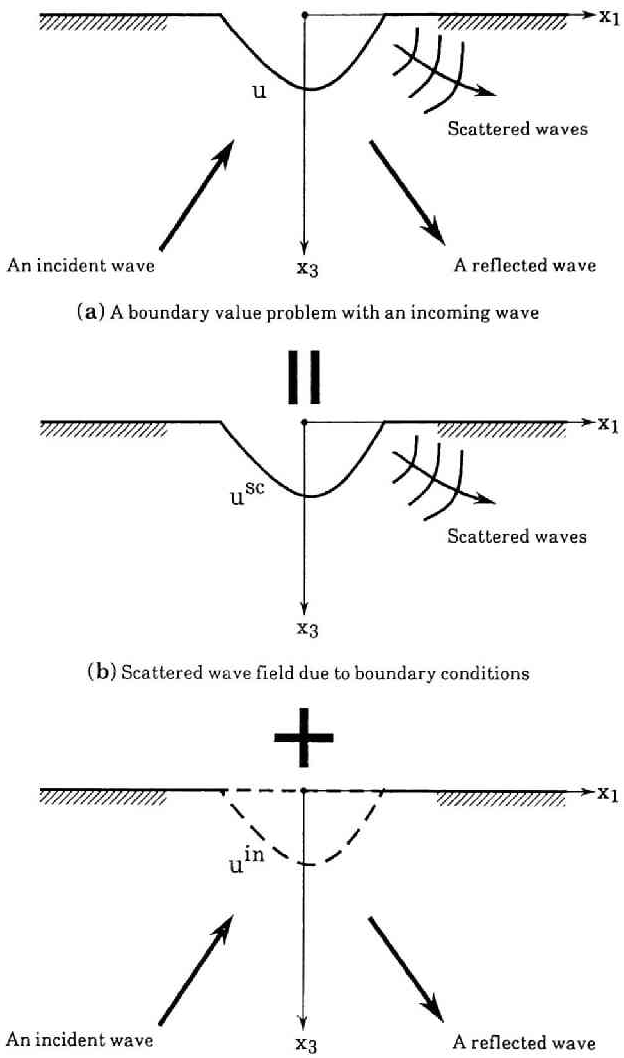

Figure 2.2: The conceptual schemes for an incident wave analysis. The solution for a boundary value problem with an incoming wave (a) can be considered as the sum of the scattered wave field (b) and an incoming wave field (c). A problem of a canyon in a half-space is taken as an example.

On the other hand, the incoming wave field should satisfy the equation

$$C^{(-)} \cdot u_i^{in}(\mathbf{x}^*) = \iint_S \{G_{ji}(\mathbf{x}\,;\mathbf{x}^*) \cdot t_j^{in}(\mathbf{x}, \mathbf{n}^{(-)}) - H_{ji}(\mathbf{x}, \mathbf{n}^{(-)}\,;\mathbf{x}^*) \cdot u_j^{in}(\mathbf{x})\}\, dS\,, \quad (2.9)$$

because it should satisfy the equation of motion and therefore the boundary values $\mathbf{u}^{in}(\mathbf{x})$ and $\mathbf{t}^{in}(\mathbf{x}, \mathbf{n}^{(-)})$ should satisfy the boundary integral equation for the area enclosed by the boundary S (Figure 2.2**c**). Since the outward normal of this enclosed area $\mathbf{n}^{(-)}$ is opposite to the original $\mathbf{n}$, traction components in the integrand $t_j^{in}(\mathbf{x}, \mathbf{n}^{(-)})$ and $H_{ji}(\mathbf{x}, \mathbf{n}^{(-)}\,;\mathbf{x}^*)$ should be $-t_j^{in}(\mathbf{x}, \mathbf{n})$ and $-H_{ji}(\mathbf{x}, \mathbf{n}\,;\mathbf{x}^*)$. For the same reason a constant $C^{(-)}$ should be $(1 - C)$.

From these two equations and equation (2.7) we obtain the BEM equation for an incident wave analysis in the following simple form

$$\begin{aligned} C \cdot u_i(\mathbf{x}^*) &= \iint_S \{G_{ji}(\mathbf{x}\,;\mathbf{x}^*) \cdot t_j(\mathbf{x}, \mathbf{n}) - H_{ji}(\mathbf{x}, \mathbf{n}\,;\mathbf{x}^*) \cdot u_j(\mathbf{x})\}\, dS \\ &+ u_i^{in}(\mathbf{x}^*)\,. \end{aligned} \quad (2.10)$$

This equation shows that the displacement distribution along the boundary $u_i^{in}(\mathbf{x}^*)$ is enough to solve any kind of incident wave problems. After obtaining all the unknown boundary values, however, we also need the traction distribution along the boundary $t_i^{in}(\mathbf{x}^*, \mathbf{n})$ to calculate the response at an arbitrary point because the integral equation for the scattering wave field should be used:

$$\begin{aligned} u_i(\mathbf{x}^*) &= \iint_S [G_{ji}(\mathbf{x}\,;\mathbf{x}^*) \cdot \{t_j(\mathbf{x}, \mathbf{n}) - t_j^{in}(\mathbf{x}, \mathbf{n})\} \\ &\qquad - H_{ji}(\mathbf{x}, \mathbf{n}\,;\mathbf{x}^*) \cdot \{u_j(\mathbf{x}) - u_j^{in}(\mathbf{x})\}]\, dS \\ &+ u_i^{in}(\mathbf{x}^*)\,. \end{aligned} \quad (2.11)$$

If other regions exist whose material properties are different from the exterior region, as is the case of a sediment-filled valley, the problem can be solved by combining the boundary integral equation for the exterior region with those for interior regions using the continuity condition of displacements and tractions. For example, in case that two homogeneous media are fully welded together along the whole boundary S as shown in Figure 2.3, we have the following BEM equation for the interior region (medium 1)

$$C^{(-)} \cdot u_i^{(1)}(\mathbf{x}^*) = \iint_S \{G_{ji}^{(1)}(\mathbf{x}\,;\mathbf{x}^*) \cdot t_j^{(1)}(\mathbf{x}, \mathbf{n}^{(-)}) - H_{ji}^{(1)}(\mathbf{x}, \mathbf{n}^{(-)}\,;\mathbf{x}^*) \cdot u_j^{(1)}(\mathbf{x})\}\, dS\,, \quad (2.12)$$

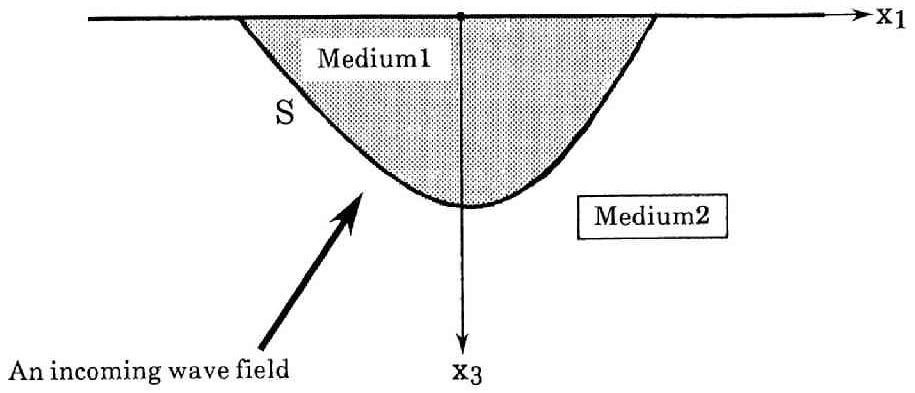

Figure 2.3: A problem of two coupled regions with an incident wave. The interior region **1** enclosed by the boundary S has different material properties from the exterior region **2** surrounding the boundary S.

and for the surrounding region (medium **2**)

$$C \cdot u_i^{(2)}(\mathbf{x}^*) = \iint_S \{G_{ji}^{(2)}(\mathbf{x};\mathbf{x}^*) \cdot t_j^{(2)}(\mathbf{x},\mathbf{n}) - H_{ji}^{(2)}(\mathbf{x},\mathbf{n};\mathbf{x}^*) \cdot u_j^{(2)}(\mathbf{x})\}\, dS + u_i^{in}(\mathbf{x}^*)\,, \tag{2.13}$$

where, the superscript $^{(m)}$ $(m = 1, 2)$ denotes the medium number. Equations (2.12) and (2.13) are combined using the continuity conditions

$$\begin{aligned} u_j^{(1)}(\mathbf{x}) &= u_j^{(2)}(\mathbf{x}) \\ t_j^{(1)}(\mathbf{x},\mathbf{n}^{(-)}) \left[= -t_j^{(1)}(\mathbf{x},\mathbf{n}) \right] &= -t_j^{(2)}(\mathbf{x},\mathbf{n}) \end{aligned} \tag{2.14}$$

along the boundary S.

2.3 The 2D discrete wavenumber Green function

Here the two-dimensional Green function for full- and half-spaces formulated by the discrete wavenumber method will be summarized. Most of the procedure to find the solutions follows the work done by Bouchon and Aki (1977). As stated by them, the solutions described here are the discrete version of those obtained first by Lamb (1904) for a surface line force.

In the in-plane (plane-strain) field it is convenient to express the wave field in terms of the compressional and rotational potentials ϕ and ψ with which displacements can be obtained as follows:

$$\begin{aligned} u_1 &= \frac{\partial \phi}{\partial x_1} - \frac{\partial \psi}{\partial x_3} \\ u_3 &= \frac{\partial \phi}{\partial x_3} + \frac{\partial \psi}{\partial x_1} \end{aligned} \tag{2.15}$$

The potentials due to a line source $Q_i e^{i\omega t}$ at a point (x_1^*, x_3^*) in an unbounded medium are,

$$\begin{aligned} \phi_1 &= \frac{Q_1}{4\pi {k_\beta}^2 \mu} \int_{-\infty}^{\infty} \frac{k}{\nu} e^{-i\nu|x_3 - x_3^*|} e^{-ik(x_1 - x_1^*)} dk \\ \psi_1 &= \frac{Q_1}{4\pi {k_\beta}^2 \mu} \int_{-\infty}^{\infty} -sgn(x_3 - x_3^*) e^{-i\gamma|x_3 - x_3^*|} e^{-ik(x_1 - x_1^*)} dk \,, \end{aligned} \tag{2.16}$$

for x_1-direction loading and

$$\begin{aligned} \phi_3 &= \frac{Q_3}{4\pi {k_\beta}^2 \mu} \int_{-\infty}^{\infty} sgn(x_3 - x_3^*) e^{-i\nu|x_3 - x_3^*|} e^{-ik(x_1 - x_1^*)} dk \\ \psi_3 &= \frac{Q_3}{4\pi {k_\beta}^2 \mu} \int_{-\infty}^{\infty} \frac{k}{\gamma} e^{-i\gamma|x_3 - x_3^*|} e^{-ik(x_1 - x_1^*)} dk \,, \end{aligned} \tag{2.17}$$

for x_3-direction loading. In these equations k is the horizontal wavenumber, μ is the shear modulus, and

$$\begin{aligned} \nu = \; & (k_\alpha^2 - k^2)^{1/2} \qquad Im\ \nu < 0 \\ \gamma = \; & (k_\beta^2 - k^2)^{1/2} \qquad Im\ \gamma < 0 \\ & k_\alpha = \omega/\alpha \qquad k_\beta = \omega/\beta \,, \end{aligned} \tag{2.18}$$

where α and β are the P and S wave velocities, respectively. The time factor $e^{i\omega t}$ is omitted there and thereafter. Discretizing the wave fields under the assumption of periodicity of line sources in x_1-direction, the equations (2.16) and (2.17) become

$$\begin{aligned} \phi_1 &= \frac{Q_1}{2Lk_\beta^2 \mu} \sum_{n=-\infty}^{\infty} \frac{k_n}{\nu_n} e^{-i\nu_n|x_3 - x_3^*|} e^{-ik_n(x_1 - x_1^*)} \\ \psi_1 &= \frac{Q_1}{2Lk_\beta^2 \mu} \sum_{n=-\infty}^{\infty} -sgn(x_3 - x_3^*) e^{-i\gamma_n|x_3 - x_3^*|} e^{-ik_n(x_1 - x_1^*)} \,, \end{aligned} \tag{2.19}$$

for x_1-direction loading and

$$\begin{aligned}\phi_3 &= \frac{Q_3}{2Lk_\beta{}^2\mu}\sum_{n=-\infty}^{\infty} sgn(x_3-x_3^*)e^{-i\nu_n|x_3-x_3^*|}e^{-ik_n(x_1-x_1^*)}\\ \psi_3 &= \frac{Q_3}{2Lk_\beta{}^2\mu}\sum_{n=-\infty}^{\infty}\frac{k_n}{\gamma_n}e^{-i\gamma_n|x_3-x_3^*|}e^{-ik_n(x_1-x_1^*)}\,,\end{aligned} \tag{2.20}$$

for x_3-direction loading, where L is an interval of periodicity and

$$\begin{aligned}\nu_n &= (k_\alpha{}^2-k_n{}^2)^{1/2} \qquad Im\ \nu_n<0\\ \gamma_n &= (k_\beta{}^2-k_n{}^2)^{1/2} \qquad Im\ \gamma_n<0.\\ k_n &= (2\pi/L)n\,.\end{aligned} \tag{2.21}$$

The discrete wavenumber method is called after these discrete wavenumbers, among which the horizontal discrete wavenumber k_n defines the rest in our case.

From the above results the Green functions of an unbounded medium $G_{ij}{}^F$, that is, the displacements due to periodic line sources are

$$\begin{aligned}G_{11}{}^F(\mathbf{x};\mathbf{x}^*) &= \frac{i}{2Lk_\beta{}^2\mu}\sum_{n=-\infty}^{\infty}\left\{-\frac{k_n{}^2}{\nu_n}E_{\nu_n}{}^F-\gamma_nE_{\gamma_n}{}^F\right\}E_{k_n}\\ G_{31}{}^F(\mathbf{x};\mathbf{x}^*) &= \frac{i}{2Lk_\beta{}^2\mu}\sum_{n=-\infty}^{\infty}S_{x_3}\left\{-k_nE_{\nu_n}{}^F+k_nE_{\gamma_n}{}^F\right\}E_{k_n}\\ G_{13}{}^F(\mathbf{x};\mathbf{x}^*) &= G_{31}{}^F(\mathbf{x};\mathbf{x}^*)\\ G_{33}{}^F(\mathbf{x};\mathbf{x}^*) &= \frac{i}{2Lk_\beta{}^2\mu}\sum_{n=-\infty}^{\infty}\left\{-\nu_nE_{\nu_n}{}^F-\frac{k_n{}^2}{\gamma_n}E_{\gamma_n}{}^F\right\}E_{k_n}\,,\end{aligned} \tag{2.22}$$

while the Green functions $H_{ij}{}^F$, that is, the tractions due to periodic line sources are

$$\begin{aligned}H_{11}{}^F(\mathbf{x},\mathbf{n};\mathbf{x}^*) &= \frac{1}{2Lk_\beta{}^2\mu}\sum_{n=-\infty}^{\infty}\left[\left\{\frac{k_n}{\nu_n}(2\nu_n{}^2-k_\beta{}^2)E_{\nu_n}{}^F-2k_n\gamma_nE_{\gamma_n}{}^F\right\}n_1\right.\\ &\quad\left.-S_{x_3}\left\{2k_n{}^2E_{\nu_n}{}^F+(2\gamma_n{}^2-k_\beta{}^2)E_{\gamma_n}{}^F\right\}n_3\right]E_{k_n}\\ H_{31}{}^F(\mathbf{x},\mathbf{n};\mathbf{x}^*) &= \frac{1}{2Lk_\beta{}^2\mu}\sum_{n=-\infty}^{\infty}\left[-S_{x_3}\left\{2k_n{}^2E_{\nu_n}{}^F+(2\gamma_n{}^2-k_\beta{}^2)E_{\gamma_n}{}^F\right\}n_1\right.\\ &\quad\left.+\left\{\frac{k_n}{\nu_n}(2k_n{}^2-k_\beta{}^2)E_{\nu_n}{}^F+2k_n\gamma_nE_{\gamma_n}{}^F\right\}n_3\right]E_{k_n}\end{aligned}$$

$$
\begin{aligned}
H_{13}{}^F(\mathbf{x},\mathbf{n};\mathbf{x}^*) &= \frac{1}{2Lk_\beta{}^2\mu}\sum_{n=-\infty}^{\infty}\Big[S_{x_3}\left\{(2\nu_n{}^2-k_\beta{}^2)E_{\nu_n}{}^F+2k_n{}^2E_{\gamma_n}{}^F\right\}n_1 \\
&\quad+\left\{-2k_n\nu_nE_{\nu_n}{}^F+\frac{k_n}{\gamma_n}(2\gamma_n{}^2-k_\beta{}^2)E_{\gamma_n}{}^F\right\}n_3\Big]E_{k_n} \\
H_{33}{}^F(\mathbf{x},\mathbf{n};\mathbf{x}^*) &= \frac{1}{2Lk_\beta{}^2\mu}\sum_{n=-\infty}^{\infty}\Big[\left\{-2k_n\nu_nE_{\nu_n}{}^F+\frac{k_n}{\gamma_n}(2\gamma_n{}^2-k_\beta{}^2)E_{\gamma_n}{}^F\right\}n_1 \\
&\quad+S_{x_3}\left\{(2k_n{}^2-k_\beta{}^2)E_{\nu_n}{}^F-2k_n{}^2E_{\gamma_n}{}^F\right\}n_3\Big]E_{k_n}. \qquad (2.23)
\end{aligned}
$$

In these equations following abbreviations are used

$$
\begin{aligned}
S_{x_3} &= sgn(x_3-x_3^*) \\
E_{k_n} &= e^{-ik_n(x_1-x_1^*)} \\
E_{\nu_n}{}^F &= e^{-i\nu_n|x_3-x_3^*|} \\
E_{\gamma_n}{}^F &= e^{-i\gamma_n|x_3-x_3^*|}. \qquad (2.24)
\end{aligned}
$$

As shown later in Section 5.3, we also have analytical form of the Green function for a full-space. We can use whichever we want according to our purpose and conditions, however, analytical evaluation of the element integration shown in section 2.5 is possible only for the discrete wavenumber solution.

In case of a half-space we need not only source potentials described above but also potentials which express the reflected P and S waves at the surface. The source potentials for x_1-direction loading are the same as equation (2.16). In addition to this we should introduce the reflected wave potentials ϕ_1' and ψ_1' with unknown coefficient A' and B' of the form

$$
\begin{aligned}
\phi_1' &= \frac{Q_1}{4\pi k_\beta{}^2\mu}\int_{-\infty}^{\infty}A'e^{-i\nu x_3}\,e^{-ik(x_1-x_1^*)}dk \\
\psi_1' &= \frac{Q_1}{4\pi k_\beta{}^2\mu}\int_{-\infty}^{\infty}B'e^{-i\gamma x_3}\,e^{-ik(x_1-x_1^*)}dk\,. \qquad (2.25)
\end{aligned}
$$

By applying the stress free boundary conditions at the surface for the sum of these two sets of potentials, we have the following relationship

$$
\begin{bmatrix} -2k\nu & -(2k^2-k_\beta{}^2) \\ -(2k^2-k_\beta{}^2) & 2k\gamma \end{bmatrix}\begin{pmatrix} A' \\ B' \end{pmatrix}=\begin{pmatrix} -2k^2e^{-i\nu x_3^*}+(2k^2-k_\beta{}^2)e^{-i\gamma x_3^*} \\ \frac{k}{\nu}(2k^2-k_\beta{}^2)e^{-i\nu x_3^*}+2k\gamma e^{-i\gamma x_3^*} \end{pmatrix}. \qquad (2.26)
$$

Solve this equation to get the unknown coefficients in the form

$$\begin{aligned} A' &= -\frac{1}{\Delta(k)}\left\{ -\frac{k}{\nu}\Gamma(k)e^{-i\nu x_3^*} + 4k\gamma(2k^2 - k_\beta{}^2)e^{-i\gamma x_3^*}\right\} \\ B' &= -\frac{1}{\Delta(k)}\left\{ -4k^2(2k^2 - k_\beta{}^2)e^{-i\nu x_3^*} - \Gamma(k)e^{-i\gamma x_3^*}\right\}, \end{aligned} \tag{2.27}$$

where,

$$\Delta(k) = +(2k^2 - k_\beta{}^2)^2 + 4k^2\nu\gamma \tag{2.28}$$

$$\Gamma(k) = -(2k^2 - k_\beta{}^2)^2 + 4k^2\nu\gamma\,. \tag{2.29}$$

The function $\Delta(k)$ is known as the Rayleigh function since the equation $\Delta(k) = 0$ gives the propagation velocity of Rayleigh waves. Substituting the result into equation (2.25), we have the final potentials which satisfy the boundary condition along the free-surface as,

$$\begin{aligned} \phi_1' &= \frac{Q_1}{4\pi k_\beta{}^2\mu}\int_{-\infty}^{\infty}\frac{1}{\Delta(k)}\left\{\frac{k}{\nu}\Gamma(k)e^{-i\nu(x_3+x_3^*)}\right. \\ &\quad \left. -4k\gamma(2k^2 - k_\beta{}^2)e^{-i(\nu x_3+\gamma x_3^*)}\right\}e^{-ik(x_1-x_1^*)}dk \\ \psi_1' &= \frac{Q_1}{4\pi k_\beta{}^2\mu}\int_{-\infty}^{\infty}\frac{1}{\Delta(k)}\left\{4k^2(2k^2 - k_\beta{}^2)e^{-i(\gamma x_3+\nu x_3^*)}\right. \\ &\quad \left. +\Gamma(k)e^{-i\gamma(x_3+x_3^*)}\right\}e^{-ik(x_1-x_1^*)}dk\,. \end{aligned} \tag{2.30}$$

Similarly, through the equation for unknown coefficients in case of a line source in x_3-direction

$$\begin{bmatrix} -2k\nu & -(2k^2 - k_\beta{}^2) \\ -(2k^2 - k_\beta{}^2) & 2k\gamma \end{bmatrix}\begin{pmatrix} A' \\ B' \end{pmatrix} = \begin{pmatrix} +2k\nu e^{-i\nu x_3^*} + \frac{k}{\gamma}(2k^2 - k_\beta{}^2)e^{-i\gamma x_3^*} \\ -(2k^2 - k_\beta{}^2)e^{-i\nu x_3^*} + 2k^2 e^{-i\gamma x_3^*} \end{pmatrix}, \tag{2.31}$$

we can obtain the reflected wave potentials ϕ_3' and ψ_3' as

$$\begin{aligned} \phi_3' &= \frac{Q_3}{4\pi k_\beta{}^2\mu}\int_{-\infty}^{\infty}\frac{1}{\Delta(k)}\left\{ -\Gamma(k)e^{-i\nu(x_3+x_3^*)}\right. \\ &\quad \left. -4k^2(2k^2 - k_\beta{}^2)e^{-i(\nu x_3+\gamma x_3^*)}\right\}e^{-ik(x_1-x_1^*)}dk \\ \psi_3' &= \frac{Q_3}{4\pi k_\beta{}^2\mu}\int_{-\infty}^{\infty}\frac{1}{\Delta(k)}\left\{ -4k\nu(2k^2 - k_\beta{}^2)e^{-i(\gamma x_3+\nu x_3^*)}\right. \\ &\quad \left. +\frac{k}{\gamma}\Gamma(k)e^{-i\gamma(x_3+x_3^*)}\right\}e^{-ik(x_1-x_1^*)}dk\,. \end{aligned} \tag{2.32}$$

Applying the same discretization for wavenumber k, those equations will provide the discrete wavenumber Green functions in a homogeneous half-space ${G_{ij}}^H$ as shown below:

$$
\begin{aligned}
{G_{11}}^H(\mathbf{x};\mathbf{x}^*) &= \frac{i}{2L{k_\beta}^2\mu}\sum_{n=-\infty}^{\infty}\Bigg[-\frac{{k_n}^2}{\nu_n}{E_{\nu_n}}^F-\gamma_n{E_{\gamma_n}}^F \\
&\quad -\frac{{k_n}^2\Gamma(k_n)}{\nu_n\Delta(k_n)}{E_{\nu_n\nu_n}}^H+\frac{4{k_n}^2\gamma_n(2{k_n}^2-{k_\beta}^2)}{\Delta(k_n)}{E_{\gamma_n\nu_n}}^H \\
&\quad +\frac{4{k_n}^2\gamma_n(2{k_n}^2-{k_\beta}^2)}{\Delta(k_n)}{E_{\nu_n\gamma_n}}^H+\frac{\gamma_n\Gamma(k_n)}{\Delta(k_n)}{E_{\gamma_n\gamma_n}}^H\Bigg]E_{k_n} \\
{G_{31}}^H(\mathbf{x};\mathbf{x}^*) &= \frac{i}{2L{k_\beta}^2\mu}\sum_{n=-\infty}^{\infty}\Bigg[S_{x_3}\{-k_n{E_{\nu_n}}^F+k_n{E_{\gamma_n}}^F\} \\
&\quad -\frac{k_n\Gamma(k_n)}{\Delta(k_n)}{E_{\nu_n\nu_n}}^H-\frac{4k_n^3(2{k_n}^2-{k_\beta}^2)}{\Delta(k_n)}{E_{\gamma_n\nu_n}}^H \\
&\quad +\frac{4k_n\nu_n\gamma_n(2{k_n}^2-{k_\beta}^2)}{\Delta(k_n)}{E_{\nu_n\gamma_n}}^H-\frac{k_n\Gamma(k_n)}{\Delta(k_n)}{E_{\gamma_n\gamma_n}}^H\Bigg]E_{k_n} \\
{G_{13}}^H(\mathbf{x};\mathbf{x}^*) &= \frac{i}{2L{k_\beta}^2\mu}\sum_{n=-\infty}^{\infty}\Bigg[S_{x_3}\{-k_n{E_{\nu_n}}^F+k_n{E_{\gamma_n}}^F\} \\
&\quad +\frac{k_n\Gamma(k_n)}{\Delta(k_n)}{E_{\nu_n\nu_n}}^H-\frac{4k_n\nu_n\gamma_n(2{k_n}^2-{k_\beta}^2)}{\Delta(k_n)}{E_{\gamma_n\nu_n}}^H \\
&\quad +\frac{4k_n^3(2{k_n}^2-{k_\beta}^2)}{\Delta(k_n)}{E_{\nu_n\gamma_n}}^H+\frac{k_n\Gamma(k_n)}{\Delta(k_n)}{E_{\gamma_n\gamma_n}}^H\Bigg]E_{k_n} \\
{G_{33}}^H(\mathbf{x};\mathbf{x}^*) &= \frac{i}{2L{k_\beta}^2\mu}\sum_{n=-\infty}^{\infty}\Bigg[-\nu_n{E_{\nu_n}}^F-\frac{{k_n}^2}{\gamma_n}{E_{\gamma_n}}^F \\
&\quad +\frac{\nu_n\Gamma(k_n)}{\Delta(k_n)}{E_{\nu_n\nu_n}}^H+\frac{4{k_n}^2\nu_n(2{k_n}^2-{k_\beta}^2)}{\Delta(k_n)}{E_{\gamma_n\nu_n}}^H \\
&\quad +\frac{4{k_n}^2\nu_n(2{k_n}^2-{k_\beta}^2)}{\Delta(k_n)}{E_{\nu_n\gamma_n}}^H-\frac{{k_n}^2\Gamma(k_n)}{\gamma_n\Delta(k_n)}{E_{\gamma_n\gamma_n}}^H\Bigg]E_{k_n}\,, \qquad (2.33)
\end{aligned}
$$

where following abbreviations for a half-space are used

$$
\begin{aligned}
{E_{\nu_n\nu_n}}^H &= e^{-i\nu_n(x_3+x_3^*)} \\
{E_{\gamma_n\nu_n}}^H &= e^{-i(\gamma_n x_3+\nu_n x_3^*)} \\
{E_{\nu_n\gamma_n}}^H &= e^{-i(\nu_n x_3+\gamma_n x_3^*)} \\
{E_{\gamma_n\gamma_n}}^H &= e^{-i\gamma_n(x_3+x_3^*)}\,. \qquad (2.34)
\end{aligned}
$$

The Green functions of traction for a half-space can also be obtained from the resultant potentials but are omitted here.

The Green function for an anti-plane problem can be expressed in the same manner as described above using the discrete wavenumber method

$$G_{22}{}^{F}(\mathbf{x};\mathbf{x}^*) = \frac{i}{2Lk_\beta{}^2\mu}\sum_{n=-\infty}^{\infty}\left[-\frac{k_\beta{}^2}{\gamma_n}E_{\gamma_n}{}^{F}\right]E_{k_n} \tag{2.35}$$

$$G_{22}{}^{H}(\mathbf{x};\mathbf{x}^*) = \frac{i}{2Lk_\beta{}^2\mu}\sum_{n=-\infty}^{\infty}\left[-\frac{k_\beta{}^2}{\gamma_n}(E_{\gamma_n}{}^{F}+E_{\gamma_n\gamma_n}{}^{H})\right]E_{k_n}\,, \tag{2.36}$$

for a full-space and a half-space, respectively. However, the original integral can be evaluated analytically to yield

$$G_{22}{}^{F}(\mathbf{x};\mathbf{x}^*) = -\frac{i}{4\mu}H_0{}^{(2)}(k_\beta r) \tag{2.37}$$

$$G_{22}{}^{H}(\mathbf{x};\mathbf{x}^*) = -\frac{i}{4\mu}\left\{H_0{}^{(2)}(k_\beta r)+H_0{}^{(2)}(k_\beta r^*)\right\}\,, \tag{2.38}$$

where, $H_m^{(2)}(\cdot)$ is the Hankel function of the second kind and mth order, and

$$\begin{aligned} r &= \sqrt{(x_1-x_1^*)^2+(x_3-x_3^*)^2} \\ r^* &= \sqrt{(x_1-x_1^*)^2+(x_3+x_3^*)^2}\,. \end{aligned} \tag{2.39}$$

These analytical solutions are much easier to calculate so that the discrete wavenumber form of the Green functions in equation (2.36) will not be used unless one actually intends to solve a problem with periodic structures. Needless to say, coupling terms between x_1-direction and x_2-direction and x_2-direction and x_3-direction are all zero in the two-dimensional wave field.

2.4 The 3D discrete wavenumber Green function

Next the three-dimensional Green functions for a homogeneous full- and half-spaces formulated by the discrete wavenumber method will be summarized. Lamb (1904) presented the integral form of such solutions for a surface point force for the first time. The notation used here to derive the Green function follows that by Aki and Richards (1980).

In the three-dimensional field it is convenient to express the wave field in terms of the Helmholtz potentials Φ and Ψ with which displacements can be obtained as follows:

$$\mathbf{u} = \nabla \cdot \Phi + \nabla \times \Psi \tag{2.40}$$

The potentials due to a point source $Q_i e^{i\omega t}$ at a point (x_1^*, x_2^*, x_3^*) in an unbounded medium are then (the time factor is again omitted),

$$\begin{aligned}
\Phi_1 &= \frac{Q_1}{8\pi^2 k_\beta{}^2 \mu} \iint_{-\infty}^{\infty} \frac{k_1}{\nu} e^{-i\nu|x_3 - x_3^*|} e^{-ik_1(x_1 - x_1^*) - ik_2(x_2 - x_2^*)} dk_1 dk_2 \\
\Psi_1^{[1]} &= 0 \\
\Psi_1^{[2]} &= \frac{Q_1}{8\pi^2 k_\beta{}^2 \mu} \iint_{-\infty}^{\infty} -S_{x_3} e^{-i\gamma|x_3 - x_3^*|} e^{-ik_1(x_1 - x_1^*) - ik_2(x_2 - x_2^*)} dk_1 dk_2 \\
\Psi_1^{[3]} &= \frac{Q_1}{8\pi^2 k_\beta{}^2 \mu} \iint_{-\infty}^{\infty} \frac{k_2}{\gamma} e^{-i\gamma|x_3 - x_3^*|} e^{-ik_1(x_1 - x_1^*) - ik_2(x_2 - x_2^*)} dk_1 dk_2 ,
\end{aligned} \tag{2.41}$$

for x_1-direction loading,

$$\begin{aligned}
\Phi_2 &= \frac{Q_2}{8\pi^2 k_\beta{}^2 \mu} \iint_{-\infty}^{\infty} \frac{k_2}{\nu} e^{-i\nu|x_3 - x_3^*|} e^{-ik_1(x_1 - x_1^*) - ik_2(x_2 - x_2^*)} dk_1 dk_2 \\
\Psi_2^{[1]} &= \frac{Q_2}{8\pi^2 k_\beta{}^2 \mu} \iint_{-\infty}^{\infty} S_{x_3} e^{-i\gamma|x_3 - x_3^*|} e^{-ik_1(x_1 - x_1^*) - ik_2(x_2 - x_2^*)} dk_1 dk_2 \\
\Psi_2^{[2]} &= 0 \\
\Psi_2^{[3]} &= \frac{Q_2}{8\pi^2 k_\beta{}^2 \mu} \iint_{-\infty}^{\infty} -\frac{k_1}{\gamma} e^{-i\gamma|x_3 - x_3^*|} e^{-ik_1(x_1 - x_1^*) - ik_2(x_2 - x_2^*)} dk_1 dk_2 ,
\end{aligned} \tag{2.42}$$

for x_2-direction loading, and

$$\begin{aligned}
\Phi_3 &= \frac{Q_3}{8\pi^2 k_\beta{}^2 \mu} \iint_{-\infty}^{\infty} S_{x_3} e^{-i\nu|x_3 - x_3^*|} e^{-ik_1(x_1 - x_1^*) - ik_2(x_2 - x_2^*)} dk_1 dk_2 \\
\Psi_3^{[1]} &= \frac{Q_3}{8\pi^2 k_\beta{}^2 \mu} \iint_{-\infty}^{\infty} \frac{k_2}{\gamma} e^{-i\gamma|x_3 - x_3^*|} e^{-ik_1(x_1 - x_1^*) - ik_2(x_2 - x_2^*)} dk_1 dk_2 \\
\Psi_3^{[2]} &= \frac{Q_3}{8\pi^2 k_\beta{}^2 \mu} \iint_{-\infty}^{\infty} \frac{k_1}{\gamma} e^{-i\gamma|x_3 - x_3^*|} e^{-ik_1(x_1 - x_1^*) - ik_2(x_2 - x_2^*)} dk_1 dk_2 \\
\Psi_3^{[3]} &= 0 .
\end{aligned} \tag{2.43}$$

for x_3-direction loading, where k_1 and k_2 are the horizontal wavenumbers in x_1- and x_2-directions and

$$\begin{aligned} \nu &= (k_\alpha{}^2 - k_1{}^2 - k_2{}^2)^{1/2} \qquad Im\ \nu < 0 \\ \gamma &= (k_\beta{}^2 - k_1{}^2 - k_2{}^2)^{1/2} \qquad Im\ \gamma < 0\,. \end{aligned} \tag{2.44}$$

Discretizing the wave field in x_1- and x_2-directions, we can transform these integrals into double infinite summations as

$$\begin{aligned} \Phi_1 &= \frac{Q_1}{2L_1L_2k_\beta{}^2\mu} \sum_{n=-\infty}^{\infty}\sum_{m=-\infty}^{\infty} \frac{k_n}{\nu_{nm}} E^F_{\nu_{nm}} E_{k_nk_m} \\ \Psi_1{}^{[1]} &= 0 \\ \Psi_1{}^{[2]} &= \frac{Q_1}{2L_1L_2k_\beta{}^2\mu} \sum_{n=-\infty}^{\infty}\sum_{m=-\infty}^{\infty} -S_{x_3} E^F_{\gamma_{nm}} E_{k_nk_m} \\ \Psi_1{}^{[3]} &= \frac{Q_1}{8\pi^2k_\beta{}^2\mu} \sum_{n=-\infty}^{\infty}\sum_{m=-\infty}^{\infty} \frac{k_m}{\gamma_{nm}} E^F_{\gamma_{nm}} E_{k_nk_m} \end{aligned} \tag{2.45}$$

for x_1-direction loading,

$$\begin{aligned} \Phi_2 &= \frac{Q_2}{2L_1L_2k_\beta{}^2\mu} \sum_{n=-\infty}^{\infty}\sum_{m=-\infty}^{\infty} \frac{k_m}{\nu_{nm}} E^F_{\nu_{nm}} E_{k_nk_m} \\ \Psi_2{}^{[1]} &= \frac{Q_1}{2L_1L_2k_\beta{}^2\mu} \sum_{n=-\infty}^{\infty}\sum_{m=-\infty}^{\infty} S_{x_3} E^F_{\gamma_{nm}} E_{k_nk_m} \\ \Psi_2{}^{[2]} &= 0 \\ \Psi_2{}^{[3]} &= \frac{Q_1}{2L_1L_2k_\beta{}^2\mu} \sum_{n=-\infty}^{\infty}\sum_{m=-\infty}^{\infty} -\frac{k_n}{\gamma_{nm}} E^F_{\gamma_{nm}} E_{k_nk_m} \end{aligned} \tag{2.46}$$

for x_2-direction loading, and

$$\begin{aligned} \Phi_3 &= \frac{Q_3}{2L_1L_2k_\beta{}^2\mu} \sum_{n=-\infty}^{\infty}\sum_{m=-\infty}^{\infty} S_{x_3} E^F_{\nu_{nm}} E_{k_nk_m} \\ \Psi_3{}^{[1]} &= \frac{Q_3}{2L_1L_2k_\beta{}^2\mu} \sum_{n=-\infty}^{\infty}\sum_{m=-\infty}^{\infty} \frac{k_m}{\gamma_{nm}} E^F_{\gamma_{nm}} E_{k_nk_m} \\ \Psi_3{}^{[2]} &= \frac{Q_3}{2L_1L_2k_\beta{}^2\mu} \sum_{n=-\infty}^{\infty}\sum_{m=-\infty}^{\infty} \frac{k_n}{\gamma_{nm}} E^F_{\gamma_{nm}} E_{k_nk_m} \\ \Psi_3{}^{[3]} &= 0\,. \end{aligned} \tag{2.47}$$

for x_3-direction loading, where L_1 and L_2 are intervals of periodicity in x_1 and x_2 directions, and

$$\begin{aligned}
\nu_{nm} &= (k_\alpha{}^2 - k_n{}^2 - k_m{}^2)^{1/2} \qquad Im\ \nu_{nm} < 0 \\
\gamma_{nm} &= (k_\beta{}^2 - k_n{}^2 - k_m{}^2)^{1/2} \qquad Im\ \gamma_{nm} < 0 \\
k_n &= (2\pi/L_1)n \\
k_m &= (2\pi/L_2)m \\
E_{k_nk_m} &= e^{-ik_n(x_1-x_1{}^*)-ik_m(x_2-x_2{}^*)} \\
E^F_{\nu_{nm}} &= e^{-i\nu_{nm}|x_3-x_3{}^*|} \\
E^F_{\gamma_{nm}} &= e^{-i\gamma_{nm}|x_3-x_3{}^*|}\,.
\end{aligned} \tag{2.48}$$

From these discretized potentials the Green functions of an unbounded medium $G_{ij}{}^F$, that is, the displacements due to unit periodic point forces can be expressed as:

$$\begin{aligned}
G_{11}{}^F(\mathbf{x};\mathbf{x}^*) &= \frac{i}{2L_1L_2k_\beta{}^2\mu}\sum_{n=-\infty}^{\infty}\sum_{m=-\infty}^{\infty}\{-\frac{k_n{}^2}{\nu_{nm}}E^F_{\nu_{nm}} - \frac{\gamma_{nm}{}^2+k_m{}^2}{\gamma_{nm}}E^F_{\gamma_{nm}}\}E_{k_nk_m} \\
G_{21}{}^F(\mathbf{x};\mathbf{x}^*) &= \frac{i}{2L_1L_2k_\beta{}^2\mu}\sum_{n=-\infty}^{\infty}\sum_{m=-\infty}^{\infty}\{-\frac{k_nk_m}{\nu_{nm}}E^F_{\gamma_{nm}} - \frac{k_nk_m}{\gamma_{nm}}E^F_{\nu_{nm}}\}E_{k_nk_m} \\
G_{31}{}^F(\mathbf{x};\mathbf{x}^*) &= \frac{i}{2L_1L_2k_\beta{}^2\mu}\sum_{n=-\infty}^{\infty}\sum_{m=-\infty}^{\infty}S_{x_3}\{-k_nE^F_{\nu_{nm}} + k_nE^F_{\gamma_{nm}}\}E_{k_nk_m} \\
G_{12}{}^F(\mathbf{x};\mathbf{x}^*) &= G_{21}{}^F(\mathbf{x};\mathbf{x}^*) \\
G_{22}{}^F(\mathbf{x};\mathbf{x}^*) &= \frac{i}{L_1L_2k_\beta{}^2\mu}\sum_{n=-\infty}^{\infty}\sum_{m=-\infty}^{\infty}\{-\frac{k_m{}^2}{\nu_{nm}}E^F_{\nu_{nm}} - \frac{\gamma_{nm}{}^2+k_n{}^2}{\gamma_{nm}}E^F_{\gamma_{nm}}\}E_{k_nk_m} \\
G_{32}{}^F(\mathbf{x};\mathbf{x}^*) &= \frac{i}{2L^2k_\beta{}^2\mu}\sum_{n=-\infty}^{\infty}\sum_{m=-\infty}^{\infty}S_{x_3}\{-k_mE^F_{\nu_{nm}} + k_mE^F_{\gamma_{nm}}\}E_{k_nk_m} \\
G_{13}{}^F(\mathbf{x};\mathbf{x}^*) &= G_{31}{}^F(\mathbf{x};\mathbf{x}^*) \\
G_{23}{}^F(\mathbf{x};\mathbf{x}^*) &= G_{32}{}^F(\mathbf{x};\mathbf{x}^*) \\
G_{33}{}^F(\mathbf{x};\mathbf{x}^*) &= \frac{i}{L_1L_2k_\beta{}^2\mu}\sum_{n=-\infty}^{\infty}\sum_{m=-\infty}^{\infty}\{-\nu_{nm}E^F_{\nu_{nm}} - \frac{k_n{}^2+k_m{}^2}{\gamma_{nm}}E^F_{\gamma_{nm}}\}E_{k_nk_m}\,.
\end{aligned} \tag{2.49}$$

In case of a half-space we need reflected-wave potentials as in the two dimensional case. By applying the stress free boundary conditions at the surface we have

the following final form of the reflected-wave potentials:

$$
\begin{aligned}
\Phi_1' &= \frac{Q_1}{2L_1L_2{k_\beta}^2\mu}\sum_{n=-\infty}^{\infty}\sum_{m=-\infty}^{\infty}\frac{1}{\Delta(k_n,k_m)}\left\{\frac{k_n}{\nu_{nm}}\Gamma(k_n,k_m)E^H_{\nu_{nm}\nu_{nm}}\right.\\
&\quad\left.-4k_n\gamma_{nm}({k_\beta}^2-2{\gamma_{nm}}^2)E^H_{\nu_{nm}\gamma_{nm}}\right\}E_{k_nk_m}\\
{\Psi_1'}^{[1]} &= 0\\
{\Psi_1'}^{[2]} &= \frac{Q_1}{2L_1L_2{k_\beta}^2\mu}\sum_{n=-\infty}^{\infty}\sum_{m=-\infty}^{\infty}\frac{1}{\Delta(k_n,k_m)}\left\{4({k_n}^2+{k_m}^2)({k_\beta}^2-2{\gamma_{nm}}^2)E^H_{\gamma_{nm}\nu_{nm}}\right.\\
&\quad\left.+\Gamma(k_n,k_m)E^H_{\gamma_{nm}\gamma_{nm}}\right\}E_{k_nk_m}\\
{\Psi_1'}^{[3]} &= \frac{Q_1}{2L_1L_2{k_\beta}^2\mu}\sum_{n=-\infty}^{\infty}\sum_{m=-\infty}^{\infty}\frac{1}{\Delta(k_n,k_m)}\left\{4k_m\gamma_{nm}({k_\beta}^2-2{\gamma_{nm}}^2)E^H_{\gamma_{nm}\nu_{nm}}\right.\\
&\quad\left.+\frac{k_m}{\gamma_{nm}}\Lambda(k_n,k_m)E^H_{\gamma_{nm}\gamma_{nm}}\right\}E_{k_nk_m}\,,
\end{aligned}
\tag{2.50}
$$

for x_1-direction loading,

$$
\begin{aligned}
\Phi_2' &= \frac{Q_2}{2L_1L_2{k_\beta}^2\mu}\sum_{n=-\infty}^{\infty}\sum_{m=-\infty}^{\infty}\frac{1}{\Delta(k_n,k_m)}\left\{\frac{k_m}{\nu_{nm}}\Gamma(k_n,k_m)E^H_{\nu_{nm}\nu_{nm}}\right.\\
&\quad\left.-4k_m\gamma_{nm}({k_\beta}^2-2{\gamma_{nm}}^2)E^H_{\nu_{nm}\gamma_{nm}}\right\}E_{k_nk_m}\\
{\Psi_2'}^{[1]} &= \frac{Q_2}{2L_1L_2{k_\beta}^2\mu}\sum_{n=-\infty}^{\infty}\sum_{m=-\infty}^{\infty}\frac{1}{\Delta(k_n,k_m)}\left\{-4({k_n}^2+{k_m}^2)({k_\beta}^2-2{\gamma_{nm}}^2)E^H_{\gamma_{nm}\nu_{nm}}\right.\\
&\quad\left.-\Gamma(k_n,k_m)E^H_{\gamma_{nm}\gamma_{nm}}\right\}E_{k_nk_m}\\
{\Psi_2'}^{[2]} &= 0\\
{\Psi_2'}^{[3]} &= \frac{Q_2}{2L_1L_2{k_\beta}^2\mu}\sum_{n=-\infty}^{\infty}\sum_{m=-\infty}^{\infty}\frac{1}{\Delta(k_n,k_m)}\left\{-4k_n\gamma_{nm}({k_\beta}^2-2{\gamma_{nm}}^2)E^H_{\gamma_{nm}\nu_{nm}}\right.\\
&\quad\left.-\frac{k_n}{\gamma_{nm}}\Lambda(k_n,k_m)E^H_{\gamma_{nm}\gamma_{nm}}\right\}E_{k_nk_m}\,,
\end{aligned}
\tag{2.51}
$$

for x_2-direction loading, and

$$
\begin{aligned}
\Phi_3' &= \frac{Q_3}{2L_1L_2{k_\beta}^2\mu}\sum_{n=-\infty}^{\infty}\sum_{m=-\infty}^{\infty}\frac{1}{\Delta(k_n,k_m)}\left\{-\Gamma(k_n,k_m)E^H_{\nu_{nm}\nu_{nm}}\right.\\
&\quad\left.-4({k_n}^2+{k_m}^2)({k_\beta}^2-2{\gamma_{nm}}^2)E^H_{\nu_{nm}\gamma_{nm}}\right\}E_{k_nk_m}\\
{\Psi_3'}^{[1]} &= \frac{Q_3}{2L_1L_2{k_\beta}^2\mu}\sum_{n=-\infty}^{\infty}\sum_{m=-\infty}^{\infty}\frac{1}{\Delta(k_n,k_m)}\left\{4k_m\nu_{nm}({k_\beta}^2-2{\gamma_{nm}}^2)E^H_{\gamma_{nm}\nu_{nm}}\right.
\end{aligned}
$$

$$
\begin{aligned}
& -\frac{k_m}{\gamma_{nm}}\Gamma(k_n,k_m)E^{H}_{\gamma_{nm}\gamma_{nm}}\Big\} E_{k_nk_m} \\
\Psi_3^{'[2]} &= \frac{Q_3}{2L_1L_2{k_\beta}^2\mu}\sum_{n=-\infty}^{\infty}\sum_{m=-\infty}^{\infty}\frac{1}{\Delta(k_n,k_m)}\Big\{-4k_n\nu_{nm}({k_\beta}^2-2{\gamma_{nm}}^2)E^{H}_{\gamma_{nm}\nu_{nm}} \\
& +\frac{k_n}{\gamma_{nm}}\Gamma(k_n,k_m)E^{H}_{\gamma_{nm}\gamma_{nm}}\Big\} E_{k_nk_m} \\
\Psi_3^{'[3]} &= 0
\end{aligned}
\tag{2.52}
$$

for x_3-direction loading, where,

$$
\begin{aligned}
\Delta(k_n,k_m) &= +({k_\beta}^2-2{\gamma_{nm}}^2)^2+4\nu_{nm}\gamma_{nm}({k_n}^2+{k_m}^2) \\
\Gamma(k_n,k_m) &= -({k_\beta}^2-2{\gamma_{nm}}^2)^2+4\nu_{nm}\gamma_{nm}({k_n}^2+{k_m}^2) \\
\Lambda(k_n,k_m) &= +({k_\beta}^2-2{\gamma_{nm}}^2)^2+4\nu_{nm}\gamma_{nm}({k_\beta}^2+{\gamma_{nm}}^2) \\
E^{H}_{\nu_{nm}\nu_{nm}} &= e^{-i\nu_{nm}(x_3+x_3^*)} \\
E^{H}_{\gamma_{nm}\nu_{nm}} &= e^{-i(\gamma_{nm}x_3+\nu_{nm}x_3^*)} \\
E^{H}_{\nu_{nm}\gamma_{nm}} &= e^{-i(\nu_{nm}x_3+\gamma_{nm}x_3^*)} \\
E^{H}_{\gamma_{nm}\gamma_{nm}} &= e^{-i\gamma_{nm}(x_3+x_3^*)} \ .
\end{aligned}
\tag{2.53}
$$

Adding these reflected-wave potentials with the source potentials, we have the solution for a half-space which will provide the discrete wavenumber Green functions in a three-dimensional homogeneous half-space ${G_{ij}}^H$ and ${H_{ij}}^H$ as in the two dimensional case.

The above Green functions use the expression of the double Fourier transform over k_1 and k_2, which is similar to that of the so-called Dynamical Ground Compliance first obtained by Thomson and Kobori (1963). It is a natural consequence of the Cartesian coordinates we use. The three-dimensional Green functions in most of the previous studies (e.g., Apsel and Luco, 1983; Frazer and Gettrust, 1984) are expressed as the Hankel transform over the radial wavenumber k_r with the Bessel function by using the cylindrical coordinates. However, the Green functions expressed in the Cartesian coordinates are easier to evaluate the element integration analytically.

It should be noted that the Green functions in two-dimensional wave field can be easily obtained just by assuming $L_2 = 1$ and summing up terms for only

one wavenumber k_n. The solution is the Green function for a line source with common x_2-direction dependency $e^{-ik_m x_2}$ which can be used for the analysis of a two-dimensional irregularity subject to an incident plane wave with azimuthal angle (whose x_2-direction dependency should be the same). The two-dimensional Green function presented in the foregoing section is the special case where $m = 0$.

2.5 Element integration

In the direct BEM the element integrations in equations (2.5) and (2.6) are necessary. For the two-dimensional case these integrations become simply,

$$\tilde{G}_{ji}(m\,;\mathbf{x}_n) = \int_{-l/2}^{l/2} G_{ji}(\mathbf{x}\,;\mathbf{x}_n)\,ds_m \tag{2.54}$$

$$\tilde{H}_{ji}(m\,;\mathbf{x}_n) = \int_{-l/2}^{l/2} H_{ji}(\mathbf{x},\mathbf{n}\,;\mathbf{x}_n)\,ds_m\,, \tag{2.55}$$

where l and s_m are the length and the local coordinate of the m-th element, respectively. A line force is located at the center of the n-th element as illustrated in Figure 2.4. Since the discrete wavenumber Green function has separated dependency with respect to x_1 and x_3 coordinates, it is rather easy to evaluate these integrations analytically.

We shall consider two different cases depending on whether the integrand contains the absolute value term $\mid x_3 - x_3^* \mid$. First we consider the case that the integrand contains no absolute value term. Referring to equations (2.22), (2.23), and (2.33), we can write such an integration for the wavenumber k_n as a generic form

$$I_n = f(k_n) \int_{-l/2}^{l/2} e^{-i\eta_n(x_3 \pm x_3^*)} e^{-ik_n(x_1 - x_1^*)}\,ds_m\,, \tag{2.56}$$

where η_n represents either ν_n or γ_n. This stands for all the surface terms and the source terms if the source location in depth is outside of the range defined by the both ends of the element.

The global coordinates (x_1, x_3) are expressed by the local coordinate s_m as

$$\begin{aligned} x_1 &= x_1^c + n_3\,s_m \\ x_3 &= x_3^c - n_1\,s_m \end{aligned} \tag{2.57}$$

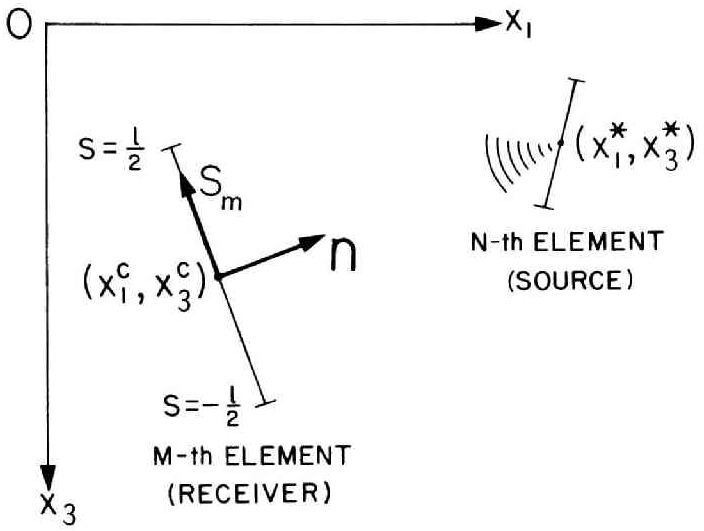

Figure 2.4: The local coordinate s_m used in the element integration. $\mathbf{n}$ and l are the outward normal and the length of the m-th element, respectively.

where (x_1^c, x_3^c) is the center of the element. Substituting these into equation (2.56) we have

$$\begin{aligned} I_n &= f(k_n) \int_{-l/2}^{l/2} e^{-i\eta_n(x_3^c - n_1 s_m \pm x_3^*)} e^{-ik_n(x_1^c + n_3 s_m - x_1^*)} \, ds_m \\ &= f(k_n)\, e^{-i\eta_n(x_3^c \pm x_3^*)}\, e^{-ik_n(x_1^c - x_1^*)} \int_{-l/2}^{l/2} e^{i(\eta_n n_1 - k_n n_3)s_m} \, ds_m \\ &= f(k_n)\, e^{-i\eta_n(x_3^c \pm x_3^*)}\, e^{-ik_n(x_1^c - x_1^*)} \frac{2}{-\eta n_1 + k_n n_3} \sin \frac{(-\eta n_1 + k_n n_3)l}{2} . \end{aligned} \tag{2.58}$$

Second is the case that the absolute value term with respect to x_3 coordinate $\mid x_3 - x_3^* \mid$ exists. It appears in the source terms only if the source location in depth is within the range of the element. In such a case x_3 dependency becomes (assuming $n_1 > 0$)

$$\mid x_3 - x_3^* \mid = \left\{ \begin{array}{ll} +x_3^c - n_1 s_m - x_3^* & \text{if } -l/2 \le s_m < (x_3^c - x_3^*)/n_1 \\ -x_3^c + n_1 s_m + x_3^* & \text{if } (x_3^c - x_3^*)/n_1 \le s_m \le l/2 . \end{array} \right\} \tag{2.59}$$

After several calculations we have the element integration of the form

$$
\begin{aligned}
I_n \;= -if(k_n)e^{-ik_n(x_1^c - x_1^*)} \;& \left[\left\{\frac{1}{\eta_n n_1 - k_n n_3} + \frac{1}{\eta_n n_1 + k_n n_3}\right\} e^{-ik_n(x_3^c - x_3^*)n_3/n_1}\right. \\
& - \frac{1}{\eta_n n_1 - k_n n_3}\, e^{-i(\eta_n n_1 - k_n n_3)l/2}\, e^{-i\eta_n(x_3^c - x_3^*)} \\
& \left. - \frac{1}{\eta_n n_1 + k_n n_3}\, e^{-i(\eta_n n_1 + k_n n_3)l/2}\, e^{+i\eta_n(x_3^c - x_3^*)}\right] .
\end{aligned}
\tag{2.60}
$$

The above analytical evaluation of the element integration is one of the advantages of the DWBEM because it eliminates difficulties associated with a singularity of the Green functions in case that the element includes the force (i.e., $n = m$). Also, this integration guarantees convergence with respect to the horizontal wavenumber due to the additional term of order k_n^{-1}. However, careful treatment may be necessary in the calculation process because each term in $f(k_n)$ has a tendency to increase with the wavenumber k_n although their sum will converge. A similar procedure appears in the response calculation for moving dislocation sources (Bouchon, 1978; Kawase and Aki, 1990).

The truncation of the infinite summation is decided by double thresholds, that is, an absolute value and a relative value. Each time the partial sum for the pre-defined number of wavenumbers (typically 16) is calculated, the absolute value of this partial sum as well as the relative value with respect to the total sum up to that time is checked. Calculation will continue until both of these values are smaller than the pre-defined value (typically 10^{-5}). Usually numbers of terms necessary to satisfy these conditions may range from 32 up to a few thousands.

As a final note on the discrete wavenumber Green function, an essential difference of the discrete wavenumber scheme from the approximated integration schemes should be mentioned. In the past many numerical integration schemes suitable for automatic computing were proposed (e.g., Press *et al.*, 1986). On the surface the discrete wavenumber sum looks just the same as a simple trapezoidal rule of integration provided that the integration will be continued until the integrand converges to zero. However, there exists an essential difference between them. In any numerical integration schemes we need to check the convergence in terms of the sampling rate. Too few sampling points result in an inaccurate value. Since it is impossible to know

the sufficient sampling rate in advance, we have to evaluate the integration at least twice to see the convergence. The more accuracy we demand, the more numbers of iteration we need. On the other hand, the discrete wavenumber Green function has its own physical meaning, that is, the response due to periodically-existing, infinite numbers of sources. The discrete wavenumber sum is, therefore, exact in terms of the sampling rate and so we need not to check the convergence as far as the periodicity length L is large enough to have all the arrivals from fictitious sources outside the time window (we need to check the convergence with respect to the summation, of course). Or we can use the discrete wavenumber boundary element method for problems with periodic structures. It is not necessary to eliminate the effects of fictitous structures in such cases. From mathematical point of view the periodicity of sources is interpreted as the result of aliasing (Bouchon and Aki, 1977).

In case of a three-dimensional problem, the same procedure described above can be applied to the double integrals for any triangular sub-elements.

2.6 Economical evaluation of the Green function

Even though the discrete wavenumber method is more efficient than conventional techniques, the convergence of the Green functions with respect to the horizontal wavenumber is still slow when vertical distance between the source and the receiver is small. Especially in three-dimension, the double infinite summation over two horizontal wavenumbers requires a heavy computational power. It is possible, however, to evaluate it more economically by just taking its imaginary part and reproducing the real part using the causality condition, because the convergence of the imaginary part is much faster than those of the real part (Kawase and Aki, 1989a). First the fundamental relationship between the real and imaginary parts in frequency domain that holds for any functions causal in time domain is presented.

Let $F(\omega)$ be the Fourier transform of a real time function $f(t)$, that is,

$$F(\omega) = \int_{-\infty}^{\infty} f(t) e^{-i\omega t}\, dt\,, \tag{2.61}$$

$$f(t) = \frac{1}{2\pi} \int_{-\infty}^{\infty} F(\omega) e^{i\omega t}\, d\omega\,. \tag{2.62}$$

Denoting $F_R(\omega)$ and $F_I(\omega)$ as the real and imaginary parts of $F(\omega)$, we have the

Table 2.1: Maximum wavenumbers to get convergence

z_R (depth)	0.0	0.001	0.01	0.1
Real part	16.0	7.6	10.5	2.1
Imaginary part	1.9	1.9	1.8	1.7

The parameters used here is the same as those for Figure 2.5 (complex frequency) except for the receiver depth z_R. The values are normalized by k_β. Convergence is checked for every 0.1 increment from 1.0 .

symmetricity relations $F_R(\omega) = F_R(-\omega)$ and $F_I(\omega) = -F_I(-\omega)$. Substituting these to equation (2.62) yields the following expression of the inverse Fourier transform

$$f(t) = \frac{1}{\pi}\left\{\int_0^\infty F_R(\omega)\cos\omega t\, d\omega - \int_0^\infty F_I(\omega)\sin\omega t\, d\omega\right\} . \tag{2.63}$$

Assuming that the time function $f(t)$ is zero for t < 0, we have

$$\int_0^\infty F_R(\omega)\cos\omega t\, d\omega = \int_0^\infty F_I(\omega)\sin\omega t\, d\omega \;\; ; \; t < 0. \tag{2.64}$$

Then the following equation holds for t > 0

$$\int_0^\infty F_R(\omega)\cos\omega t\, d\omega = -\int_0^\infty F_I(\omega)\sin\omega t\, d\omega \;\; ; \; t > 0. \tag{2.65}$$

Substituting this into equation (2.63), we finally obtain the time function for t > 0 expressed by only the real part

$$f(t) = \frac{1}{\pi}\int_{-\infty}^\infty F_R(\omega)e^{i\omega t}d\omega\,, \tag{2.66}$$

or the imaginary part

$$f(t) = \frac{i}{\pi}\int_{-\infty}^\infty F_I(\omega)e^{i\omega t}d\omega\,. \tag{2.67}$$

These are the specific expressions of the causality which leads to the well-known relationship between real and imaginary part as the Hilbert transform (Papoulis, 1962; Aki and Richards, 1980; Izumi *et al.*, 1988; Hayashi and Katsukura, 1990).

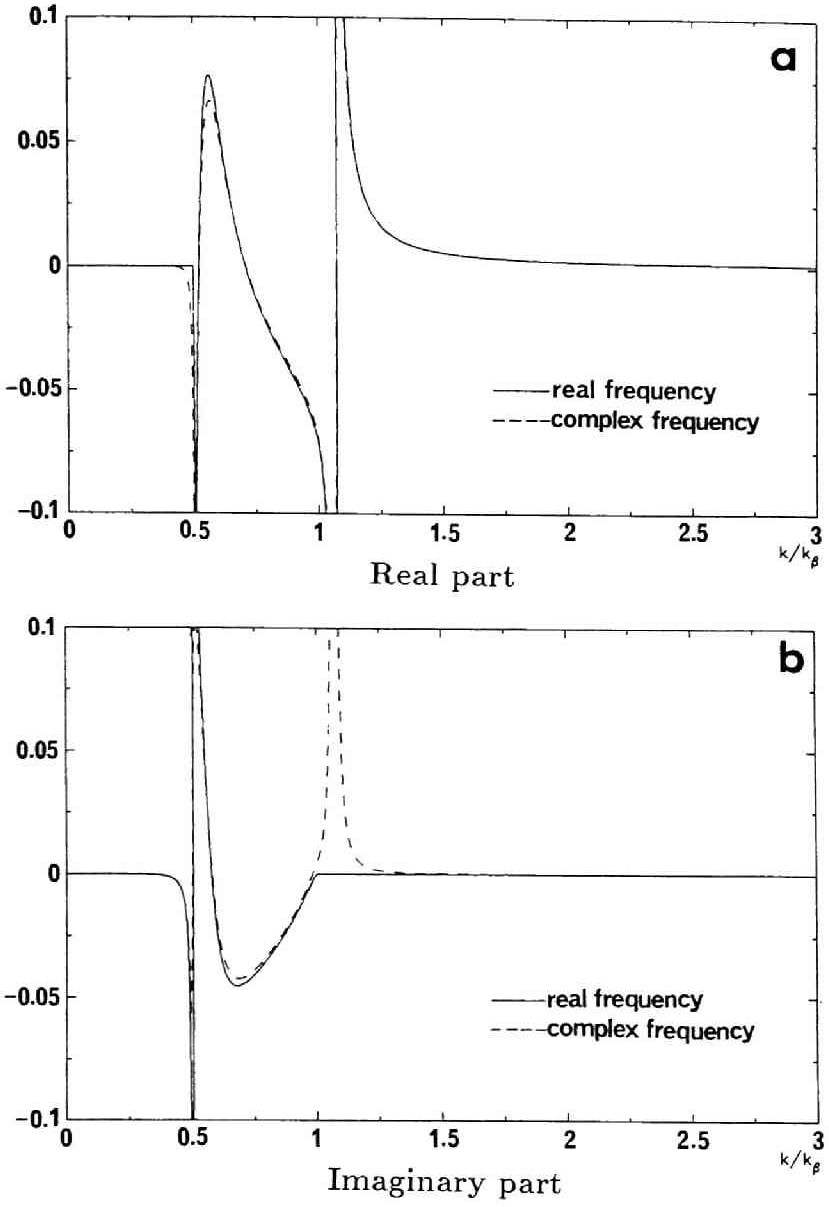

Figure 2.5: An example of a surface term of the Green function for a two-dimensional homogeneous half-space. S and P wave velocities of 1.0/sec and 2.0/sec are assumed. Frequency is set to be 5 Hz. **a** shows the real part and **b** shows the imaginary part of the integrand without e^{ikx} term. The abscissa is the normalized wavenumber. Solid lines represent functions without the imaginary part in frequency, whereas broken lines represent those with the imaginary part of 1% in frequency.

Considering the FFT version of equation (2.66) and equation (2.67), we realize that synthetic seismograms can be obtained from either the real part or the imaginary part for only the first half of the total duration ($0 \leq t < T/2$). The later halves of the real and imaginary part synthetics ($T/2 \leq t < T$) are just the mirror image of the first half and that with the opposite sign, respectively. Mathematically the response in the later half corresponds to the that for $-T/2 \leq t < 0$ but appears there because of the periodicity of FFT synthetics. If we have arrivals that appear in the later half, they will also appear in the first half of the real or imaginary part synthetics as contaminations because of this symmetricity. Therefore, $T/2$ should be long enough to include all the major arrivals.

If one needs the real part when he calculates only the imaginary part, or vice versa, he can get the other by using inverse FFT-forward FFT procedure. First the real part synthetics is obtained by just changing the sign in the later half of the imaginary part synthetics calculated by the FFT from the imaginary part. Taking the FFT of this new real part synthetics, then, he can get the real part of the Green function. Through this procedure we are essentially taking the Hilbert transform by FFT.

If the calculation time of the real part is the same as that of the imaginary part, the above procedure is of no practical importance. However, in the discrete wavenumber method, the imaginary part is much easier to evaluate than the real part, thanks to the fundamental nature of the Green function. Figure 2.5 shows an example of the surface term of the two-dimensional half-space Green function (Kawase and Aki, 1989b). If no damping is assumed, the function becomes pure real after the horizontal wavenumber k becomes larger than k_β, as shown in Figure 2.5. This means that the imaginary part can be evaluated as the principal value up to k_β plus the contribution from a Rayleigh pole, and therefore the wavenumber integration becomes finite. If damping is introduced or complex frequency is used, the function will not be pure real even for $k > k_\beta$ and sharp peaks appear because of a Rayleigh pole that reside just off the real k axis. However, the imaginary part converges much faster than the real part, as can be seen in Figure 2.5.

In general the wavenumber at which the real or imaginary parts would converge is a function of frequency, material constants, the source-receiver location, and

the desired accuracy. Table 2.1 shows an example of the maximum wavenumbers (normalized by k_β) to get the same relative error of 1.0×10^{-4} for the real and imaginary parts as a function of the receiver depth. The difference of convergence speed between the real and imaginary parts is significant as long as the receiver depth is small. From the parametric study it is found that it is enough to integrate up to twice of k_β to get convergence in the imaginary part. Of source, more sophisticated methods such as asymptotic expansion, polynomial extrapolation, or generalized Filon's method (e.g., Apsel and Luco, 1983; Frazer and Gettrust, 1984; Chapman and Orcutt, 1985) can be combined to further accelerate the convergence.

2.7 Summary of the proposed method

In this chapter the author presents the fundamental formulation of the proposed discrete wavenumber boundary element method. In essence the DWBEM is the combination of the direct BEM and the discrete wavenumber Green function. The author first shows the basic equations of the direct BEM using the representation theorem. The equations for an incident-wave problem and for an plural-region problem are also shown. Then the author summarizes the Green functions for full- and half-spaces in two and three dimensional wave fields by the discrete wavenumber method. Although the principles to derive these Green functions can be found in the literature, their complete forms that are necessary for the DWBEM is unknown to the author. Next exact term-by-term evaluation is presented for the element integrations. It is one of the advantages of the DWBEM because this element integration eliminates difficulties associated with a singularity of the Green functions if a force is applied on the element. Besides this integration guarantees convergence with respect to the horizontal wavenumber due to the additional term of order k_n^{-1}. Finally the author briefly describes a technique to evaluate the Green function more economically. By taking the imaginary part and reproducing the real part using the causality condition with FFT, the Green function can be calculated faster because the convergence of the imaginary part is faster than that of the real part.

The advantage of the DWBEM is its efficiency in computation and flexibility for boundary configurations, thanks to the fundamental nature of the discrete wave-

number Green functions and the direct BEM. Thus the DWBEM can model complex inhomogeneities of arbitrary numbers of regions by discretizing their boundaries of arbitrary shapes with variable-sized elements as far as our computer resource permits. At the same time, the accuracy and the stability of the solution, especially in high frequency range, are achieved without much precautions, thanks to the exact element integration and direct constraint for boundary conditions. The applications that prove these advantages of the DWBEM will follow.

As a final note, the advantage of periodic nature of the DWBEM should be mentioned. Problems of simple irregularities or inhomogeneities such as a cylindrical canyon in a half-space need to eliminate the effect of the adjacent fictitious structures by using the large periodicity length L and the complex frequency. However, the problems of periodic irregularities or inhomogeneities such as a mountain range or randomly distributed inclusions and cracks require the periodicity of structures so that the DWBEM is more suitable than the normal BEM or FEM solutions in which only finite part of such structures can be modeled.

Chapter 3

Theoretical Responses of 2D Irregularities

3.1 Description of the problem

Consider a two-dimensional homogeneous isotropic elastic medium subject to a harmonic excitation of an incident wave. Figure 3.1 shows the problem configuration and the incident waves considered here. In two-dimensional wave field in-plane motions u_1 and u_3 are decoupled with an anti-plane motion u_2.

There are two kinds of topographic irregularities considered here: a canyon and a ridge. Another topographic irregularity that often appears in the literature is a cliff. Since canyons and ridges are considered as two combined cliffs, it may be sufficient to study these two shapes in order to grasp the fundamental characteristics of wave scattering phenomena taking place around the surface irregularities.

As mentioned in the Chapter 1, the effects of topography and subsurface irregularities on the seismic response have been recognized widely as an important factor since Aki and Larner (1970) and Trifunac (1971) studied the effect of subsurface irregularities as a pioneering work. Since then extensive theoretical and experimental works have been carried out on the subject. However, wave scattering phenomena taking place around topographic irregularities due to various types of incident waves are still not well understood.

3.2 Validation

The frequency responses of a two-dimensional semicircular canyon are shown for comparison between the present results and published ones. Following Bouchon and Aki (1977), we introduce the imaginary part of the frequency that sufficiently suppresses the early arrivals of the waves generated by fictitious structures. Since this artificial damping affects the frequency response considerably, the effect should

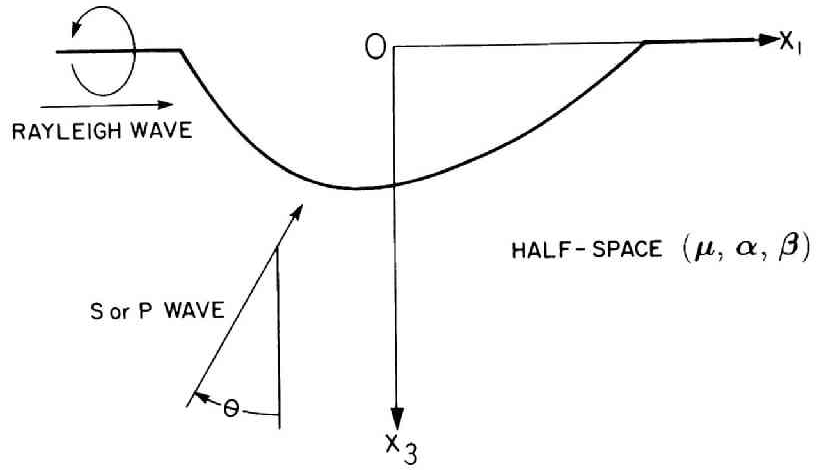

Figure 3.1: The conceptual model of a 2D irregularity. Both plane body-wave incidence and Rayleigh wave incidence are considered.

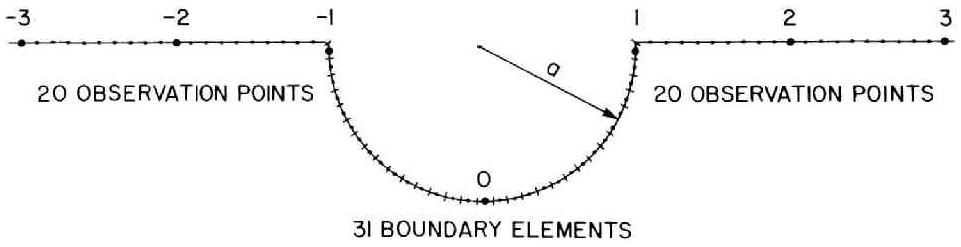

Figure 3.2: The model configuration and the element distribution of a semicircular canyon. Observation points on the horizontal surface are also shown. Totally 31 elements are used for calculation.

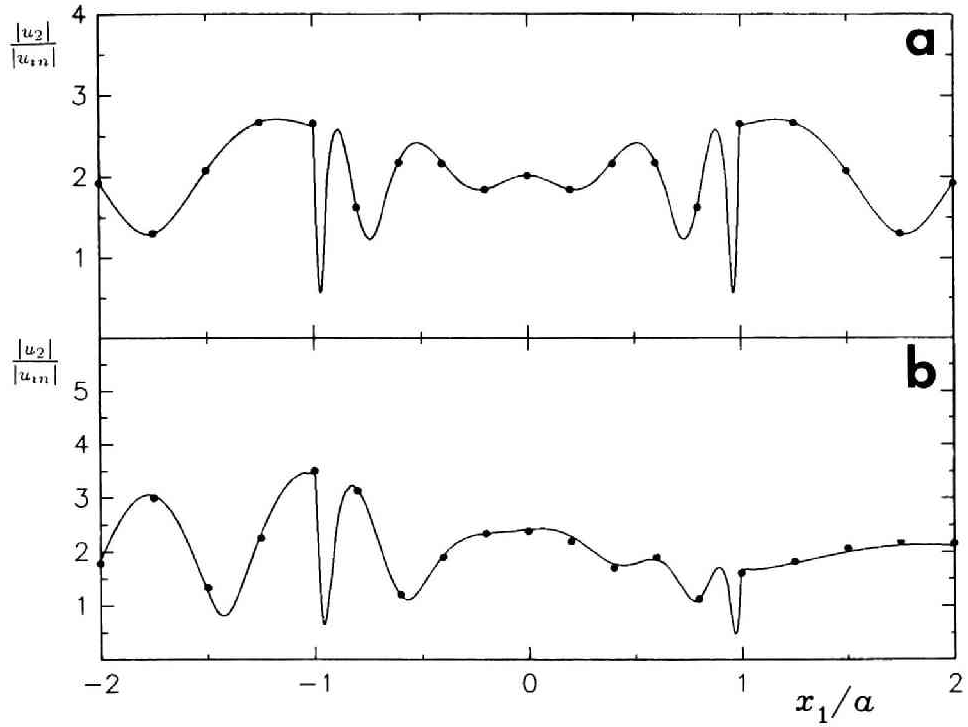

Figure 3.3: Frequency responses due to SH waves with the incidence angles of 0° (a) and 30° (b). The solid lines represent the results obtained by the conventional BEM, while solid circles represent the exact solution (Trifunac 1973). The nondimensional frequency $f_0\,(=\omega a/2\pi\beta)$ is set to 1.0.

be eliminated in the end using the following procedure. First we calculate the frequency response by using the complex frequency. Then the time-histories at observation points due to a proper input waveform are obtained by the inverse Fourier transform of the frequency responses followed by the exponentially increasing time window, which compensates the effect of the imaginary part. Finally, frequency transfer functions can be evaluated through the Fourier transform of these corrected time-histories and the input waveform.

To show the validity of the above procedure and to confirm the accuracy of the direct BEM itself, the responses due to incident SH waves calculated by the con-

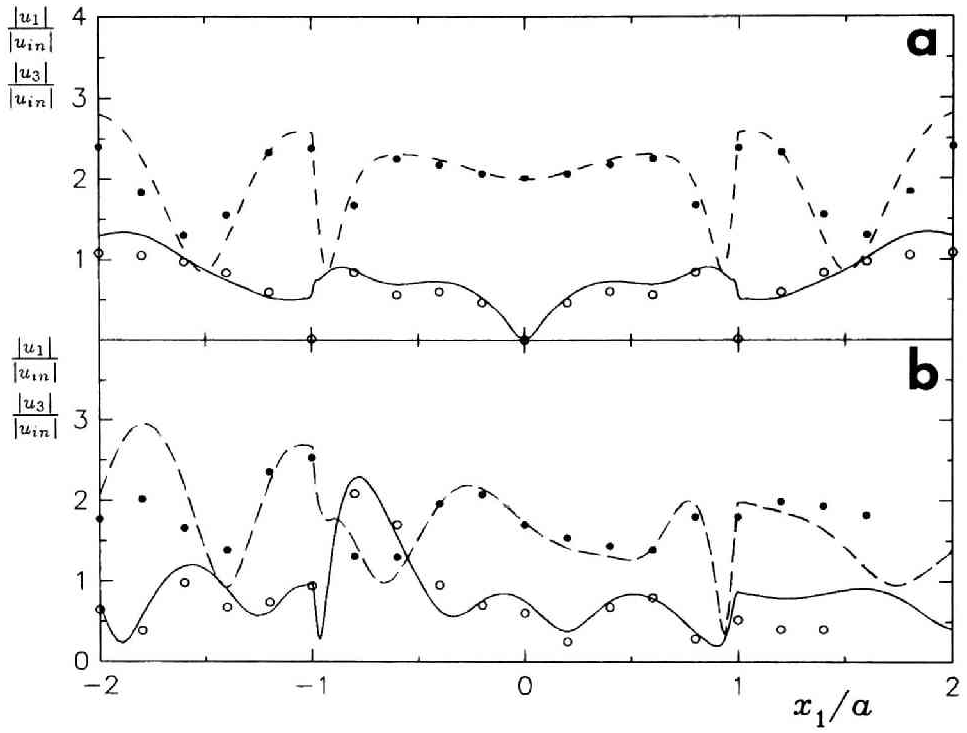

Figure 3.4: Frequency responses due to SV waves with the incidence angles of 0° (**a**) and 30° (**b**). The solid and broken lines are the amplitude for the horizontal and vertical components obtained by the DWBEM, while solid and open circles are the results by Wong (1982). Poisson's ratio is 1/3 and $f_0 = 1.0$.

ventional BEM (Kawase *et al.*, 1982; Kawase *et al.*, 1985) are compared with those obtained by the eigenfunction expansion method (Trifunac 1973). The same amount of imaginary part of the frequency is used as in the DWBEM. The distribution of the boundary elements along the canyon surface are shown in Figure 3.2

Figure 3.3 shows our results on the amplitude response distribution along the surface in and around the canyon by the solid line together with the results by Trifunac (1973) using solid circles. Only the cases for the nondimensional frequency $f_0 = \omega a/2\pi\beta = 1.0$ are shown hereafter, in which the S-wavelength is equal to the radius of the canyon a. This frequency corresponds to the characteristic frequency

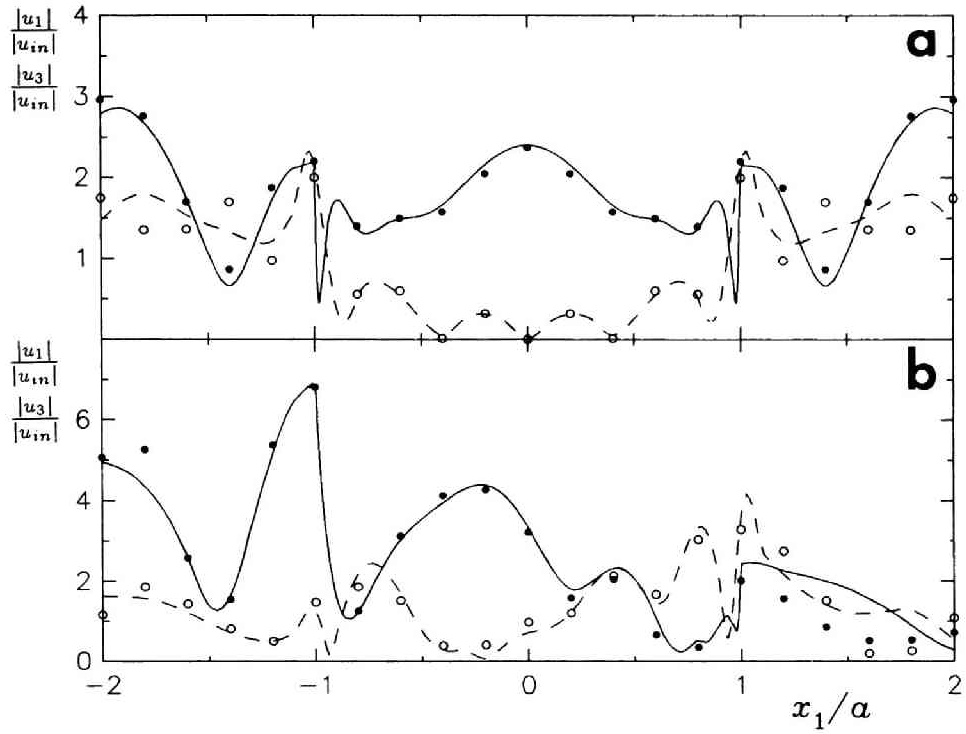

Figure 3.5: Frequency responses due to P waves with the incidence angles of 0° (**a**) and 30° (**b**). The meaning of the figure and parameters used are the same as in Figure 3.4.

of an incident wavelet used in the time-domain calculation. Note that f_0 is one half of the nondimensional frequency η in Trifunac's paper. The horizontal axis represents the nondimensional coordinate x_1/a along the x_1-axis. Vertical axis means the amplitude of the frequency response relative to the incident wave amplitude. Figures 3.3**a** and 3.3**b** correspond to the cases for incidence angles of 0° and 30°, measured clockwise from the vertical line as shown in Figure 3.1. The agreement of the results obtained by the conventional BEM and the procedure described above with the exact solutions is excellent in both incidence angles.

Next the validity of the DWBEM is shown by comparing the results with those by Wong (1979, 1982). In low frequency range, Wong's results have been verified by Sánchez-Sesma *et al.* (1985) and Dravinski and Mossessian (1987). No analytical

solution is available for a canyon in in-plane wave field. Poisson's ratio is assumed to be 1/3 and periodicity length L to be $20a$ which is large enough to prevent contaminations from adjacent fictitious canyons. Figure 3.4 shows the results for SV wave incidence with two different angles 0° and 30°. Both horizontal and vertical amplitudes are shown by solid and broken lines together with the Wong's results by symbols. The agreement of the results obtained by the DWBEM with Wong's is excellent in both horizontal and vertical components inside the canyon.

However, small discrepancies are observed along the surface outside the canyon. This seems to indicate the difficulty of the indirect BIEM to express the wave field outside the canyon correctly in higher frequency range as shown by Wong (1979) for SH wave incidence. Since the sources are located away from the canyon surface (i.e., near the center), the unknown source strength is less constrained by the boundary condition and thus the wave field expressed by these sources will become unreliable as the observation point goes away from the canyon. Increasing the numbers of sources will not improve the accuracy but will make the system equation unstable. On the other hand, in the DWBEM the boundary condition is imposed directly on the canyon surface where sources are located so that the solution is well constrained. Also the exact evaluation of the element integration for both displacements and tractions helps to give the stability of the solution. Thus we can get the causal and physically explainable time-histories as shown in the following sections by calculating the responses for nondimensional frequencies as high as 4.0.

Figure 3.5 shows the comparison for P wave incidence with the same angles of incidence. Also the case of a Rayleigh wave incidence is shown in Figure 3.6. Again the agreement is excellent in most cases. The results for lower frequencies, which are omitted here, are in excellent agreement both inside and outside the canyon.

3.3 Response of canyons

The evaluation of the frequency response by using the conventional BIEM or BEM requires considerable computational effort in case of in-plane wave field. This might be the reason why one can hardly find studies on the time response of a semicircular canyon due to incident P, SV or Rayleigh waves. Even for a SH

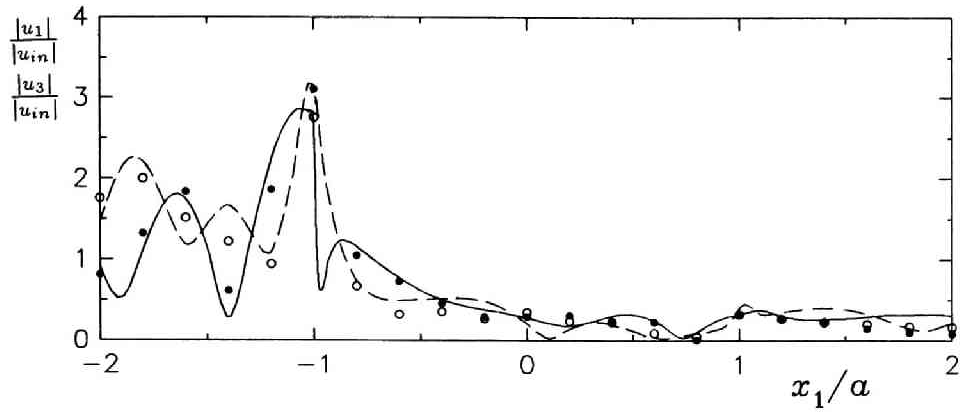

Figure 3.6: Frequency responses due to a Rayleigh wave. The meaning of the figure and parameters used are the same as in Figure 3.4.

wave incidence such a study is rare so far. Although the shape is too simple for a realistic canyon, it is worth to study the nature of the reflected and diffracted waves due to the topographical irregularities in time domain as well as in frequency domain. Here the author investigates the time-domain responses of the surface along a semicircular canyon subject to incident SH, SV, and P waves with two different angles of incidence and a Rayleigh wave.

In all the cases shown hereafter the shape of an incident wave is a Ricker wavelet defined as (Ricker, 1977)

$$u(\tau) = (2\pi^2 {f_c}^2 \tau^2 - 1)\exp(-\pi^2 {f_c}^2 \tau^2)\,, \tag{3.1}$$

where f_c is the characteristic frequency of a wavelet and τ is the nondimensional time $t\beta/a$ (t : real time). f_c is set to 1.0, the frequency used in Figures 3.3 through 3.6. Its shape and frequency spectrum are shown in Figure 3.7. The above expression of a Ricker wavelet, which is symmetric with respect to $\tau = 0$, will be modified to have appropriate amount of time shift. Calculated frequencies are 65 in total ranging from 0.0 to 4.0. Observation points are distributed at nearly equal interval measured along the surface both inside and outside the canyon, as shown in Figure 3.2.

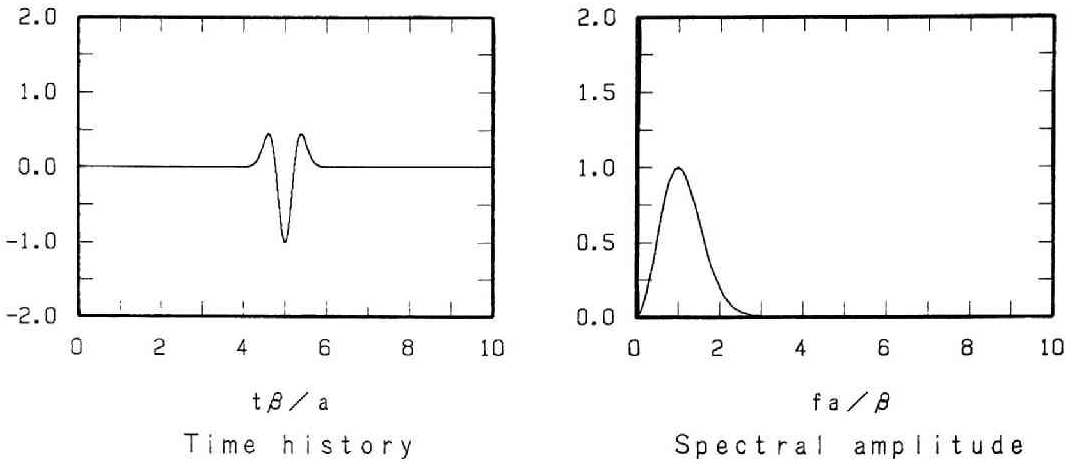

Figure 3.7: The shape and spectrum of a Ricker wavelet with the characteristic frequency f_c of 1.0. The nondimensional time axis is shifted by 5.0. The amplitude is normalized to 1 in both figures.

3.3.1 SH wave incidence

Figures 3.8 and 3.9 show the horizontal (anti-plane) responses of a canyon calculated by the conventional BEM due to incident SH waves with the angle of 0° and 30°, respectively.

In the case of a vertical incidence the direct waves keep the same amplitude along the surface of the canyon except near the edges, where the destructive interference occurs. In the case of an inclined incidence the amplitudes of the direct waves inside the canyon decrease toward the rear-side edge, which refers to the right edge in Figure 3.2. At the horizontal surface near the front-side edge, the left edge in Figure 3.2, the peak amplitude becomes larger due to the constructive interference between the direct wave and the wave reflected at the canyon. Those amplitude characteristics in time domain are, in general, consistent with the amplitude distribution in frequency domain.

On the other hand, the propagation of reflected and diffracted waves can be much more clearly seen in time domain than in frequency domain.

Outside the canyon later arrivals are mainly due to the wave reflection at the

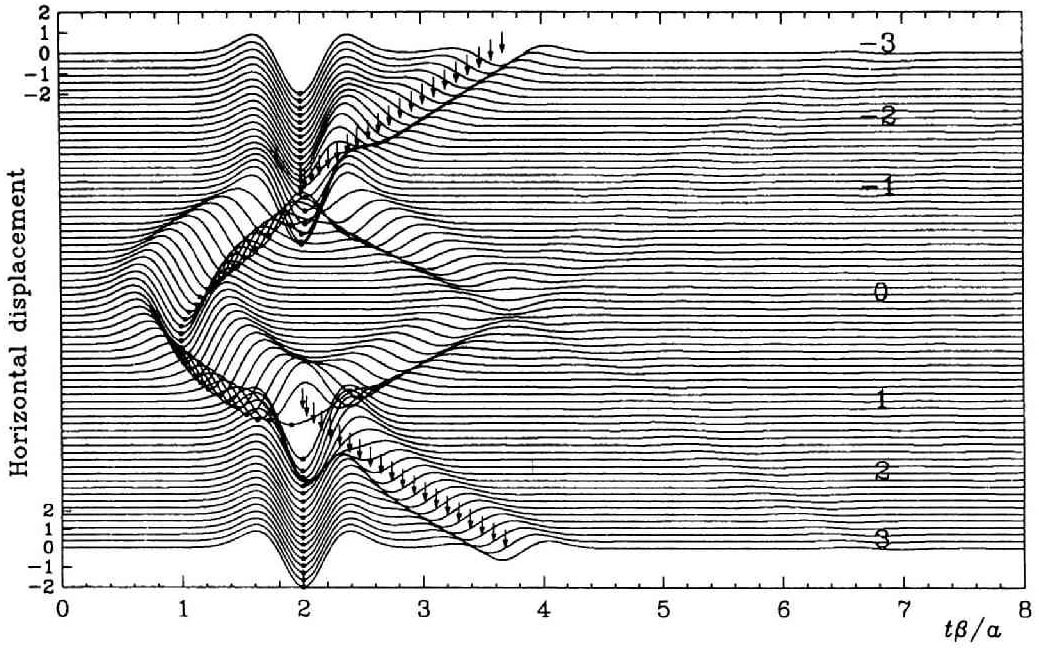

Figure 3.8: Time responses along the surface in and around a semicircular canyon due to a vertically incident SH wave. The characteristic frequency of a Ricker wavelet is 1.0. The horizontal axis is the nondimensional time $\tau = t\beta/a$ which is shifted properly. Numbers inside are the nondimensional positions x_1/a. Dots indicate the time of maximum for each time-history. Small arrows plotted outside the canyon indicate the arrival time of the peak calculated for the S waves reflected at the canyon surface.

upper part of the canyon surface. This can be confirmed by plotting the arrival time of the reflected waves in Figures 3.8 and 3.9 with small arrows. However, these later arrivals seem to contain some contribution of the diffracted waves since the amplitude changes very slowly. The amplitude of the reflected wave itself should decrease rapidly as the observation point goes away from the edges. In the case of an inclined incidence, these later arrivals can be clearly seen only in the front side. Again the arrival times of the reflected waves correspond very well to the peaks.

To further confirm the contribution of the reflected and diffracted waves, the responses of a trapezoidal canyon in Figure 3.10 are plotted in Figures 3.11 and 3.12. In this case the side slopes are flat so that the reflected waves only illuminate the

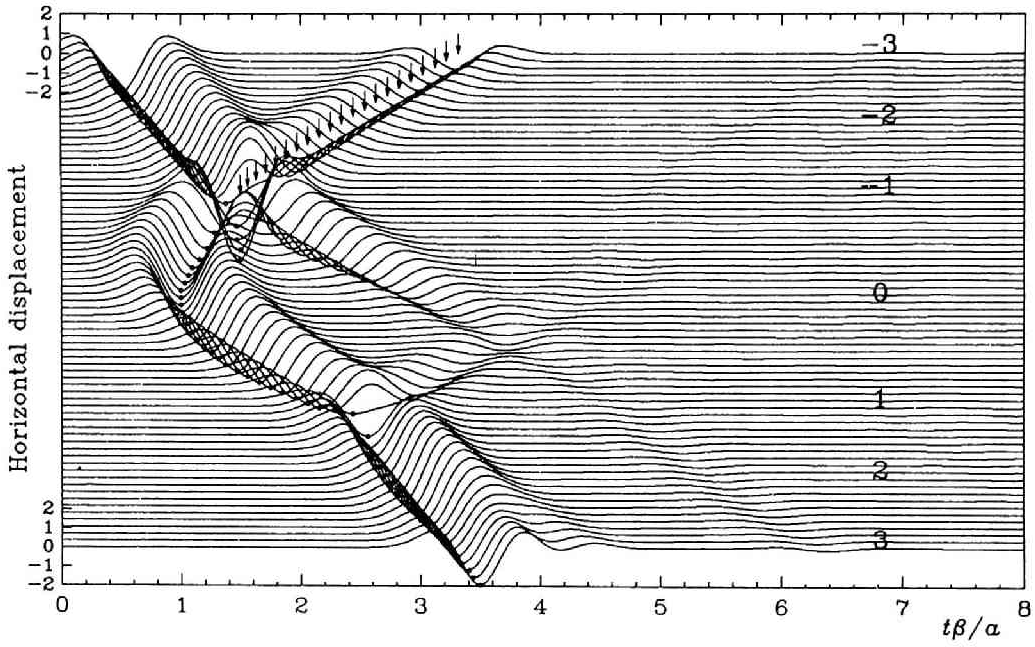

Figure 3.9: Time responses along the surface in and around a semicircular canyon due to an incident SH wave with the angle of 30°. The other conditions are the same as in Figure 3.8.

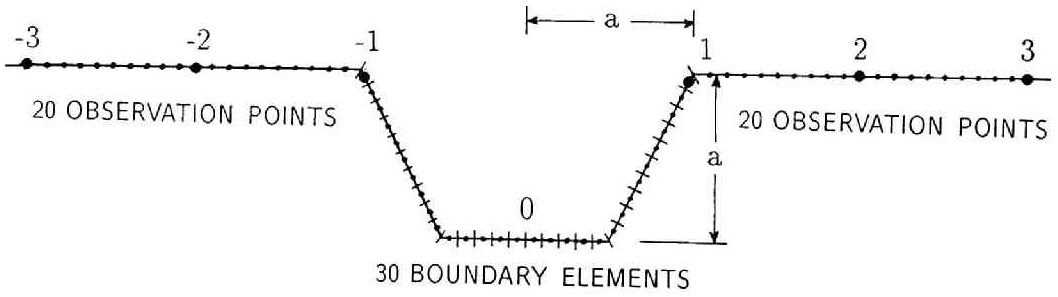

Figure 3.10: The model configuration of a trapezoidal canyon.

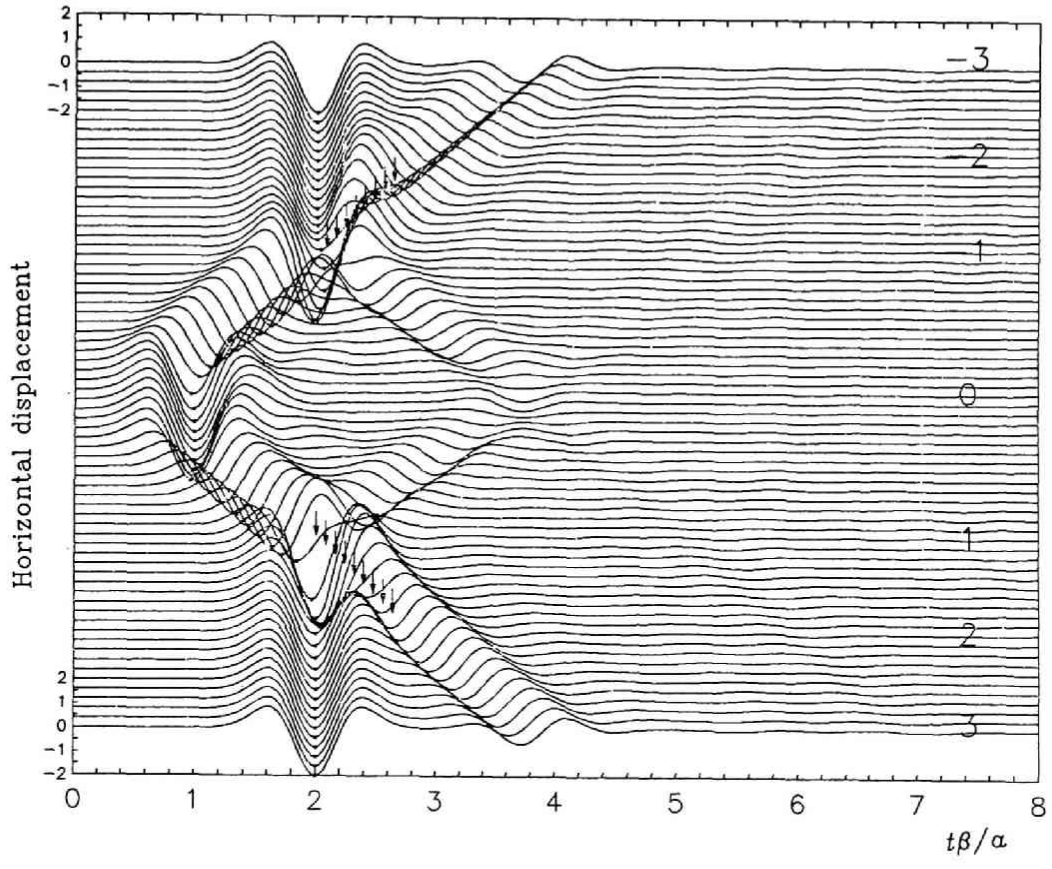

Figure 3.11: Time responses along the surface in and around a trapezoidal canyon due to a vertically incident SH wave. The other conditions are the same as in Figure 3.8.

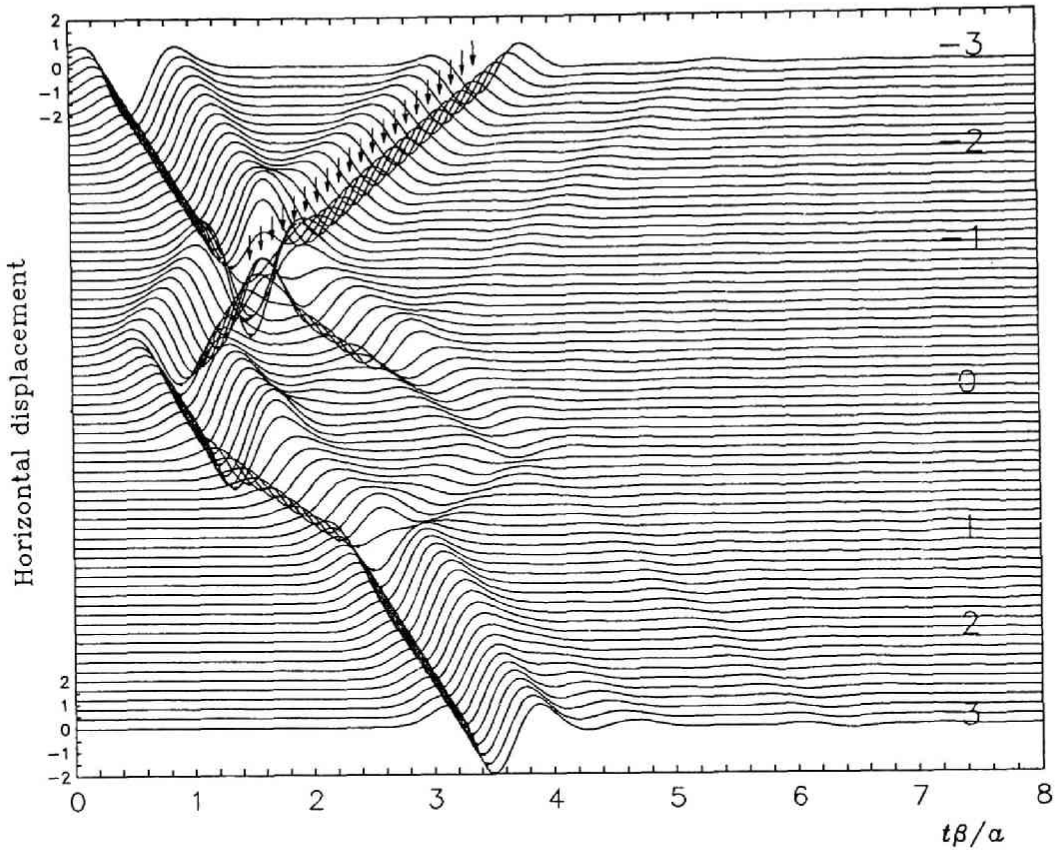

Figure 3.12: Time responses along the surface in and around a trapezoidal canyon due to an incident SH wave with the angle of 30°. The other conditions are the same as in Figure 3.8.

limited zone of the horizontal surface. Arrows in Figure 3.11 are placed only on the time-histories where the reflected waves will appear. The points without an arrow have only the diffracted wave contribution. It is found that the amplitude outside the canyon is decreasing slowly and that no noticeable difference between zones illuminated and not illuminated by the reflected waves. This clearly illustrates the important role of the diffracted wave to fill the gap, i.e., the displacement discontinuity, in the wave field.

Inside the semicircular canyon the diffracted waves, which seem to originate at the edges of the canyon, clearly propagate along the canyon surface with the apparent S wave velocity. These diffracted waves propagating along the smooth curvature may be called the *creeping* waves in elastodynamics, the term used for the first time by Franz (1954) in electromagnetism. It is difficult to predict the existence of this type of wave from the amplitude distribution in Figure 3.3 alone. The similar diffracted waves can be seen on the surface of the trapezoidal canyon.

3.3.2 SV wave incidence

Figures 3.13**a** and 3.13**b** show time histories due to a vertically incident SV wave for the horizontal (in-plane) and the vertical motions, respectively. The calculation conditions are the same as in the SH wave case.

With respect to the direct wave appearing on the horizontal component, features similar to the SH wave case can be observed inside and outside the canyon except near the edges, where more complicated interference occurs. The vertical component generated by the impact and subsequent reflection of incident wave at the canyon surface grows as the wave propagates upward and reaches its maximum at the edges.

Inside the canyon the diffracted waves have more complicated features than those for the SH wave case, especially in the horizontal component. Although it is difficult to distinguish clearly, the earlier part of the diffracted waves seems to be the *creeping* P waves, while the later part seems to be the *creeping* SV waves from their apparent velocities.

Outside the canyon later arrivals can be observed similarly to those for a SH wave incidence. However, they appear to become Rayleigh waves soon after

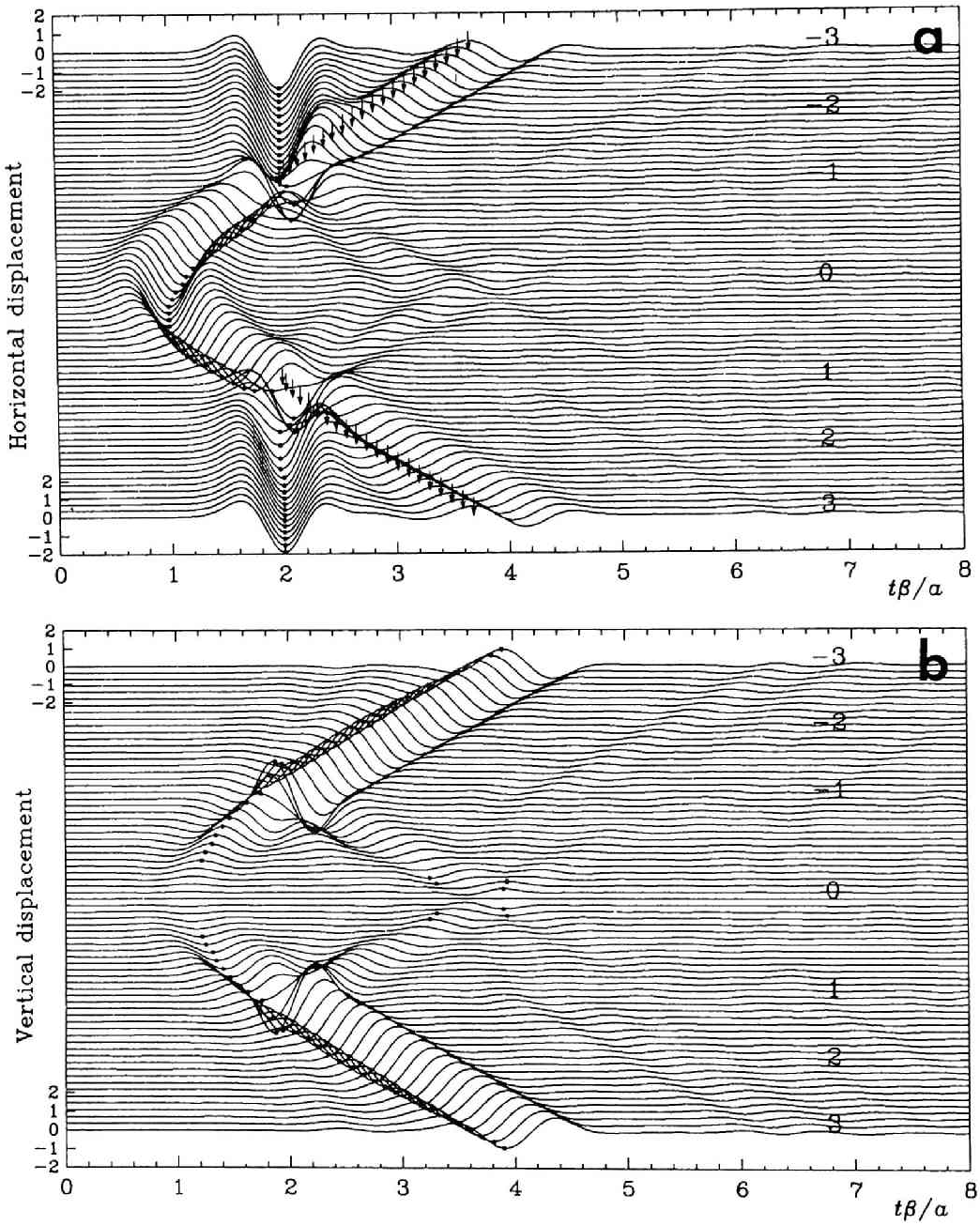

Figure 3.13: Time responses along the surface in and around a semicircular canyon due to a vertically incident SV wave. **a** and **b** correspond to the horizontal and vertical components. Poisson's ratio is 1/3. The other conditions are the same as in Figure 3.8.

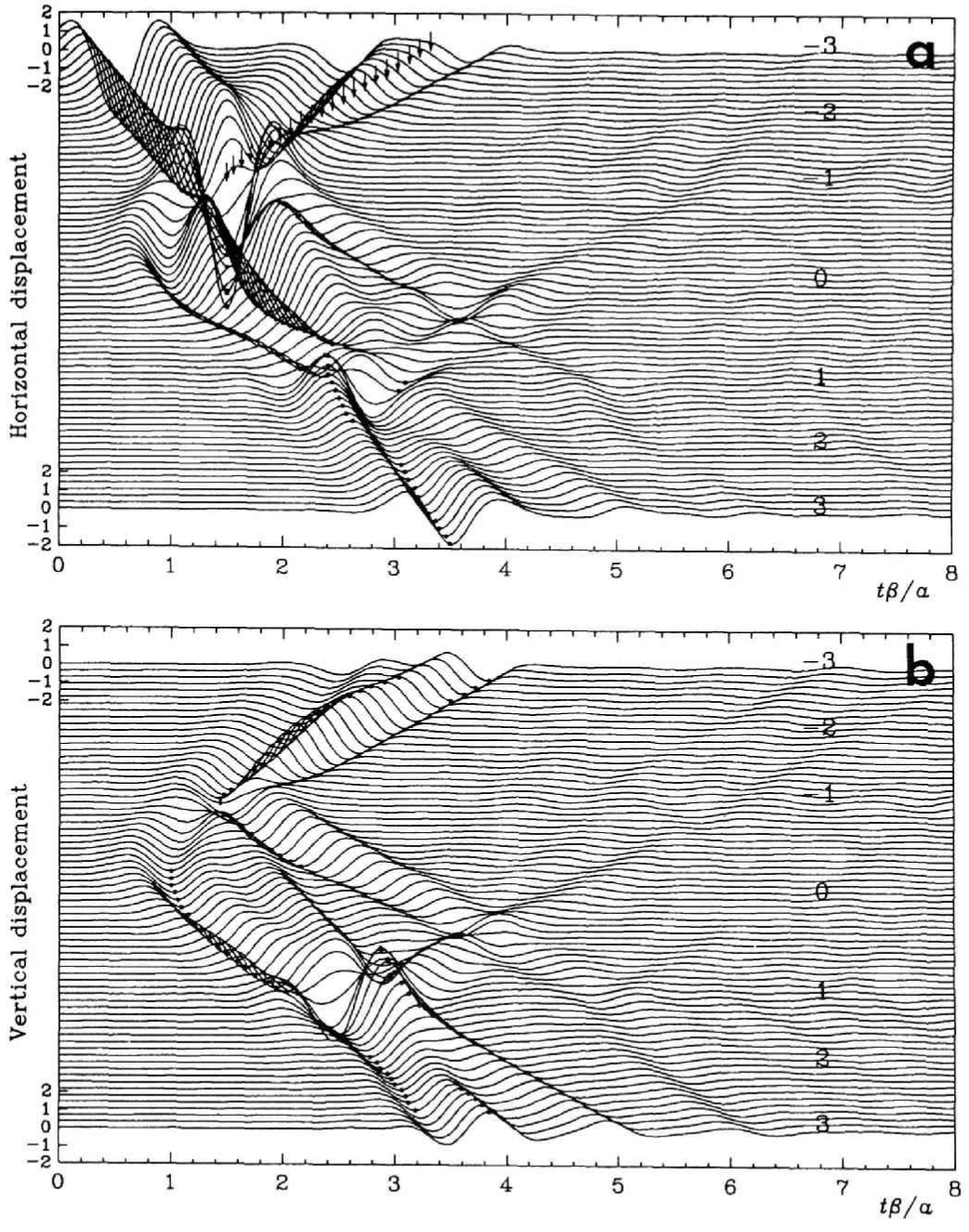

Figure 3.14: Time responses along the surface in and around a semicircular canyon due to an incident SV wave with the angle of 30°, which corresponds to the critical angle. The horizontal and vertical free-field amplitudes for a homogeneous half-space are 3.46 and 0.00, respectively. The other conditions are the same as in Figure 3.13.

the departure from the edges judging from their particle motions and apparent velocities. Neither the reflected P nor SV waves can be seen clearly. As is natural for Rayleigh waves in two-dimensional field without material damping, those waves keep the same shape and amplitude as they propagate.

The apparent fluctuation of the response amplitude for a particular frequency seen outside the canyon does not accurately express the real physical phenomena, because the phase information is disregarded. This clearly illustrates the importance of the time-domain solutions over the frequency-domain amplitude.

Next an obliquely incident SV wave is considered with the incident angle of 30°. The results are plotted in Figure 3.14. Many different features arise as compared with the SH wave case.

Even the amplitudes of the direct waves on the horizontal component, which should equal to 3.46 in case of a homogeneous half-space, change strongly along the surface. This is mainly due to the geometrical effect of incident and reflected SV waves. Another significant difference between SV and SH wave incidence is that the wave arrivals with very large amplitude appear inside the canyon soon after the direct waves. These may be due to the horizontally propagating (inhomogeneous) P wave created by the critical incidence. Also the *creeping* P and SV waves can clearly be seen inside the canyon.

Differently from the vertical incidence, the P waves reflected at the canyon surface can be observed in front of the canyon, and so the Rayleigh wave amplitude is relatively small. The reflected SV waves are still not clear.

3.3.3 P wave incidence

Comparing a P wave incidence with a SV wave incidence, everything becomes simpler. Figure 3.15 shows the responses due to a vertically incident P wave. The amplitudes of the direct waves on the vertical component are almost the same along the surface except near the edges, and the amplitudes of the diffracted waves inside the valley and the those of Rayleigh waves outside the valley are relatively small. These reflect the fact that the P-wavelength here is twice as large as the S-wavelength and so the interaction between the incident wave field and the surface irregularity becomes smaller. The reflected P waves can be observed outside the

canyon as pointed by arrival-time arrows.

Figure 3.16 shows the responses due to an obliquely incident P wave with the angle of 30°. The direct waves on the vertical component mostly keep the same amplitude except near the rear-side edge, which is in the shadow zone. The *creeping* P and SV waves generated at the front-side edge are clearly seen propagating toward the rear-side edge. Clear arrivals of the reflected P wave are again observed in front of the canyon.

3.3.4 Rayleigh wave incidence

Finally the case of a Rayleigh wave incidence is examined. Figure 3.17 shows the responses of a canyon subject to a Rayleigh wave. The amplitude of an incident Rayleigh wave is normalized by its horizontal component, which gives the vertical amplitude of 1.56 .

As was pointed out by Wong (1979, 1982) and shown in Figure 3.6, blocking effect of the canyon to the Rayleigh wave with relatively short wavelength is significant: less than 10% of incident wave amplitude can transmit through the canyon. Large amplification is observed just in front of the canyon due to the reflection of the incident Rayleigh wave, while the amplitude is reduced drastically as the wave propagates inside the canyon. It should be noted that the main part of the waves inside the canyon seems to be the diffracted waves similar to those for body wave incidence, rather than a horizontally propagating Rayleigh wave.

The amplitude in time domain is consistent with that in frequency domain in general, however, the horizontal surface in front of the canyon is an exception. The amplitude in frequency domain fluctuates strongly as can be seen in Figure 3.6, although the maximum amplitude in time domain does not change unless the point reaches close to the edge. This fluctuation in frequency domain is again due to the arrival-time difference between the direct and reflected waves.

3.4 Response of a ridge

As we have seen in the foregoing section even a simple semicircular canyon can exhibit very interesting scattering phenomena. In case of a ridge we see different

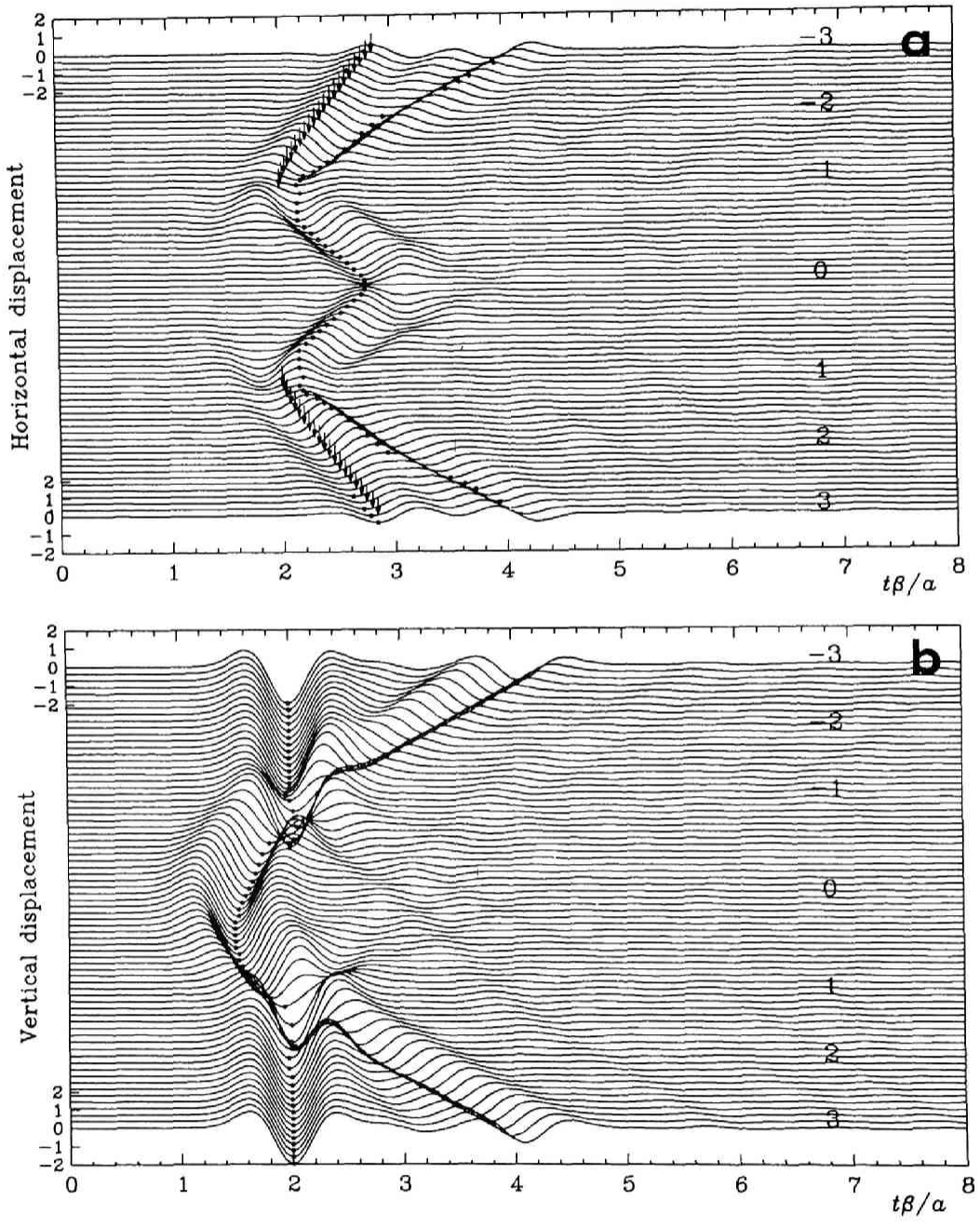

Figure 3.15: Time responses along the surface in and around a semicircular canyon due to a vertically incident P wave. Small arrows indicate the arrival time calculated for the P waves reflected at the canyon. The other conditions are the same as in Figure 3.13.

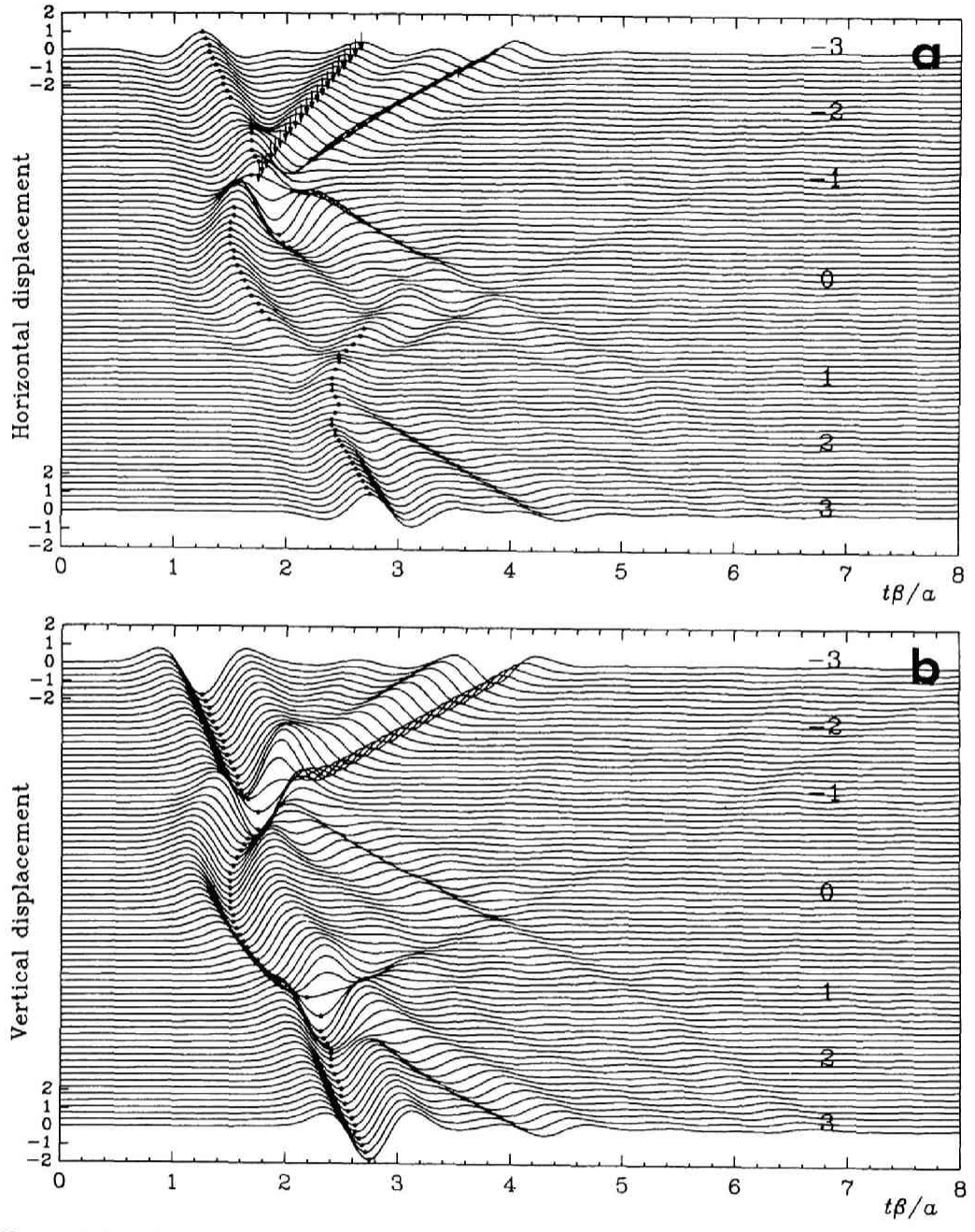

Figure 3.16: Time responses along the surface in and around a semicircular canyon due to an incident P wave with the angle of 30° The horizontal and vertical free-field amplitudes for a homogeneous half-space are 0.96 and 1.74, respectively. The other conditions are the same as in Figure 3.15.

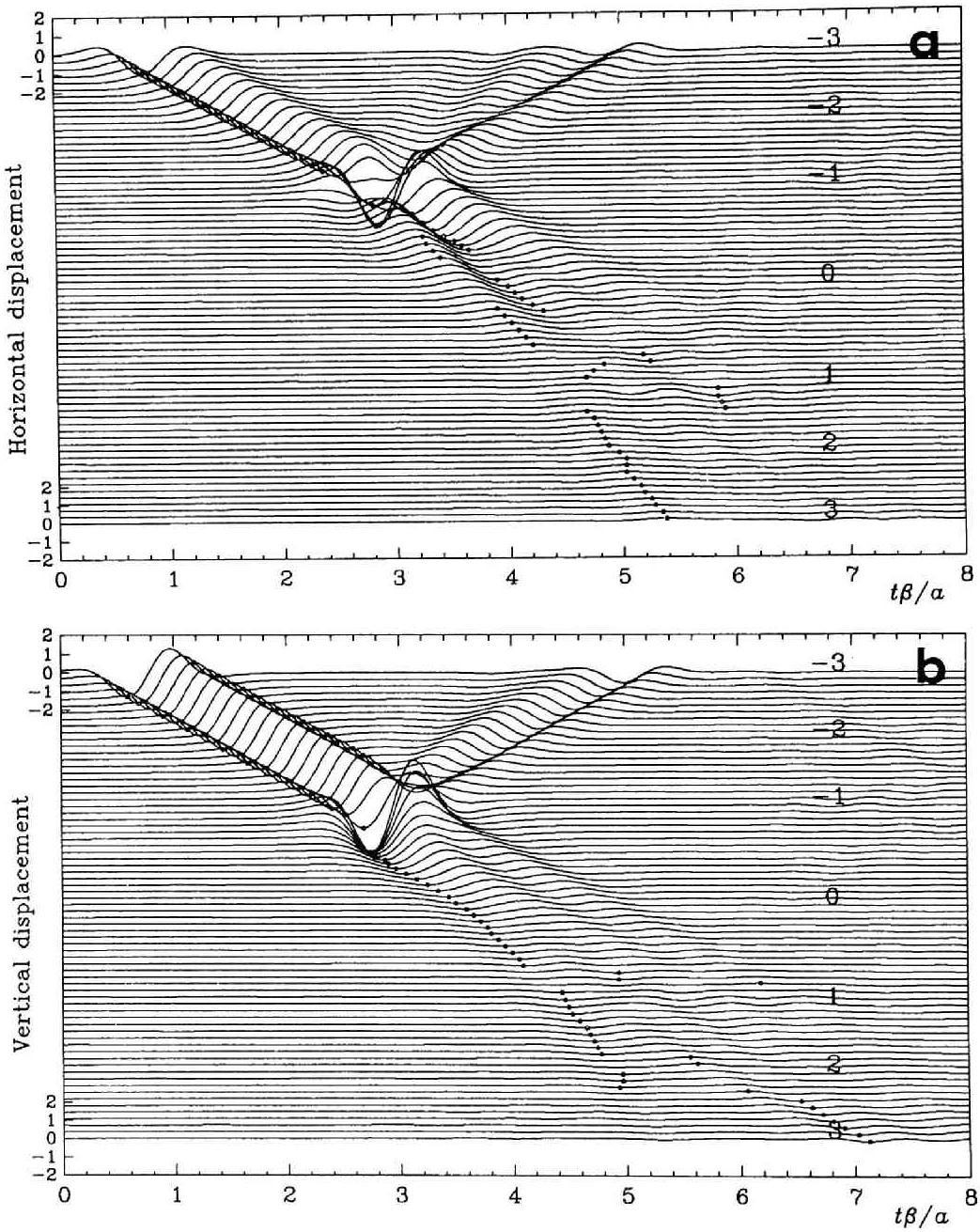

Figure 3.17: Time responses along the surface in and around a semicircular canyon due to a Rayleigh wave. The horizontal and vertical free-field amplitudes for a homogeneous half-space are 1.00 and 1.56, respectively. The other conditions are the same as in Figure 3.15.

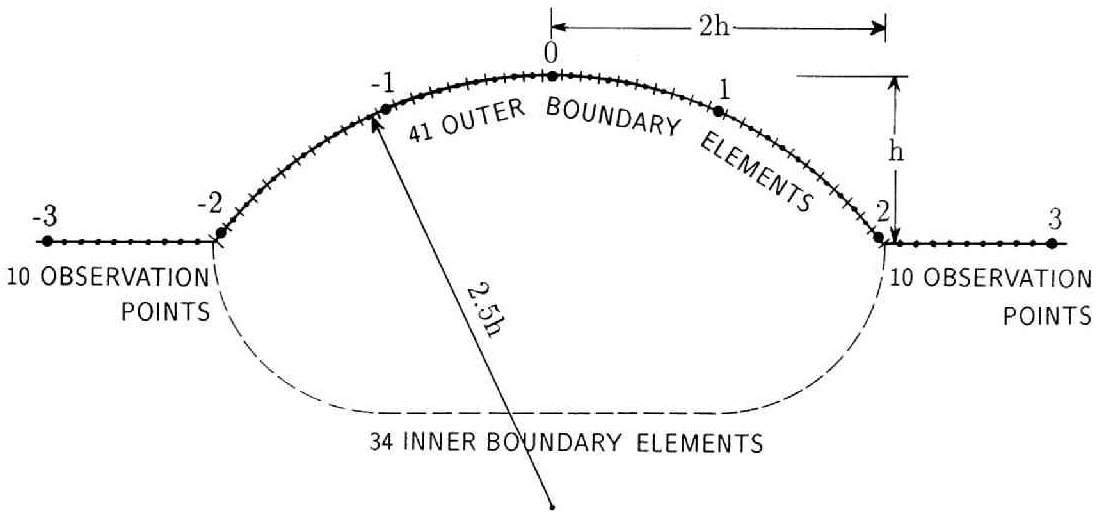

Figure 3.18: The model configuration and the element distribution of a ridge. Observation points on the horizontal surface are also shown. Totally 41 elements are placed along the surface of a ridge and 34 elements along the auxiliary boundary.

types of scattering phenomena that are also very interesting. The theoretical responses of ridges and mountains in a two-dimensional wave field have been studied by numerous authors (e.g., Boore, 1972; Bouchon, 1973; Smith, 1975; Sills, 1978; Bard, 1982; Geli, 1988), however, detailed investigation of reflected and diffracted waves created by a ridge in time-domain response have not been completed yet.

In this section a simple model of a ridge as shown in Figure 3.18 is analyzed for SH, SV, P, and Rayleigh wave incidence. Since the half-space Green function in equation (2.33) satisfies the stress free condition everywhere on the horizontal surface, we need to first excavate the half-space and then fill the cavity with soil whose surface is elevated. Thus we need to use equations (2.12) and (2.13) for the same material that connected with each other at the auxiliary boundary within a half-space. The broken line in Figure 3.18 represents this boundary. The shape of a ridge is assumed to be a circular arc of radius $2.5h$ where h is the height of a ridge. It gives the half-width of a ridge $2h$. Calculated frequencies are 41 in total ranging from 0.0 to 4.0. Totally 61 observation points are distributed at nearly equal interval

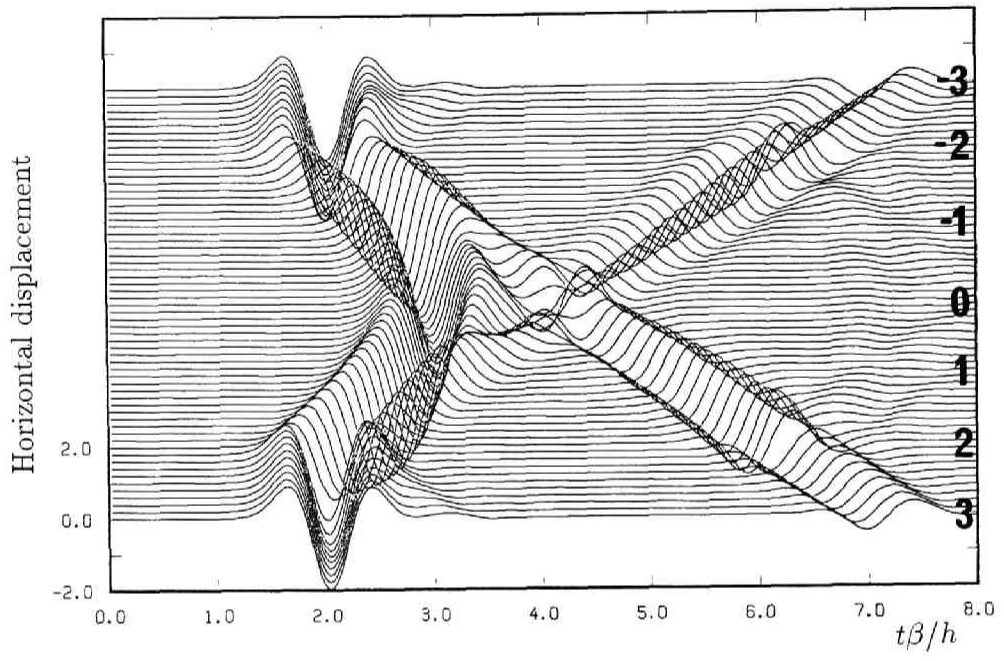

Figure 3.19: Time responses along the surface of a ridge due to a vertically incident SH wave. The characteristic frequency of a Ricker wavelet is 1.0. The horizontal axis is the nondimensional time $\tau = t\beta/h$ which is shifted properly. Numbers inside are the nondimensional positions x_1/h.

measured along the surface of the ridge and the surrounding half-space.

3.4.1 SH wave incidence

Figures 3.19 and 3.20 show the horizontal (anti-plane) responses of a ridge calculated by the DWBEM due to incident SH waves with the angle of 0° and 30°, respectively.

In the case of a vertical incidence the direct waves keep almost the same amplitude along the surface of the ridge. Very small amplification in the middle of the side slopes and very small deamplification near the edges are observed. The diffracted waves generated at the edges are propagating along the convex surface to the opposite side edges. It is very interesting that the amplitude of these diffracted waves are increasing as they propagate. This phenomenon is opposite to that ob-

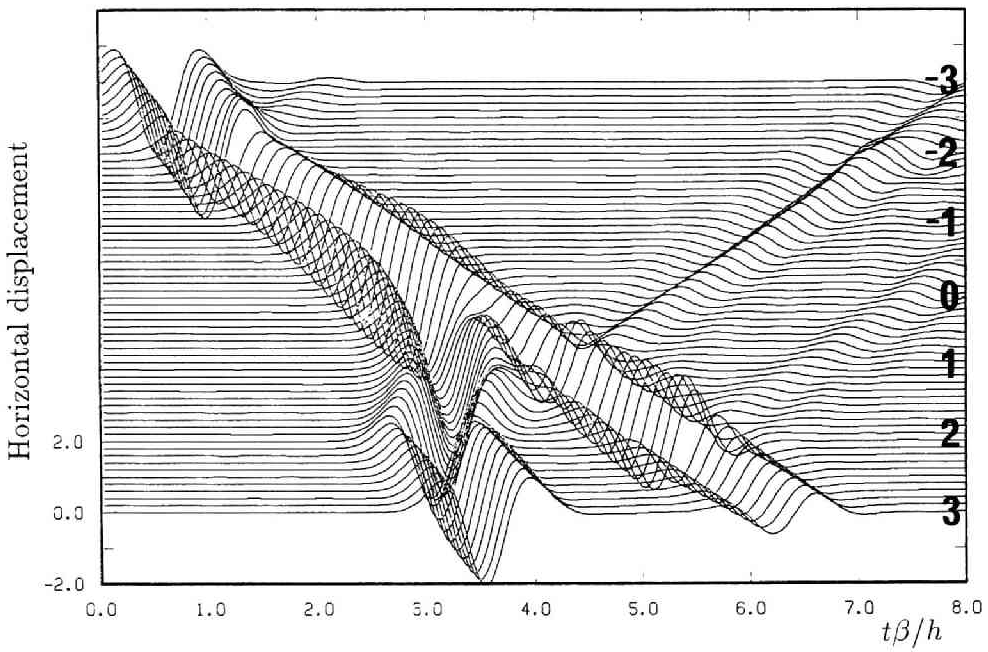

Figure 3.20: Time responses along the surface of a ridge due to an incident SH wave with the angle of 30°. The other conditions are the same as in Figure 3.19.

served for a canyon in which the *creeping* wave along the concave surface is losing its energy quickly (See Figure 3.8). We can interpret this as a result of energy concentration by successive multiple reflections along the convex curvature, a "whispering gallary"-like phenomenon. A careful observation reveals that the small amplification in the middle of the side slopes seems to be due to the diffracted waves.

In the case of an inclined incidence the direct wave amplitude are varying along the surface. Near the front-side edge only 65% of the half-space amplitude is observed, while near the hilltop about 120% amplification. The latter again may be due to the constructive interference of the direct wave with the diffracted wave propagating from the front-side edge to the rear-side edge. The diffracted wave propagating backward has rather small amplitude.

3.4.2 SV wave incidence

Figures 3.21**a** and 3.21**b** show time histories due to a vertically incident SV wave for the horizontal (in-plane) and the vertical motions, respectively. The calculation conditions are the same as in the SH wave case.

As for the direct wave appearing on the horizontal component, much larger amplification reaching 150% of an incident amplitude is observed at the hilltop. On the surface of the ridge diffracted waves have more complicated features than those for the SH wave case. The earlier part of diffracted waves seems to be the *creeping* P waves, while the later part seems to be the *creeping* Rayleigh waves from their apparent velocities and the amplitude ratios between horizontal and vertical components. A normal Rayleigh wave is associated with a flat surface; however, the latest but largest arrival of the diffracted wave seen in Figure 3.21 has doubtlessly slower propagation speed than the S wave velocity so that it is called here the *creeping* Rayleigh waves, meaning successive generation of Rayleigh waves along the curved surface. The *creeping* SV waves are barely observed in the vertical component just before the arrivals of the *creeping* Rayleigh waves.

Outside the ridge diffracted waves generated by the direct wave and the *creeping* P, SV, and Rayleigh waves are all observed. They appear to become Rayleigh waves soon after the departure from the edges as in the case of a canyon (Figure 3.13).

Next an obliquely incident SV wave is considered with the incident angle of 30°. The results are plotted in Figure 3.22. Many different features arise as compared with the SH wave case.

Even the amplitude of the earlier part on the horizontal component changes strongly along the surface. The amplitude, which starts from 3.46 on the horizontal surface, greatly decreases as the wavefront moves into the ridge and keeps almost 15% level of the half-space amplitude until it reaches at the rear-side edge where it recovers up to about 70% level. If we compare Figure 3.22 with Figure 3.20 for the SH wave incidence, we found that the earliest arrival at the ridge surface does not seem to be the direct SV wave, which should have a curved distribution of arrival time as in the SH case. Rather, it may be the inhomogeneous P wave, which should have vertical wavefront and therefore should have a constant apparent velocity even

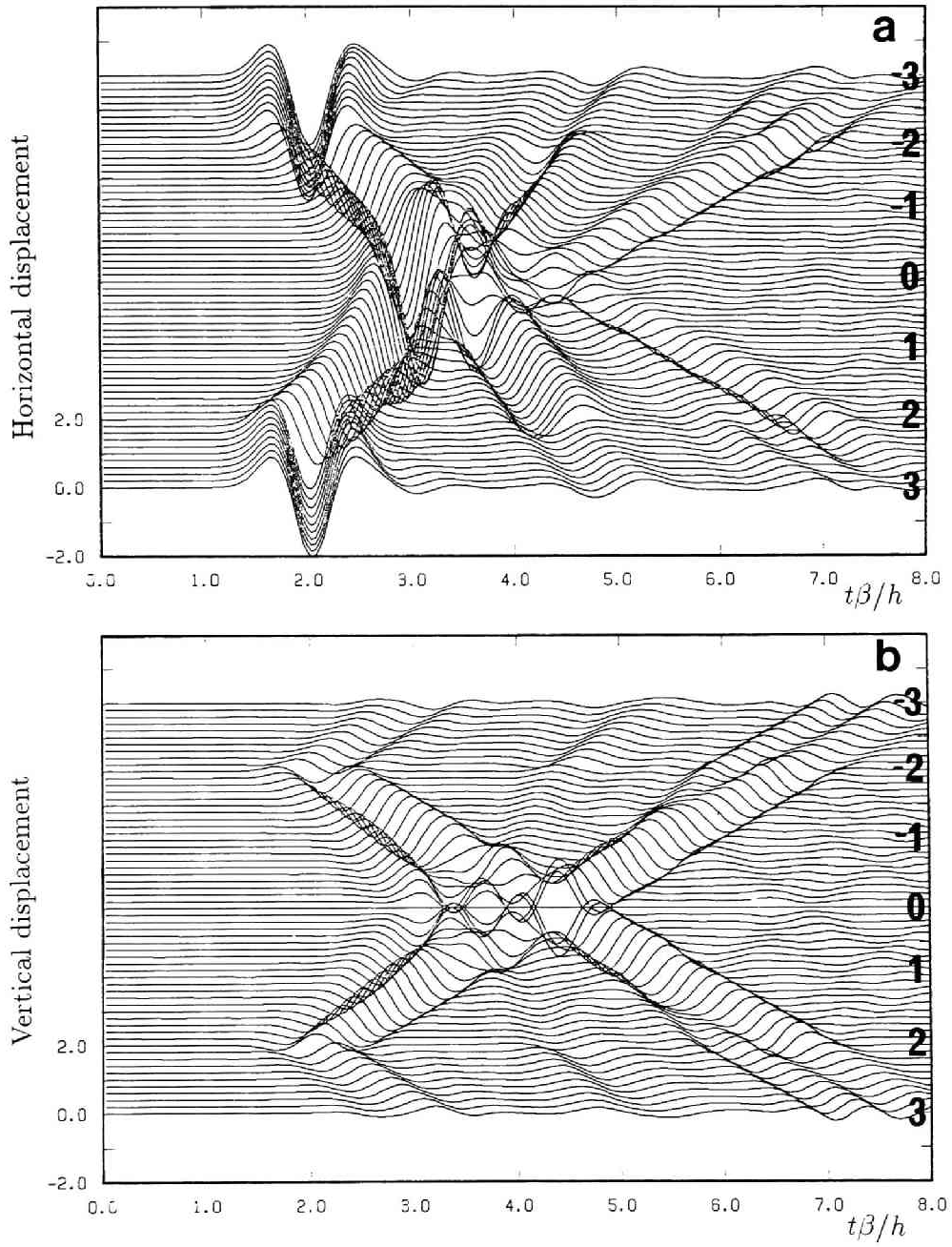

Figure 3.21: Time responses along the surface of a ridge due to a vertically incident SV wave. **a** and **b** correspond to the horizontal and vertical components. Poisson's ratio is 1/3. The other conditions are the same as in Figure 3.19.

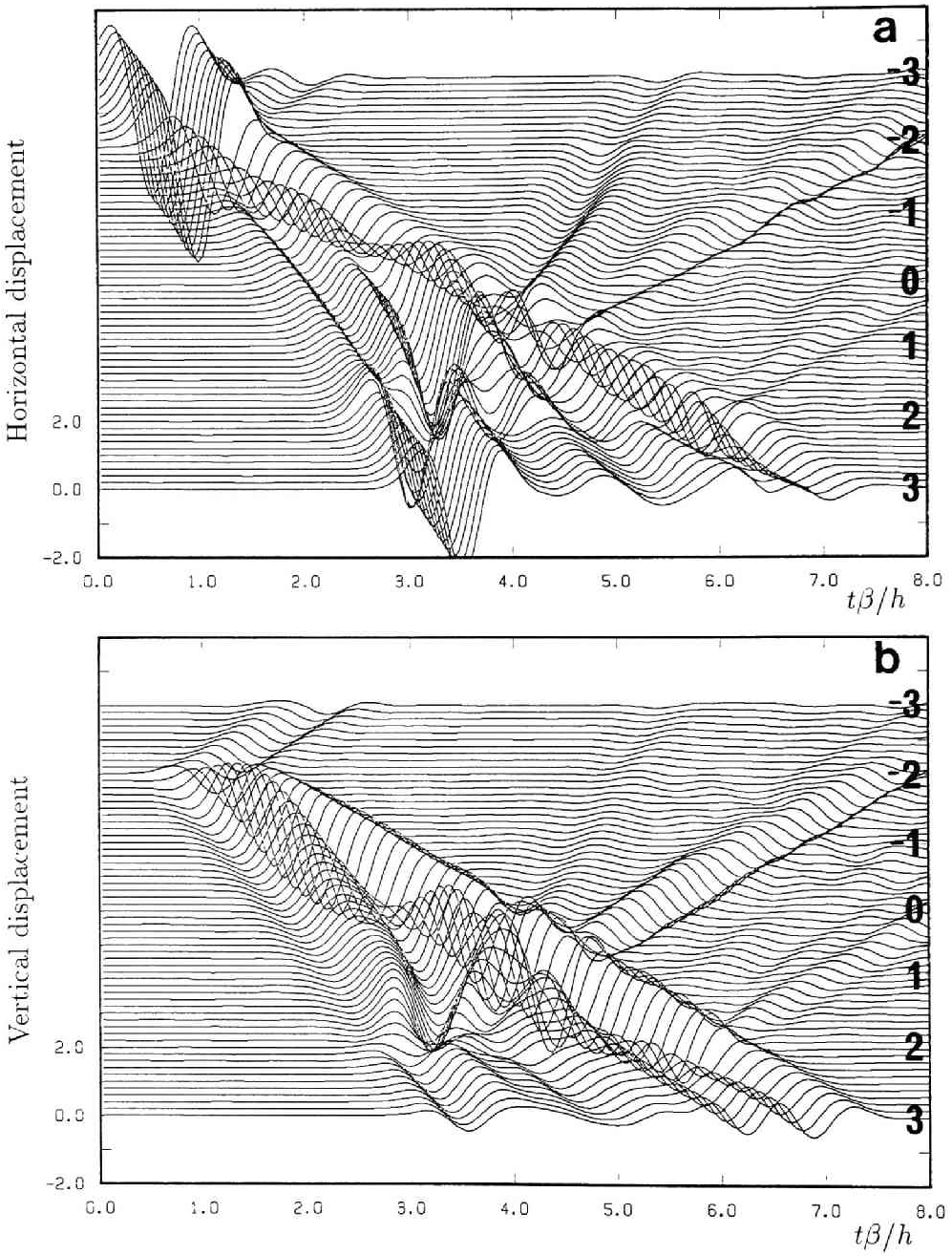

Figure 3.22: Time responses along the surface of a ridge due to an incident SV wave with the angle of 30°, which corresponds to the critical angle. The other conditions are the same as in Figure 3.21.

at the ridge surface.

The amplitude of the direct SV wave for the horizontal component increases toward the rear-side slope and reaches its maximum 2.4 at $x_1/h = 1.1$. The amplitude of the vertical component, which is zero at the horizontal surface, first increases till $x_1/h = -1.2$, then decreases near the hilltop, then again increases to reach 2.3 at $x_1/h = 1.0$. Large amplification in the front-side slope may be due to the diffracted waves. The later arrivals consist of the *creeping* P, SV, and Rayleigh waves as in the vertical incidence, although it is difficult to distinguish clearly. Thus the deamplification phenomenon first reported by Bard (1982) for a ridge with the critical incidence of SV wave is found to be caused by the energy splitting to different types of waves and components as described here. The *creeping* P and Rayleigh waves propagating backward can be seen on the ridge surface.

3.4.3 P wave incidence

In case of a P wave incidence everything becomes simpler as in the case of a canyon. Figure 3.23 shows the responses due to a vertically incident P wave. The amplitudes of the direct waves on the vertical component are almost the same along the surface, and the amplitudes of the diffracted waves on the ridge slope are relatively small. These reflect again the weak interaction between the incident P wave and the surface topography. The *creeping* P and Rayleigh waves can be observed clearly, while the *creeping* SV wave is barely observed as in the case of a SV wave incidence.

Figure 3.24 shows the responses due to an obliquely incident P wave with the angle of 30°. The direct waves on the vertical component mostly keep the same amplitude except near the edges. The *creeping* P and Rayleigh waves generated at the front-side edge are clearly seen propagating toward the rear-side edge. Back scattered P and Rayleigh waves are also observed.

3.4.4 Rayleigh wave incidence

Figure 3.25 shows the responses of a ridge subject to a Rayleigh wave. A very interesting phenomenon can be seen in the figure.

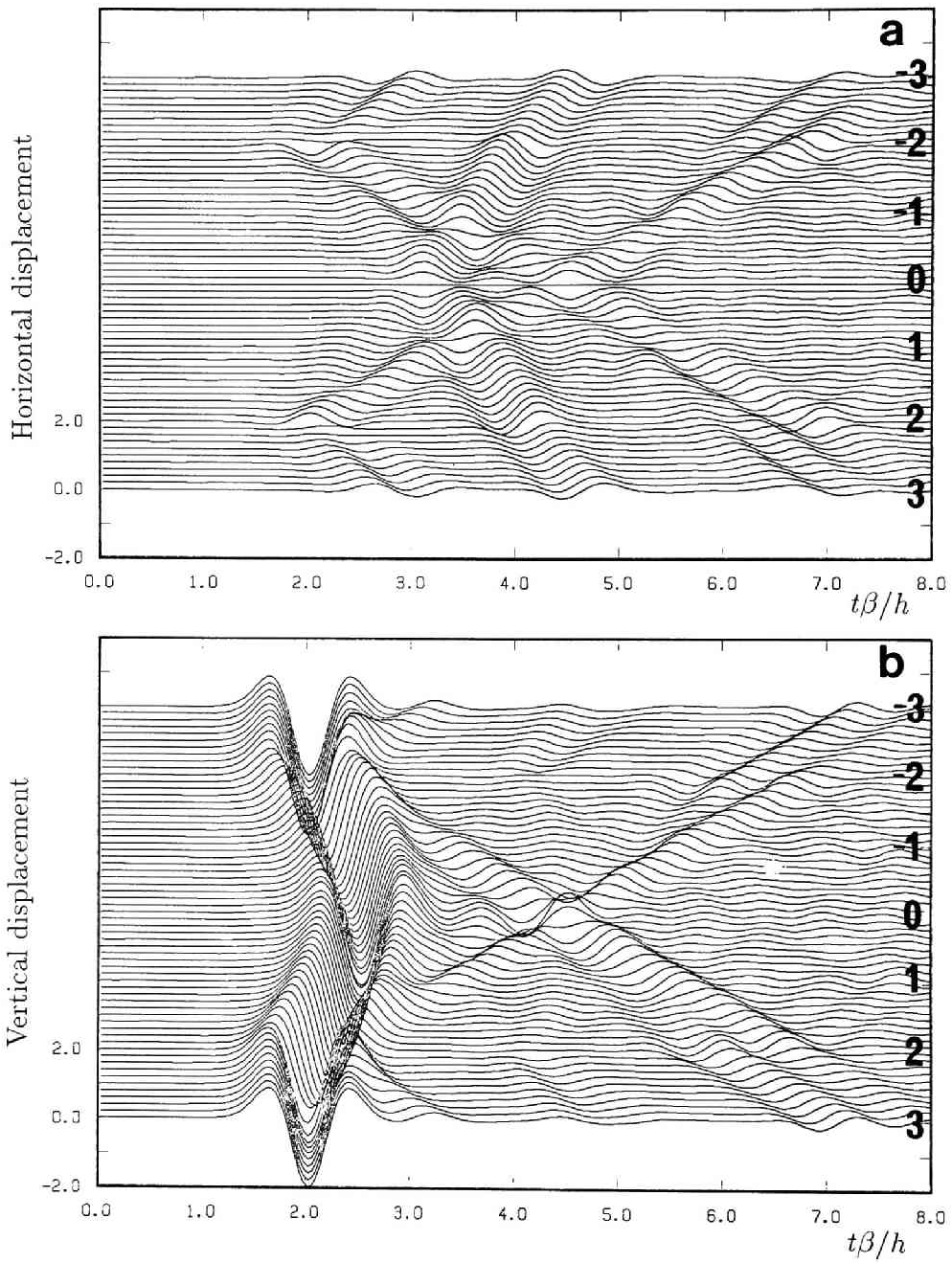

Figure 3.23: Time responses along the surface of a ridge due to a vertically incident P wave. The other conditions are the same as in Figure 3.21.

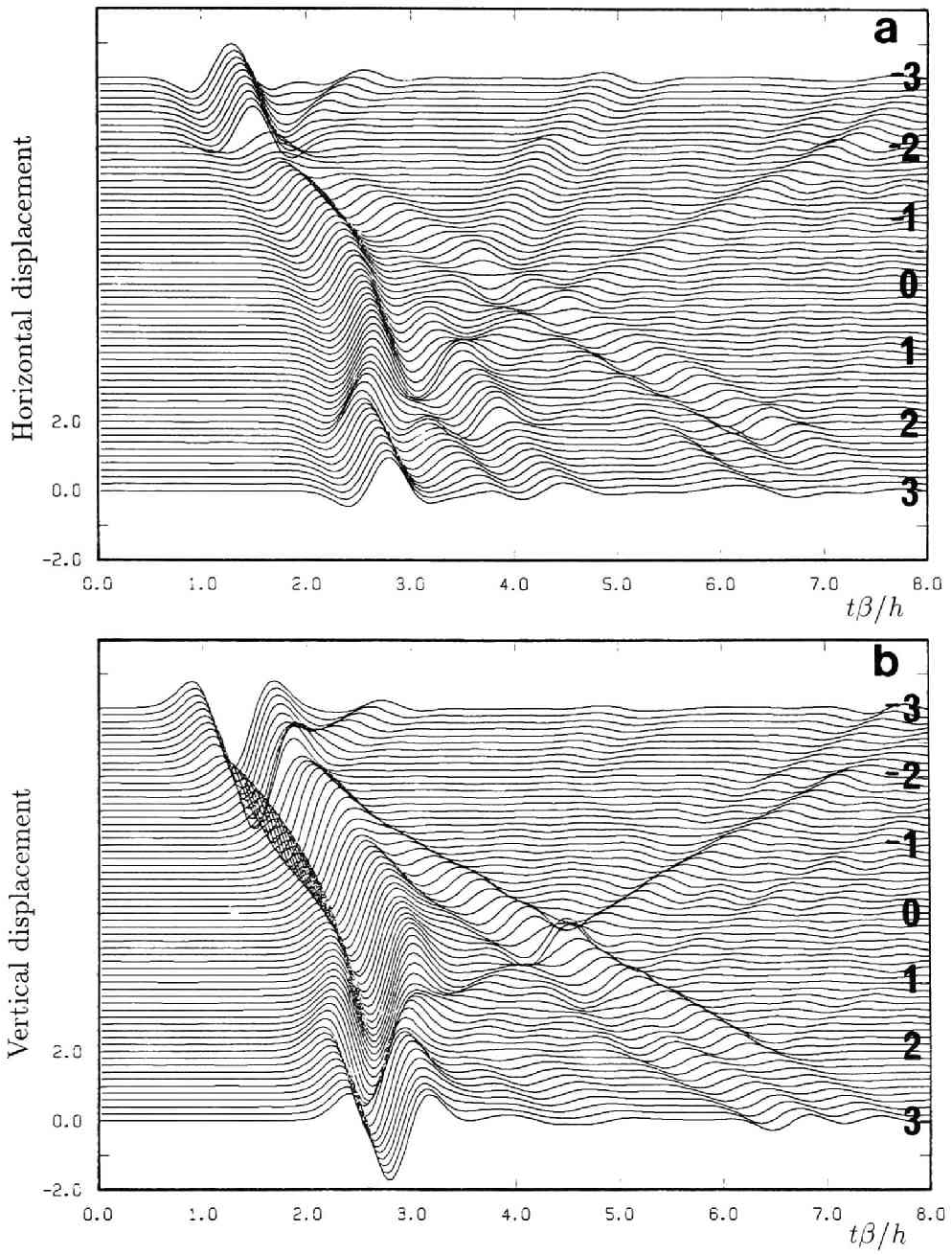

Figure 3.24: Time responses along the surface of a ridge due to an incident P wave with the angle of 30°. The horizontal and vertical free-field amplitudes for a homogeneous half-space are 0.96 and 1.74, respectively. The other conditions are the same as in Figure 3.23.

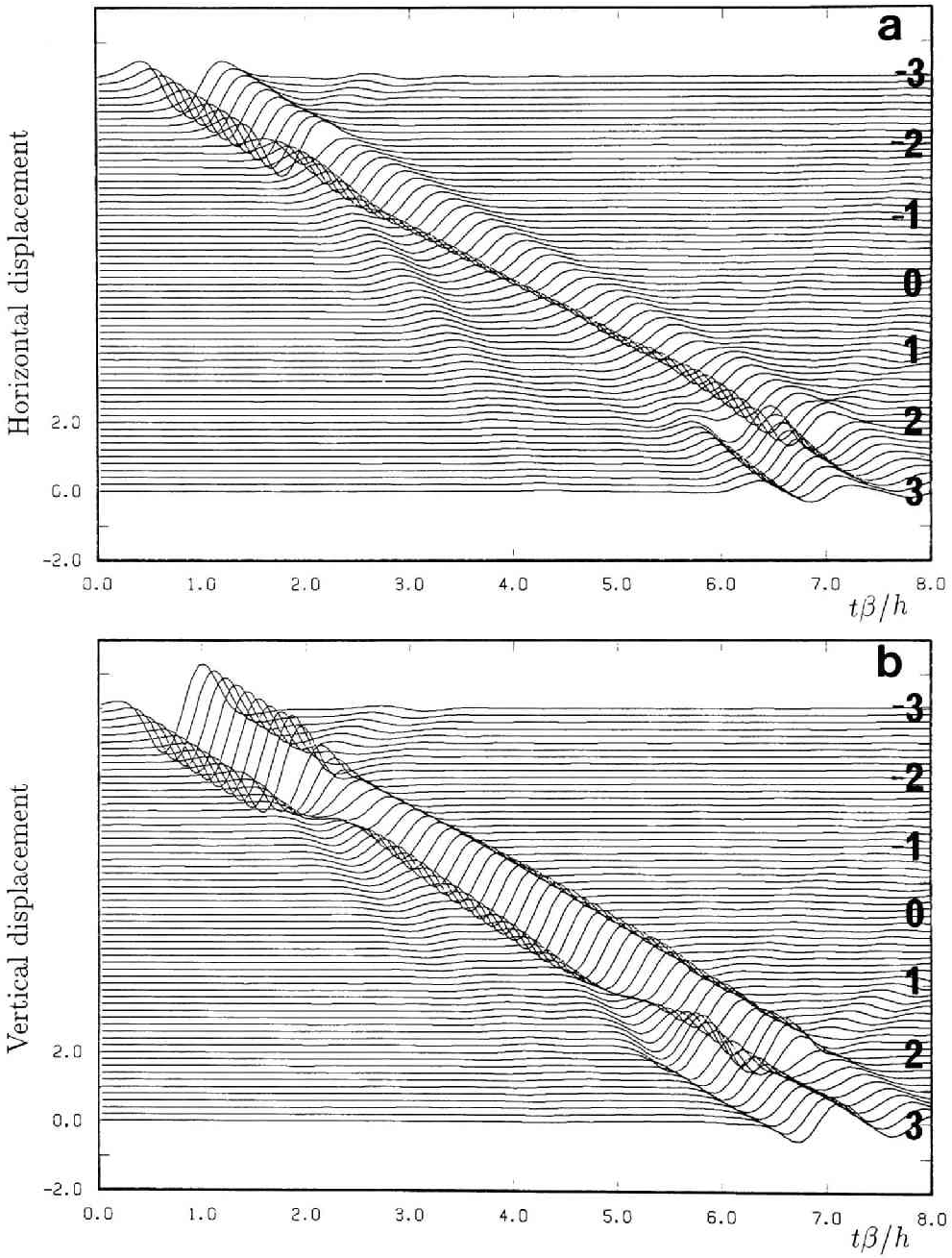

Figure 3.25: Time responses along the surface of a ridge due to a Rayleigh wave. The horizontal and vertical free-field amplitudes for a homogeneous half-space are 1.00 and 1.56, respectively. The other conditions are the same as in Figure 3.23.

Once the incident Rayleigh wave reaches at the front-side edge, its phase is shifted and its amplitude is reduced. Then it propagates along the surface of the ridge, keeping almost the same amplitude (small energy conversion between horizontal and vertical components can be seen, though). When it approaches to the rear-side edge, the earlier arrival eventually appears. Finally, on the horizontal surface at the back of the ridge, they become two clear wave-trains with equal amplitude. Although it is dangerous to judge from this figure alone, the earlier one might be the wave that propagates horizontally without being interfered very much by the ridge. The diffracted waves at the edges have negligibly small amplitude.

3.5 Summary of the results

To calculate the response in in-plane wave field more efficiently, the Discrete Wavenumber Boundary Element Method (DWBEM) for the two-dimensional wave field is developed, in which the direct boundary element method is combined with the Green function calculated by the discrete wavenumber method. The method has a strong applicability to various types of irregularities and incident waves for wide frequency range.

Since the conventional BIEM or BEM requires considerable computational effort for in-plane problems, one can hardly find results expressed in time domain for even simple topography so far. In addition conventional techniques tend to lose their stability and give inaccurate results in higher frequency range, which also prevents us from calculating the time-domain response because even small amount of error in frequency domain will result in the violation of causality in time domain. On the other hand the DWBEM is efficient in computation, owing to the discrete wavenumber Green functions, and accurate and stable even in high frequency range, owing to exact evaluation of the element integration and direct constraint for the given boundary condition. Thus the causal and physically explainable time-histories as shown here were obtained by calculating the responses for 65 different frequencies from zero up to the frequency where the wavelength corresponds to 1/4 of the canyon radius.

First the accuracy of the proposed method was successfully tested against

published results obtained in frequency domain. Then time-domain responses of canyons and a ridge subject to vertically or obliquely incident SH, SV, and P waves and a Rayleigh wave with a Ricker wavelet shape are studied. Although the shapes of the irregularities adopted in this chapter are very simple, we learned a great deal from comparing the time-domain responses of topographic irregularities due to different types of incident waves.

In all cases of incident waves impinging to a canyon, the diffracted waves originated at the edges of the canyon are observed propagating along the canyon surface with the apparent velocity of S or P waves. These waves may be called the *creeping* waves in elastodynamics, the term which has been used in electromagnetism. In most cases of inclined incidence of body waves, larger amplitude of reflected and diffracted waves is generated in front of the canyon, while the shadow zone phenomenon is observed at the back of it. The result for a Rayleigh wave with relatively short wavelength confirms the strong blocking effect by the canyon as reported in previous studies.

In case of a ridge the diffracted waves originated at the edges are again observed propagating along the ridge surface with constant apparent velocities. However, differently from the canyon, their amplitudes are increasing as they propagate.

The biggest difference between SH and SV wave incidence found is that the geometrical ray contribution (the direct and reflected waves) is dominant in the former, while the generated Rayleigh waves carry significant portion of energy in the latter. This suggests that the ray approximation will give satisfactory results for the anti-plane case as proved by Hong and Helmberger (1978), Nowack and Aki (1984), and Moczo *et al.* (1987), but that it cannot be expected to work as well in in-plane problems. It is worthy to note that among the diffracted waves generated by the ridge for in-plane problems the *creeping* Rayleigh wave, which is not seen on the canyon, has the largest amplitude.

It should be noted that the inhomogeneous P wave plays an important role in case of a critical incidence of SV wave. At the canyon surface the largest amplitude is due to the inhomogeneous P wave. At the ridge surface it becomes the earliest arrival, although its amplitude is small. Because of this energy splitting and other complex diffractions and mode conversions, the maximum amplitude in time domain

becomes smaller than the original (half-space) amplitude in case of a ridge.

Although the results shown here are limited to the cases of a Ricker wavelet incidence with a fixed characteristic frequency, the following should be noted from the comparison between the responses in time and frequency domain. The fluctuation of the amplitude along the surface in frequency domain does not always mean the fluctuation of the amplitude in time domain because the arrival-time difference of different types of waves results in the fluctuation in frequency domain even if each wave propagates with the same shape and amplitude. The time-domain response contains both amplitude and phase spectral information, and therefore expresses more complete physical picture of the wave propagation phenomena which will help to understand earthquake damages.

Chapter 4

Application to the Whittier Narrows Earthquake of 1987

4.1 Description of the problem

The Whittier Narrows, California earthquake of October 1, 1987 ($M_L = 5.9$) occurred at about 15 km east of downtown Los Angeles (34° 3.0′N, 118° 4.8′W; Jones and Hauksson, 1988) and caused the damage to approximately 10,000 buildings (Tierney, 1988; Jones and Nicolaides, 1988). The heaviest damage area was the northern part of the city of Whittier. According to Tierney (1988), about a dozen commercial buildings have been demolished and another twenty have been declared unsafe in the downtown shopping area, called Uptown or Whittier Village. The damage to residential houses was also heaviest there, especially just south of Puente Hills. The intensity VIII area in Figure 4.1, which shows the preliminary seismic intensity isoseismals based mainly on the field study (Leyendecker *et al.*, 1988), clearly reflects this.

The author and K. Aki at University of Southern California visited the area shortly after the earthquake, and was puzzled by the concentration of damage along the slope of the hill. A strong concentration of damage at the hilltop rather than on the slope is expected based on the theoretical and observational studies in the past (Aki, 1988). They observed that chimneys of houses on the hilltop were all intact, while there were many houses on the slope with toppled chimneys. Figure 4.2 shows the distribution of the heavily damaged buildings and houses in Whittier identified by the author, K. Aki, and his colleagues at University of Southern California, together with the distribution of the damaged water pipes (Schiff, 1988). The seismic intensity isoseismals in the area are also shown. This figure clearly shows the damage concentration along the southern slope of Puente Hills. K. Aki reminded the author of his lecture in "Introduction to Seismology" given a few weeks earlier

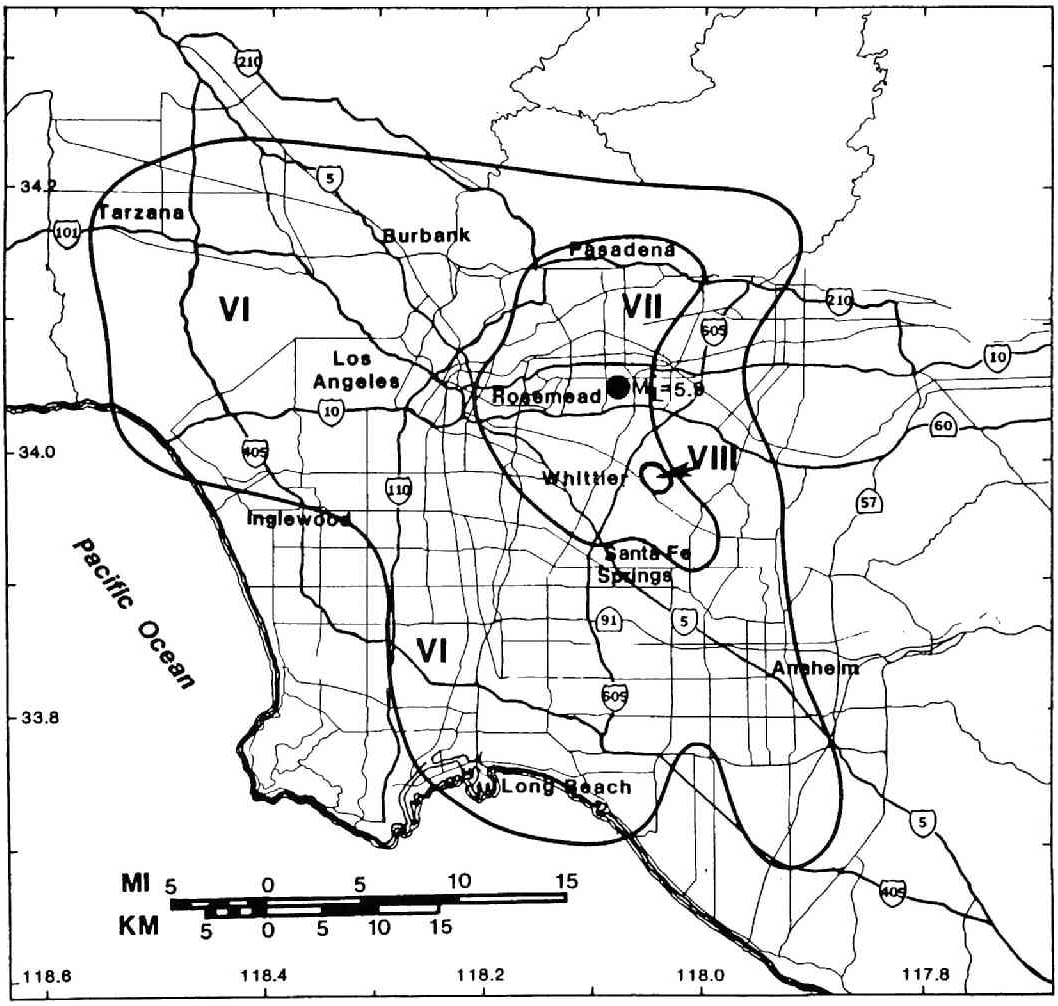

Figure 4.1: Preliminary regional Modified Mercalli intensity isoseismals in the Los Angeles area for the Whittier Narrows earthquake of October 1, 1987. The solid circle is the epicenter of the main shock. [From Leyendecker *et al.*, 1988; copyrighted by both the authors and the Earthquake Engineering Research Institute.]

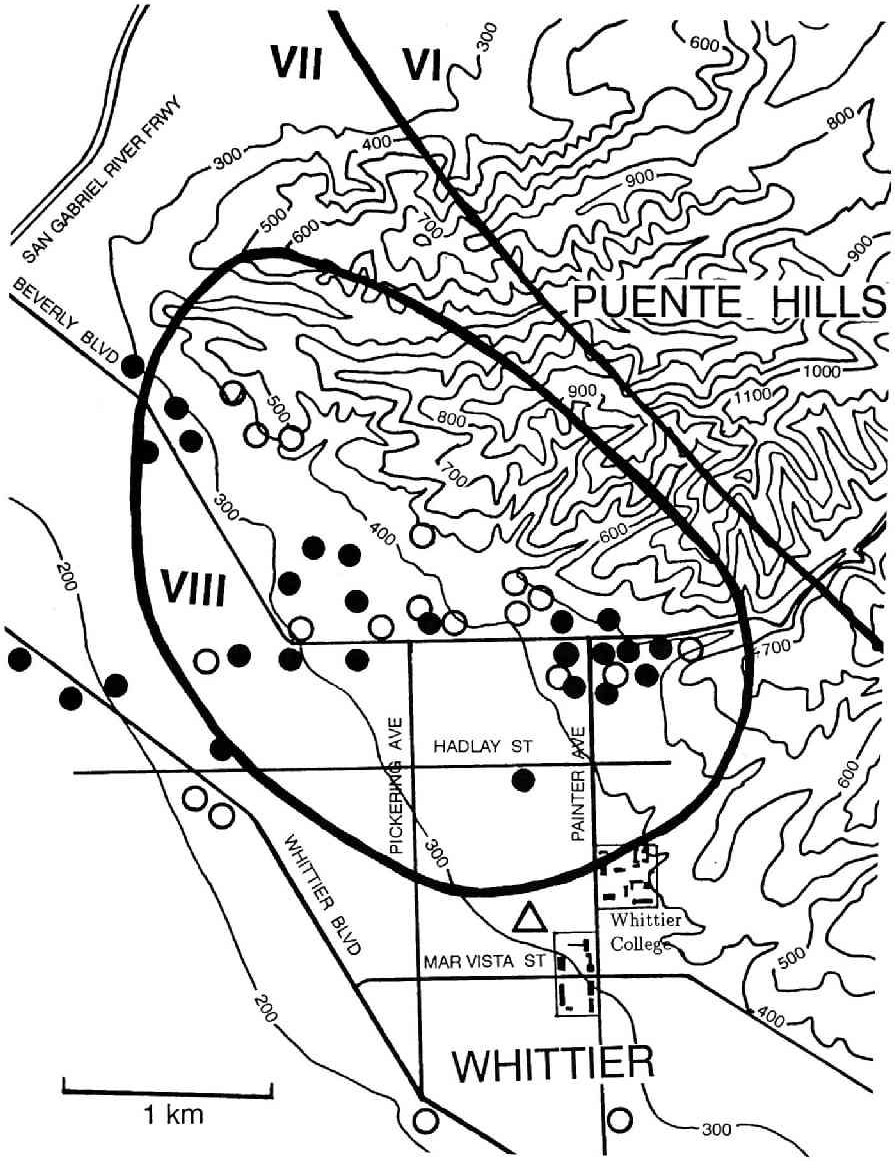

Figure 4.2: Map of downtown Whittier and Puente Hills showing contour lines of level (100 ft.) and major streets. Solid circles represent the heavily damaged buildings and houses identified by the author, K. Aki, and his colleagues at University of Southern California, while open circles represent the water pipeline damage shown in Schiff (1988). The triangle represents the approximate position of the USGS station at 7215 Bright Ave., Whittier. Thick lines show the isoseismals in Figure 4.1.

on the well-known sharp amplification effect of free-surface on an incident plane SV wave near the critical angle (i.e., the angle θ_{cr} at which $\sin\theta_{cr}$ is equal to the ratio of S wave velocity to P wave velocity). Realizing that the incident angle for the heavily damaged area in Whittier (8 to 10 km from the epicenter) roughly corresponds to the critical angle for the realistic Poisson's ratio and the reported focal depth (14±1 km; Jones and Hauksson, 1988), he suggested that the critically incident SV waves might have caused the sharply localized damage pattern in Whittier. It was soon realized that the sharp amplification for a plane SV wave incidence at the critical angle disappears if the source of an incident wave is replaced by more realistic localized sources with band-limited spectra (Aki, 1988). A possibility remained, however, that a combination of the topographic irregularity with a critically incident SV wave source may cause a sharply localized amplification. Although the amplification effects due to topographic irregularities has been studied by Boore (1972), Bouchon (1973), Bard (1982) and Tucker *et al.* (1984) among others, the possible anomalous effect by the near-critical incidence of SV waves in the epicentral region has so far escaped their attention.

The purpose of this chapter is to estimate the amplification factor due to a topographic irregularity for various types of incident SV waves with a near-critical angle to explain the anomalous damage pattern observed during the Whittier Narrows earthquake. First the observed strong motion records are examined to find if SV waves are indeed the main part of the ground motion in Whittier. Then the time-domain responses along the hill surface are calculated by using the discrete wavenumber boundary element method and the fast Fourier transform (FFT) algorithm. The method, fully described in Chapter 2, is again proved to be efficient and accurate enough to calculate the response of a hill due to various sources of incident wave field for frequencies as high as 10 Hz. The analysis is limited to the two-dimensional in-plane wave field.

4.2 Observed records examination

More than 250 strong-motion accelerograph stations were triggered by the main shock of the Whittier Narrows earthquake (Brady *et al.*, 1988a) and records ob-

Table 4.1: Peak Values at the Station 7215 Bright Ave., Whittier

		NS-direction	EW-direction	UD-direction
Acceleration (cm/sec^2)	10th floor	−417.9	514.0	549.4
	5th floor	−539.5	−600.9	345.0
	Basement	−381.9	−606.7	245.5
Velocity (cm/sec)	10th floor	43.7	−33.4	−11.4
	5th floor	35.3	−24.2	10.3
	Basement	26.6	−27.7	− 7.6
Displacement (cm)	10th floor	7.3	3.9	1.0
	5th floor	5.8	−3.1	− 1.0
	Basement	3.9	−2.5	0.8

served at twelve stations by the California Division of Mines and Geology (CDMG) and seven stations by the U.S. Geological Survey (USGS) have already been released as digitized data (Shakal *et al.*, 1987; Brady *et al.*, 1988b). First the records obtained at the nearest station to downtown Whittier shall be examined to see how much the records at the basement were affected by the building vibration.

The nearest station to downtown Whittier is the USGS station No.4 in Brady *et al.* (1988a), a ten-story reinforced concrete building at 7215 Bright Ave., Whittier. It is located 8.0 km south and 4.1 km east of the epicenter. The triangle in Figure 4.2 represents the approximate position of the station. Figure 4.3 shows the accelerograms recorded at the basement, 5th, and 10th floors of the building. Peak acceleration, velocity and displacement are summarized in Table 4.1. No ground level records were provided at this station. The accelerograms have a common predominant frequency of about 4 Hz in the EW direction or 2 Hz in the NS direction. These predominant frequencies higher than expected for the fundamental mode of a ten-story building and the peak accelerations at the 5th floor larger than those at the 10th floor suggest that the second mode of the building vibration dominates.

To confirm this we calculate the system functions $H(\omega)$ of the upper two levels

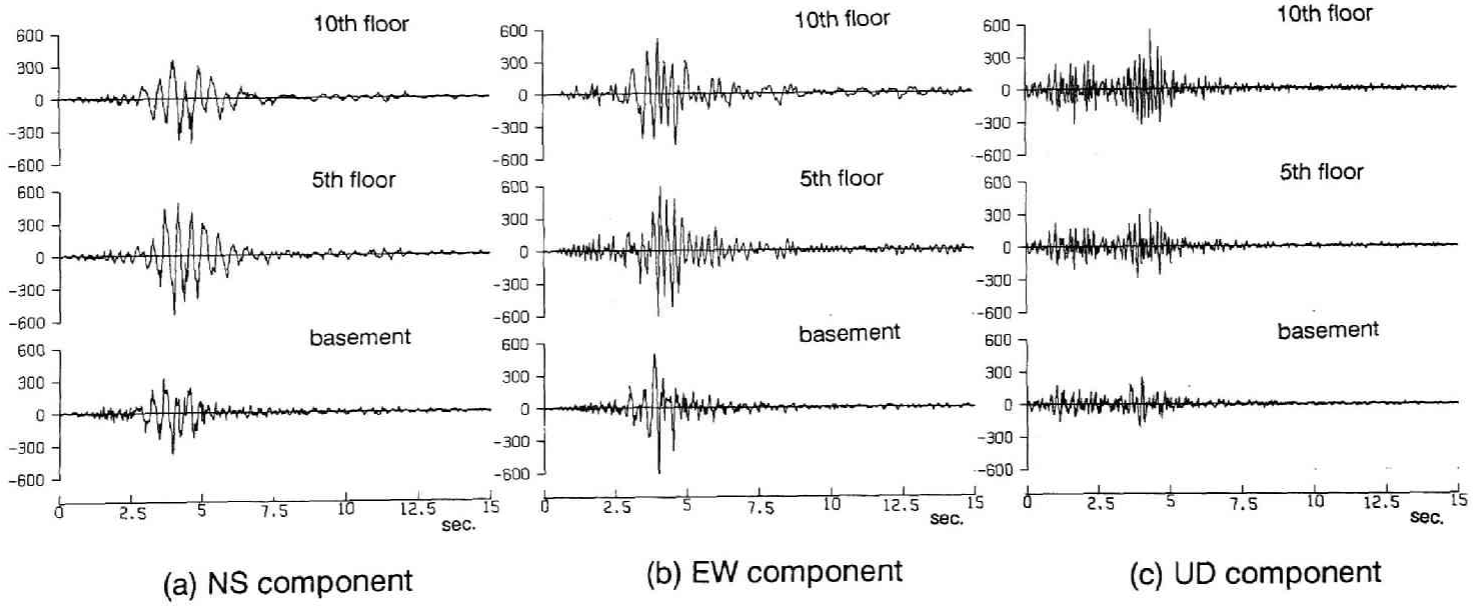

Figure 4.3: Accelerograms recorded at the basement, 5th, and 10th floors of the building at 7215 Bright Ave., Whittier. **a**: NS component; **b**: EW component; **c**: UD component.

to the basement by the following formula:

$$H(\omega) = \frac{S_{bu}(\omega)}{S_{bb}(\omega)} , \tag{4.1}$$

where, $S_{bb}(\omega)$ is the power spectrum of the basement acceleration and $S_{bu}(\omega)$ is the cross spectrum between the upper level and the basement. The Parzen window of 0.2 Hz is used. Figure 4.4 shows the absolute value of the system functions for the NS and EW components together with the power spectra at the basement. Considering that the system function represents the dynamic characteristics of the structure with a fixed base, we conclude:

i) The natural frequencies of the structure are 0.67 Hz and 2.0 Hz in the NS direction and 1.4 Hz and 4.1 Hz in the EW direction.

ii) The peak amplitudes are increasing with level in the first mode, while they are decreasing in the second mode.

iii) The NS-direction power spectrum at the basement has only one prominent peak at 2.4 Hz, while the EW-direction power spectrum has two peaks at 2.4 Hz and 3.7 Hz.

It is well known that the basement response has troughs at the natural frequencies of the structure itself but has peaks at the natural frequencies of the total soil-structure system, which are always lower than the former (e.g., Trifunac, 1972; Wolf, 1985). Since the second peak frequency 3.7 Hz in the EW-direction power spectrum is a little lower than the second natural frequency of the structure 4.1 Hz and it appears only in the EW direction, it must be due to the effect of the structure, rather than the property of the input ground motion. Particle motions for band-pass filtered basement accelerograms in Figure 4.5 show that the major axes of motion lie between NW and NNW direction for the most frequency ranges except for the range from 2.5 Hz to 5.0 Hz where EW motion dominates. Thus we conclude that the basement accelerograms of the nearest station to downtown Whittier are strongly modified by the structural response, and we cannot use them for our purpose.

Other stations in the epicentral area, however, may be used to find if SV waves are the main part of the strong ground motion. We selected twelve stations of the

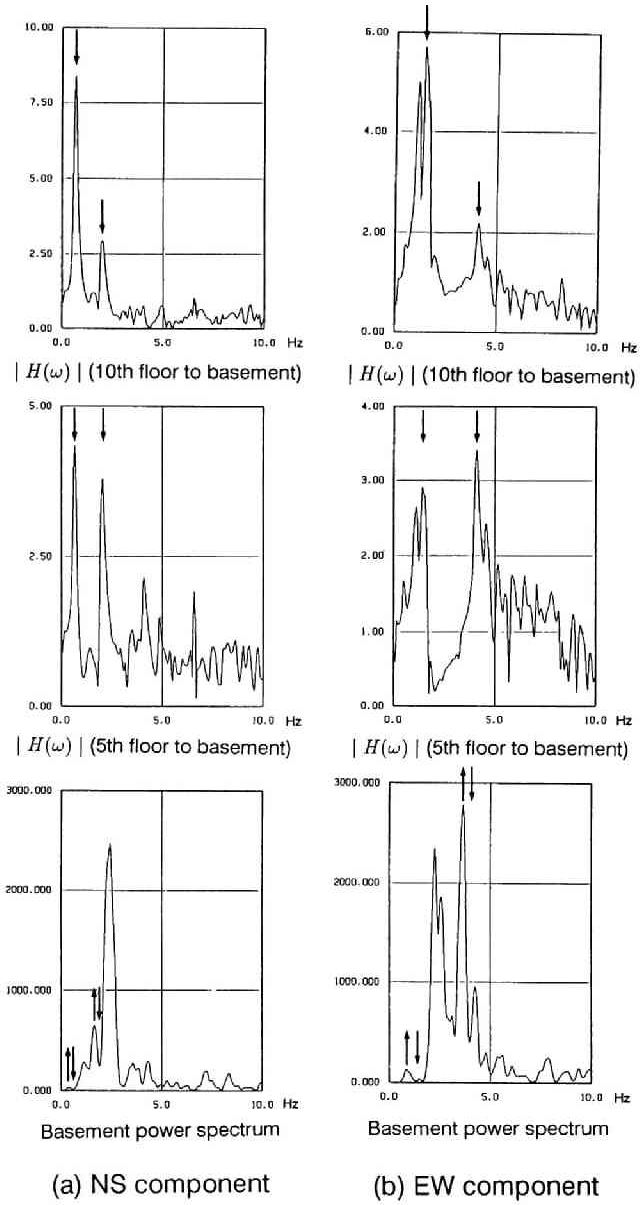

Figure 4.4: The absolute value of the system functions for the 10th and 5th floor accelerograms with respect to the basement accelerogram observed at 7215 Bright Ave., Whittier. Power spectra of the basement accelerograms are plotted in the bottom. **a**: NS component; **b**: EW component. A Parzen window with the bandwidth of 0.25 Hz is used. Down arrows and up arrows in the figure indicate the inferred natural frequencies of the structure itself and those of the total soil-structure system, respectively.

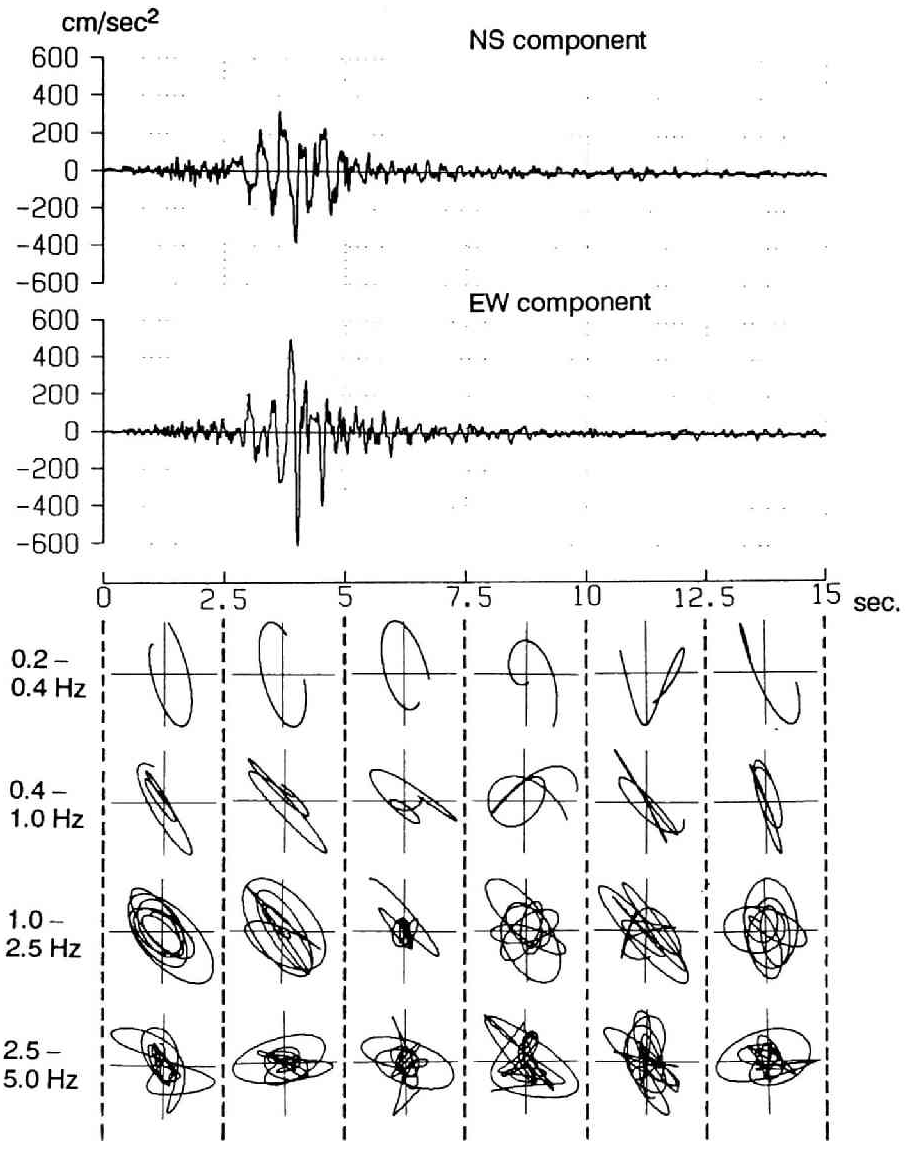

Figure 4.5: Particle motions and time-histories of the accelerograms recorded at the basement of the building at 7215 Bright Ave., Whittier. Particle motions projected in the horizontal plane (north upward) are shown for the band-pass filtered records in the frequency ranges of (top) 0.2 Hz–0.4 Hz, (upper middle) 0.4 Hz–1.0 Hz, (lower middle) 1.0 Hz–2.5 Hz, and (bottom) 2.5 Hz–5.0 Hz. They are normalized in each 2.5 sec time-window.

Table 4.2: Station Locations and Directions of Principal Axis

Station Name	Coordinate North & East (km)	Epicentral distance (km)	Principal axis from north* Obs./Cal.
ALTA: Altadena, Eaton Canyon Park	(14.2, −1.4)	14.3	4°/3°
SANM: San Marino, Southwestern Academy	(7.3, −4.5)	8.6	358°/359°
FREM: Alhambra, 900 S. Fremont Blvd.	(4.5, −6.4)	7.8	343°/352°
FRES: Alhambra, Fremont School	(2.3, −6.4)	6.8	331°/343°
GARV: Garvey Reservoir, Abutment Bldg.	(0.1, −2.7)	2.7	348°/345°
OBRE: Los Angeles, Obregon Park	(−1.3, −8.9)	9.0	322°/308°
DAMU: Whittier Narrows Dam, Upstream	(−2.1, 2.9)	3.6	45°/19°
VERN: Vernon, 4814 Loma Vista Ave.	(−5.5, −11.0)	12.3	45°/74°
BELL: Bell, L.A. Bulk Mail Center	(−6.6, −7.3)	9.8	106°/50°
BRIG: Whittier, 7215 Bright Ave.	(−8.0, 4.1)	9.0	317°/340°
DOWN: Downey, County Maintenance Bldg.	(−13.9, −7.9)	16.0	28°/13°
NORW: Norwalk, 12400 Imperial Highway	(−14.3, 1.0)	14.3	340°/359°

* The principal axis, measured clockwise from the north, has ±180° ambiguity.

CDMG and USGS which meet the condition that the epicentral distance $\leq$ 20 km and the peak acceleration $\geq$ 0.2 g. The station names and location coordinates relative to the epicenter are listed in Table 4.2. All stations are on the ground or on the basement of a small building except for the stations BRIG: Whittier–7215 Bright Ave. and FREM: Alhambra–900 South Fremont Blvd. We then determine the directional distribution of energy in the horizontal plane by using the following formula (Takizawa, 1982). First we calculate the total power and cross spectra of the two orthogonal components n (referring to north) and e (referring to east) in the frequency range of interest:

$$[E] = \int_{\omega_1}^{\omega_2} Re \begin{bmatrix} S_{nn}(\omega), & S_{ne}(\omega) \\ S_{en}(\omega), & S_{ee}(\omega) \end{bmatrix} d\omega \ , \tag{4.2}$$

where, $S_{nn}(\omega)$ is a power spectrum of the n direction velocity and $S_{ne}(\omega)$ is a cross spectrum between the n and e direction velocities, and so on. Then the energy in the direction ϕ measured clockwise from the n-axis can be obtained as

$$E_\phi = \{\cos\phi, \sin\phi\}\,[E] \begin{Bmatrix} \cos\phi \\ \sin\phi \end{Bmatrix} . \tag{4.3}$$

This energy distribution will be two elliptic lobes in line with the principal axis if the ground motion is unidirectional, while it will become a single circle if the ground motion is not directional at all. Figure 4.6 shows the energy distributions for the records observed at twelve stations. Note that the unidirectional motion is clearer in the northern and southern stations.

In Figure 4.7 the same energy distributions are plotted for the theoretical ground motions calculated by the Haskell-type fault with uniform slip distribution in a three-dimensional unbounded medium, whose P and S wave velocities are assumed to be 4.2 km/sec and 2.4 km/sec. The assumed fault parameters are chosen referring to Hauksson *et al.* (1988) and summarized in Table 4.3. The fault strike is east-west and slip direction north-south. The calculated principal directions show a remarkable agreement with those observed. At all stations except BELL: Bell–L.A. Bulk Mail Center the difference between the observed and calculated principal axes is less than 30° as shown in Table 4.2. This good agreement may indicate the effectiveness of a relatively simple source model as the results of Wald *et al.* (1988) and

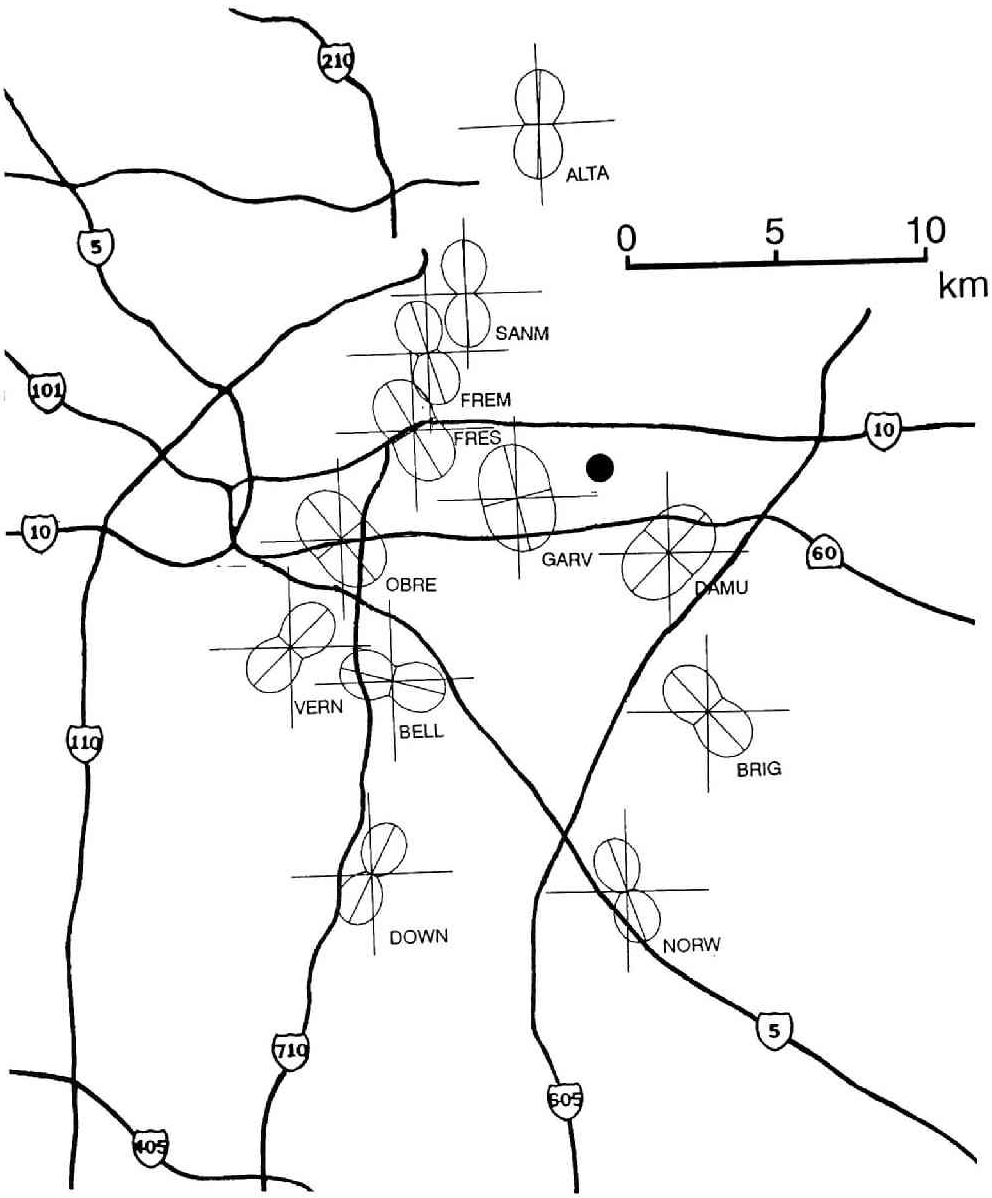

Figure 4.6: Energy distributions in the horizontal plane for the records observed at twelve stations within 20 km from the epicenter. The solid circle is the epicenter of the main shock. The station names and location coordinates are listed in Table 4.2. The distribution will be two elliptic lobes in line with the major axis if the ground motion is unidirectional, or a single circle if the ground motion is not directional at all.

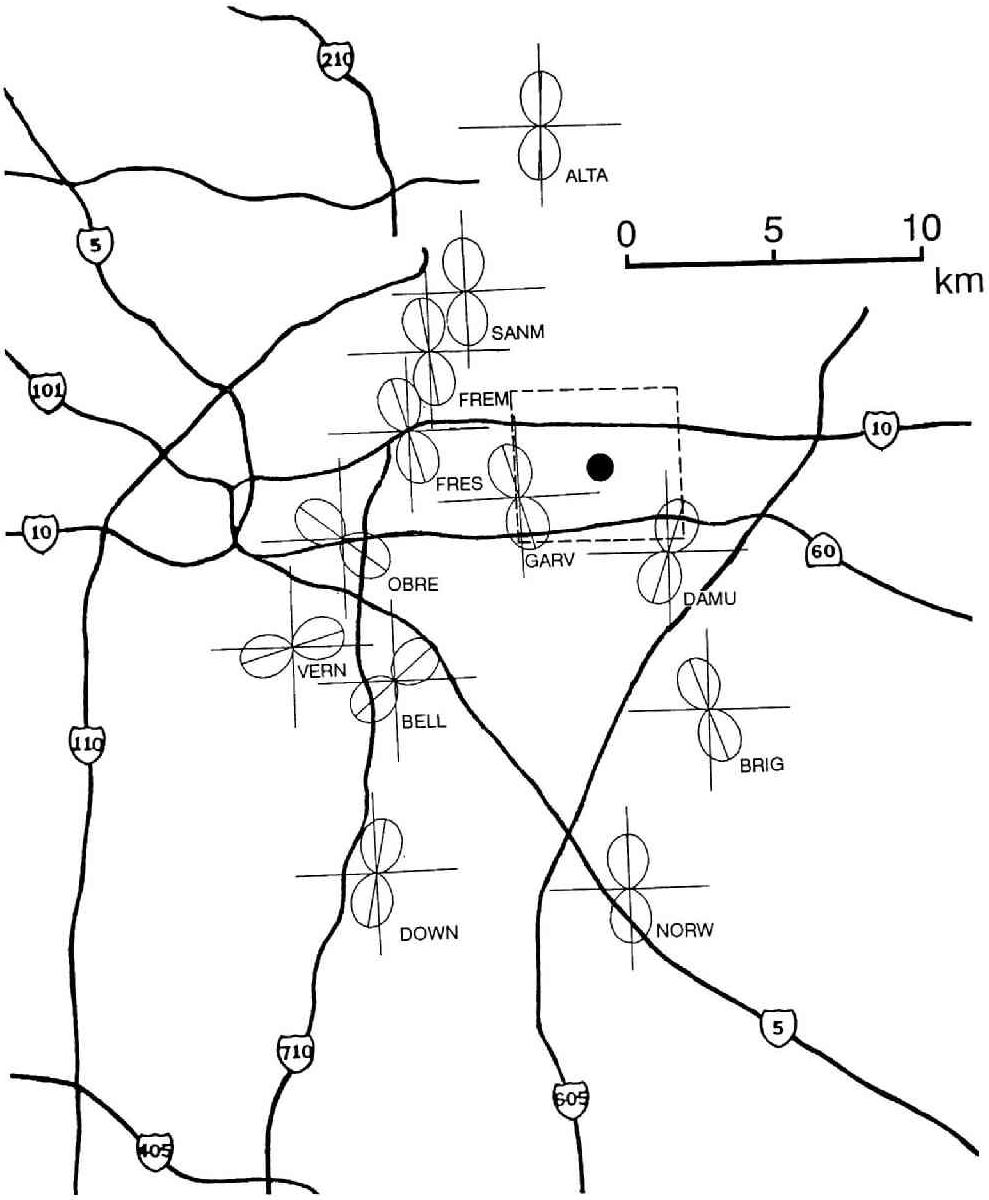

Figure 4.7: Energy distributions in the horizontal plane for the synthetics calculated at the same stations in Figure 4.6. Fault parameters of the 3D Haskell model used here are summarized in Table 4.3. The assumed rupture area is shown by the broken line.

Table 4.3: Fault parameters used for a 3D Haskell model

Rupture pattern	Depth of hypocenter (km)	Fault size L × W (km)	Dip angle	Rupture speed (km/sec)	Rise time (sec)	Final slip (m)	Seismic moment (dyne·cm)
radial	12.0	6.0×6.0	30°	2.0	0.25	1.0	0.5×10^{25}

Vidale (1989) have also suggested. The reason why the station BELL is exceptional may be because it lies close to the nodal plane so that the principal direction of motion could be affected strongly by other factors such as source complexity.

From the study of the principal axis it is found that the radial component is dominant in the southern stations. To confirm that the incident wave is mainly composed of SV waves at those stations, it is helpful to compare the correlation of the radial and vertical components with that of the transverse and vertical components. As an example we show the particle motions of the filtered velocity records observed at NORW: Norwalk–12400 Imperial Highway in Figure 4.8. Good correlation can be seen in the radial-plane projection as elliptic patterns represent, while random motion patterns are observed in the transverse-plane projection. Other stations such as DAMU: Whittier Narrows Dam, Upstream or DOWN: Downey–County Maintenance Bldg. show the same patterns as in Figure 4.8. This fact and the arrival time suggest that the major portion of the ground motion is mainly composed of SV waves. Since the difference of the azimuthal angle between these stations and BRIG is small and the waveforms of the theoretical synthetics are very similar to each other, we conclude that the assumption of the SV wave dominance in downtown Whittier seems quite reasonable. Dominant direction of motion at BRIG shown in Figure 4.5 also supports the assumption except for the frequency range of 2.5–5.0 Hz.

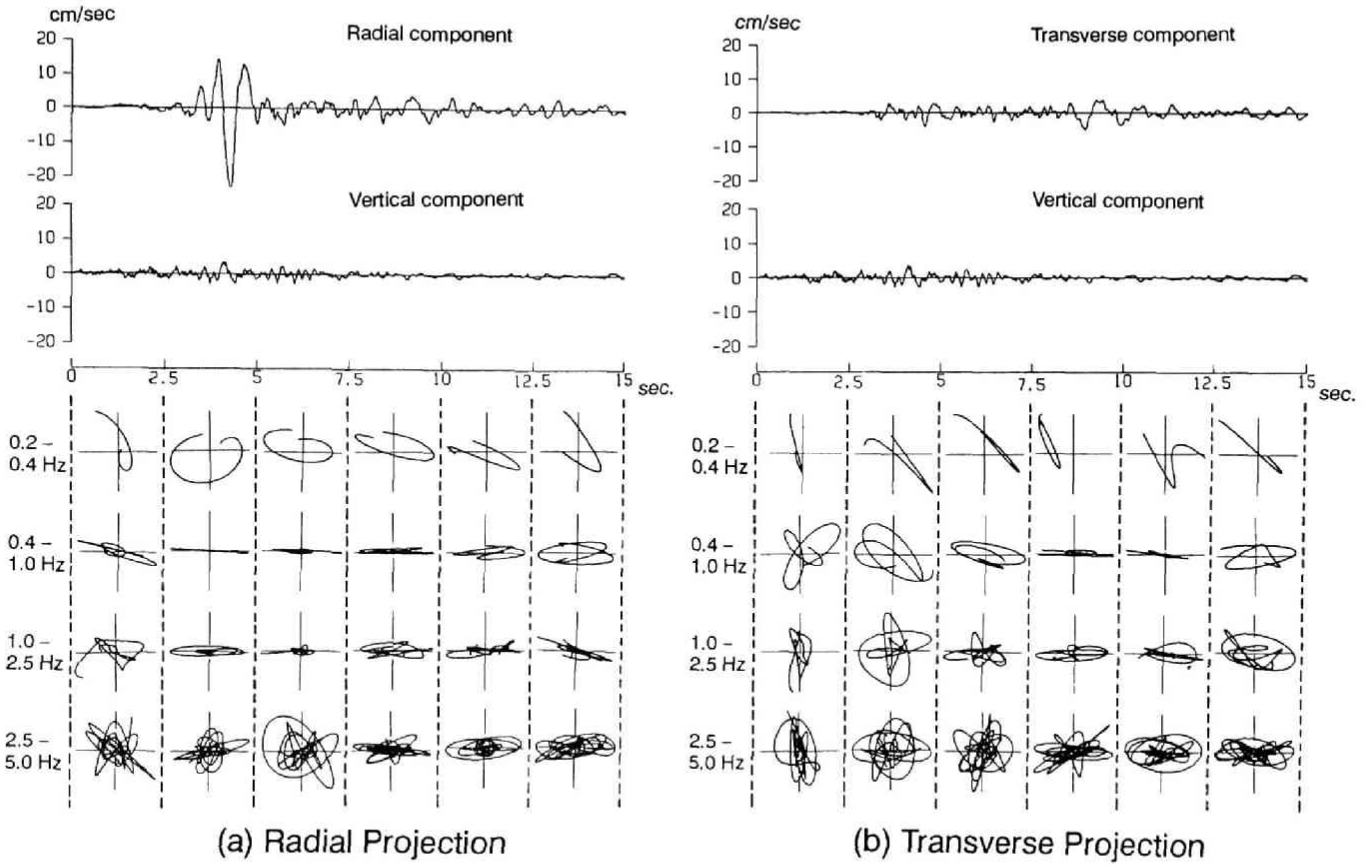

Figure 4.8: Particle motions of the observed velocity records at the station NORW projected to the vertical planes in the radial direction (**a**) and in the transverse direction (**b**). The records are band-pass filtered in the four frequency ranges and normalized in each 2.5 sec time-window.

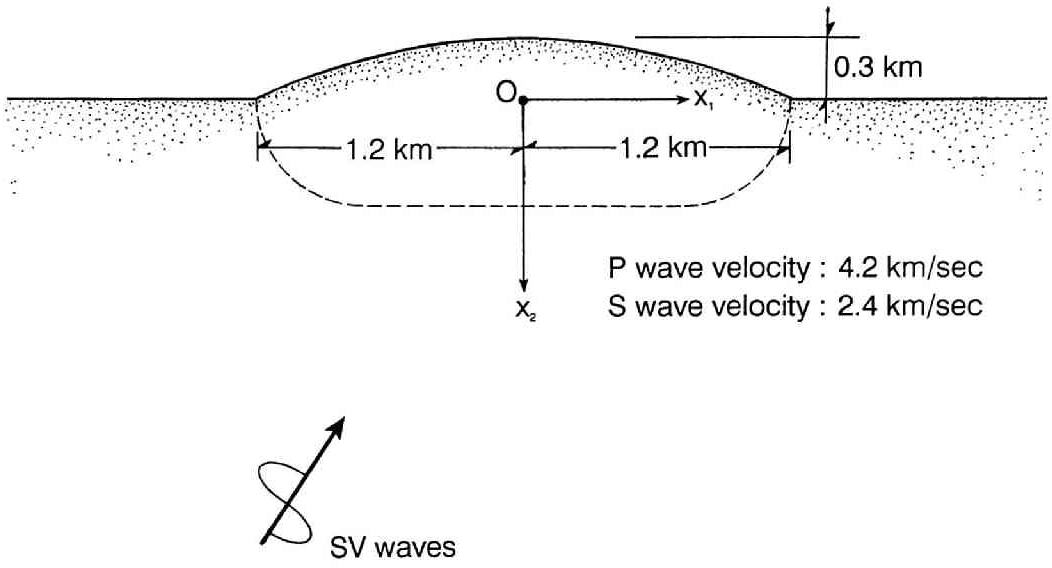

Figure 4.9: Model of a shallow hill used in the analysis. The dashed line shows the interface between the irregular region and the surrounding half-space. Responses at the surface of the hill and the surrounding soil within ±2.4km are calculated.

4.3 Models of source and medium

The method for calculating synthetic seismograms is the discrete wavenumber boundary element method described in the previous chapter. As in the section 3.4 we divide the medium into two regions, an irregular region and a surrounding one. For the irregular region we use Green function for a homogeneous unbounded medium. This region is enclosed by the boundary elements, including the free-surface with non-flat topography. For the surrounding region, we use Green function for a homogeneous half-space calculated by the discrete wavenumber method. These two regions are connected by the boundary elements on the interface which can be placed arbitrarily as shown in Figure 4.9.

The topography of the hill in our model has the height 0.3 km and the width 2.4 km, approximating the actual geometry of Puente Hills shown in Figure 4.2. The shape of the hill is assumed to be a circular arc of radius 2.55 km. The P and

S wave velocities are assumed to be 4.2 km/sec and 2.4 km/sec, respectively. The following four types of sources for incident wave field are considered:

(a) a plane SV wave at near-critical incidence,

(b) a horizontal line force located at the assumed hypocenter (−8 km, 12 km), and

(c) two-dimensional dip-slip faults of

(c1) Haskell-type with a uniform slip distribution (Haskell, 1964), and

(c2) Bouchon-type with multiple cracks (Bouchon, 1978).

They are shown schematically in Figure 4.10. The fault parameters used for the cases (c1) and (c2) are listed in Table 4.4. The theoretical expressions for these kinematic fault models are summarized in Appendix. For the case (a) the incidence angle is set to be 33.7°, which corresponds to the direction from the assumed hypocenter (−8 km, 12 km) to the hill center. Hereafter we call the left-hand side of the hill as near-side and the right-hand side as far-side relative to the hypocenter. Figure 4.11 shows the slip distributions and the rupture propagation patterns for both Haskell-type and Bouchon-type fault models.

4.4 Synthetic seismograms

The synthetic seismograms along the surface of the hill and the surrounding half-space within ±2.4 km will be shown for the above four types of incident wave field. In cases of a plane SV wave and a line force we assume the source time function of a Ricker wavelet defined as

$$u(t) = (2\pi^2 f_c^{\,2} t^2 - 1)\exp(-\pi^2 f_c^{\,2} t^2) \ , \tag{4.4}$$

where f_c is the characteristic frequency. The shape and spectra are shown in Figure 3.7.

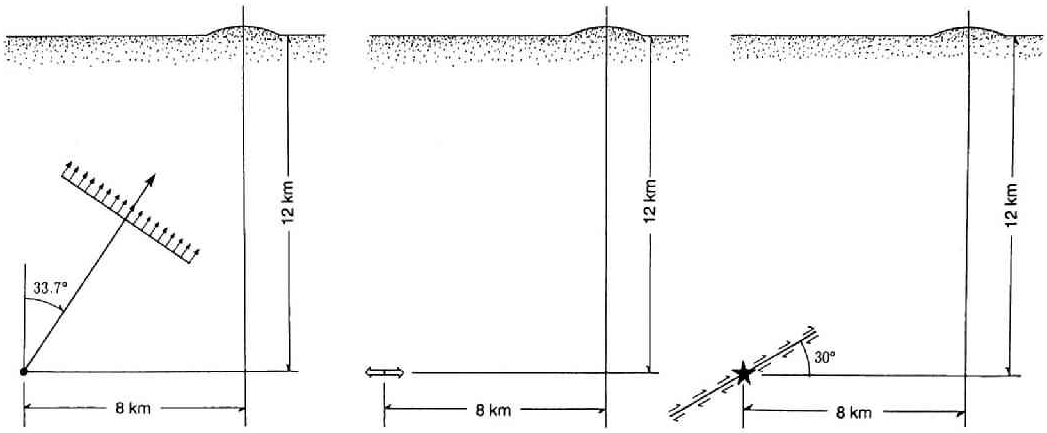

(a) A plane SV wave (b) A horizontal line force (c) 2D kinematic faults

Figure 4.10: Four types of sources for the incident wave field are considered and compared, that is, (a) a plane SV wave with nearly critical angle of incidence 33.7°, which corresponds to the direction from the assumed hypocenter to the hill center, (b) a horizontal line force located at the hypocenter (−8 km, 12 km), and (c) 2D kinematic faults, whose rupture patterns are of Haskell-type with a uniform slip distribution (c1), or, Bouchon-type with multiple cracks (c2). See Table 4.4 for the fault parameters used in the cases (c).

Table 4.4: Fault parameters used for 2D fault models

Fault type	Depth of hypocenter (km)	Fault length Upper (km)	Fault length Lower (km)	Dip angle	Rupture speed (km/sec)	Rise time (sec)	Maximum slip (m)
Haskell	12.0	3.0	3.0	30°	2.0	0.25	1.00
Bouchon	12.0	3.0	3.0	30°	2.0	—*	1.27

* Source time function is determined by the pattern of crack growth. Each crack freezes in 0.25 sec.

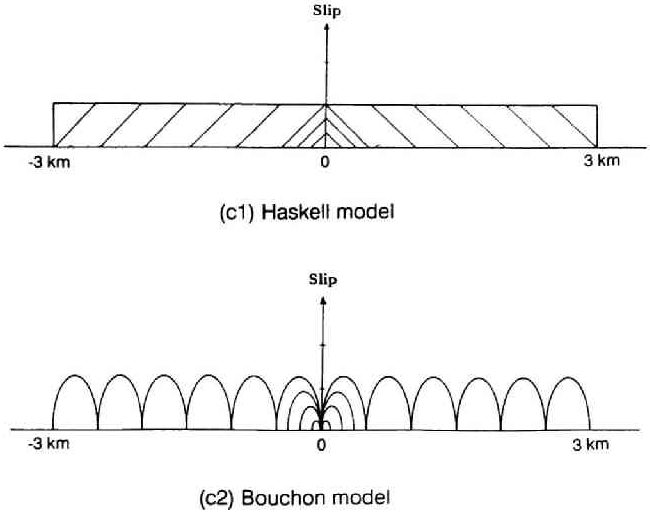

Figure 4.11: Slip distributions and rupture propagation patterns for (c1) the Haskell-type fault and (c2) the Bouchon-type fault. See Appendix for formulation.

4.4.1 Plane SV wave incidence

Figure 4.12 shows the synthetic seismograms for a plane SV wave with the angle of incidence 33.7°. Synthetics for a duration of 10 sec with a time delay of 4 sec are plotted. The characteristic frequency f_c is set to be 4 Hz. The uppermost seismogram shows the response at $x_1 = -2.4$ km. The seismograms at locations from -1.2 km to $+1.2$ km correspond to the hill surface. The lower side of the figure shows the responses of the far-side of the hill, with the lowermost one corresponding to $x_1 = +2.4$ km.

The amplification along the far-side slope of the hill is observed. The maximum amplitude increases as the observation point moves from the hilltop to the far-side edge. Along the near-side slope deamplification is clearly seen. The flat surface of the surrounding half-space seems little affected by the topography. These amplitude characteristics are stable with respect to the spectral content of the source time function as shown in Figure 4.13, where we plot the peak amplitude distributions along the surface for different characteristic frequencies $f_c = 2$ Hz, 3 Hz, and 4 Hz. The amplification factor reaches about 1.6 near the far-side edge, which seems

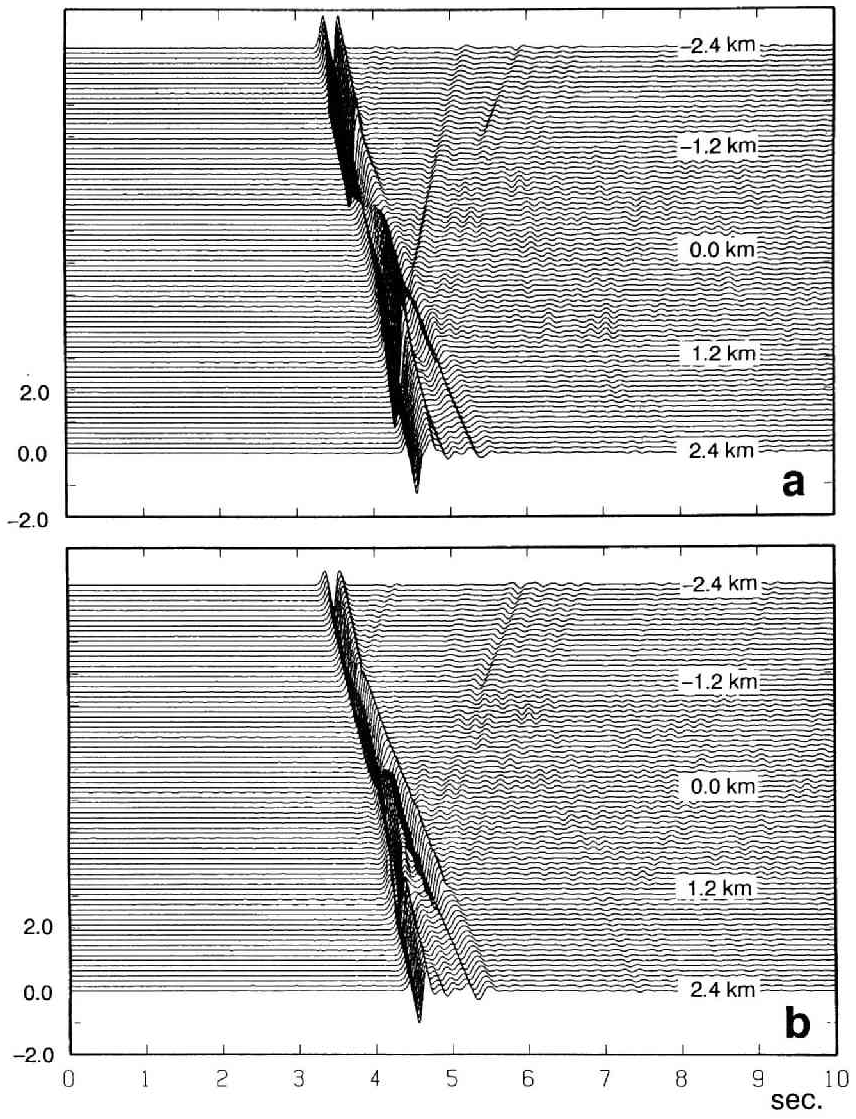

Figure 4.12: Synthetic seismograms along the surface of the hill and the surrounding soil for a plane incident SV wave with a Ricker wavelet of the characteristic frequency f_c=4 Hz. **a**: horizontal component; **b**: vertical component. The horizontal coordinate x_1 is shown in the right-hand side. The separation distance between two successive traces is approximately 60 m. Frequency spectra are calculated for every 0.05 Hz interval from 0 Hz to 10 Hz, and then transformed into time-histories by FFT. Amplitude is normalized to that of the incident wave.

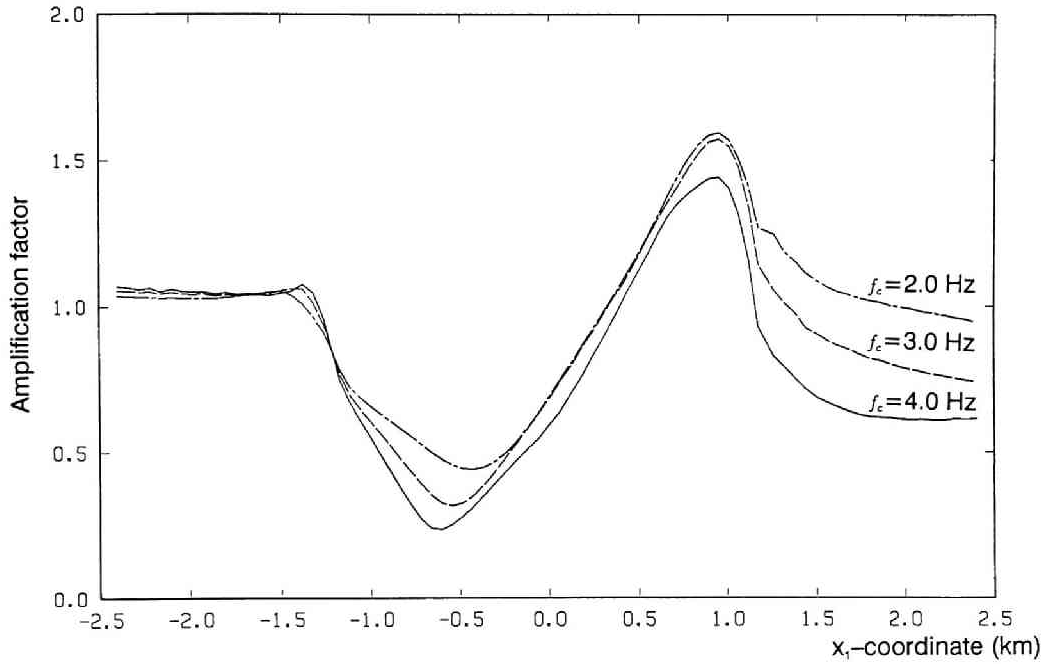

Figure 4.13: Maximum amplitude distribution along the surface of the hill and the surrounding soil for plane SV waves with characteristic frequencies f_c of 2 Hz, 3 Hz, and 4 Hz. Amplitude is normalized to that of a half-space, 2.06.

surprisingly large for the effect of a 0.3 km hill. Its position seems also unusual because the largest amplification at or near the hilltop is observed if not critical SV-wave incidence (Bouchon, 1973; Bard, 1982). For an exactly critical SV wave incidence Bard (1982) has reported a deamplification near the hilltop relative to the flat surface response. The author has already discussed in Chapter 3 the mechanism that causes this deamplification.

4.4.2 Horizontal line force

To see the effect of cylindrical wave field in comparison to plane SV wave field, displacement due to a horizontal line force are shown in Figure 4.14 in the same manner as in Figure 4.12. Synthetics for a duration of 10 sec starting with the origin time are plotted. The similar amplification along the far-side slope can be seen. The peak amplitude distributions along the surface in Figure 4.15 also have very similar characteristics to those in Figure 4.13 for a plane SV wave. The maximum amplification factor reaches 1.9 for $f_c = 3$ Hz. As mentioned earlier, the critical incidence effect on a flat surface disappears in this frequency range if the plane wave is replaced by a line force (Aki, 1988). It is noticeable, therefore, for a line force to give similar amplification characteristics to those for the plane wave on an elevated surface. This stability to the incident wave field as well as the source spectrum encourages us to attribute the observed damage concentration to the surface topography coupled with the near-critical incidence.

4.4.3 Haskell-type fault

In order to see if these characteristics are also observed for more realistic earthquake sources, first we calculate the response for a Haskell-type kinematic fault with a uniform slip distribution. Rupture starts at the center of the 6 km fault and propagates bilaterally with a constant velocity of 2.0 km/sec. The rise time (Aki and Richards, 1980) is assumed to be 0.25 sec. Since damage of structures represented by the ductility factor is well correlated with the input energy, hence with the maximum ground velocity (Newmark and Rosenblueth, 1971), we plot velocity seismograms along the surface in Figure 4.16. Synthetics for a duration of 15 sec starting with the earthquake origin time are shown.

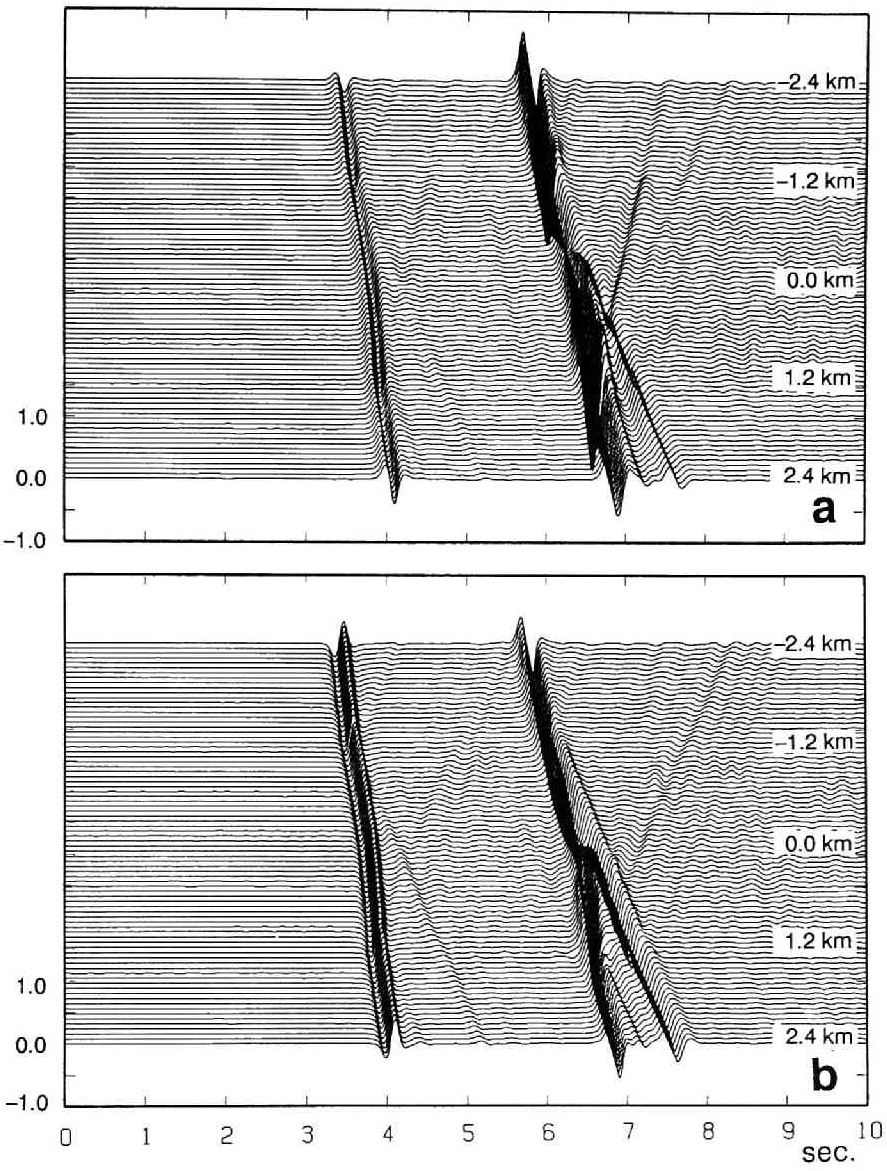

Figure 4.14: Displacement seismograms along the surface of the hill and the surrounding soil for a horizontal line force located at the assumed hypocenter (−8 km, 12 km) with a Ricker wavelet of the characteristic frequency f_c=4 Hz. Amplitude is meaningful only as a relative value. The other conditions are the same as Figure 4.12.

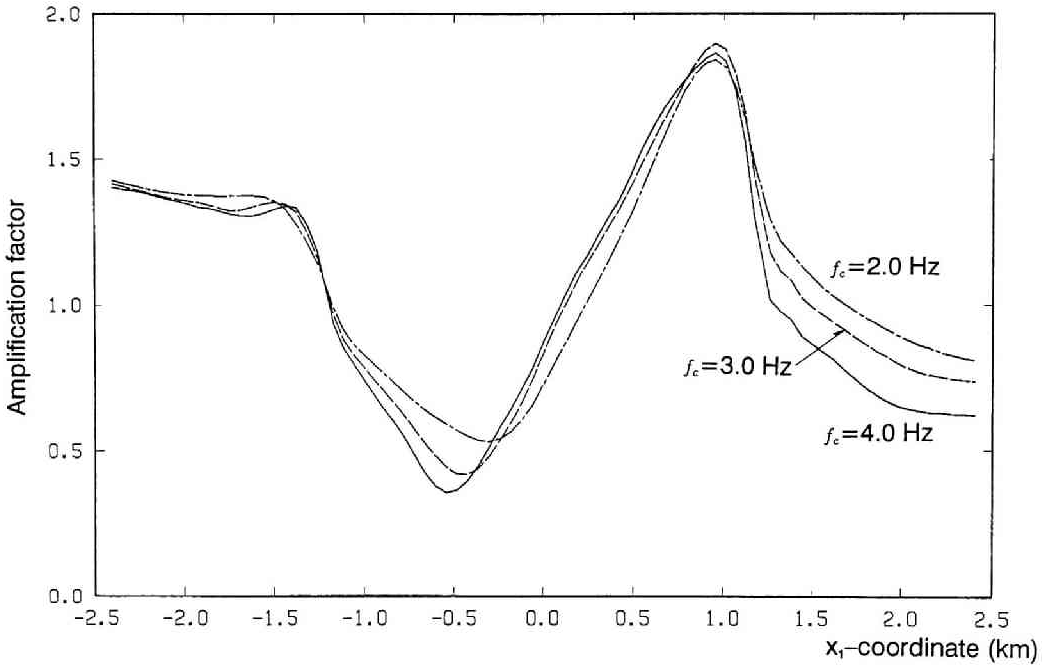

Figure 4.15: Maximum amplitude distribution along the surface of the hill and the surrounding soil for a horizontal line force with the characteristic frequencies f_c of 2 Hz, 3 Hz, and 4 Hz. Amplitude is normalized to that of a half-space at x_1=0.

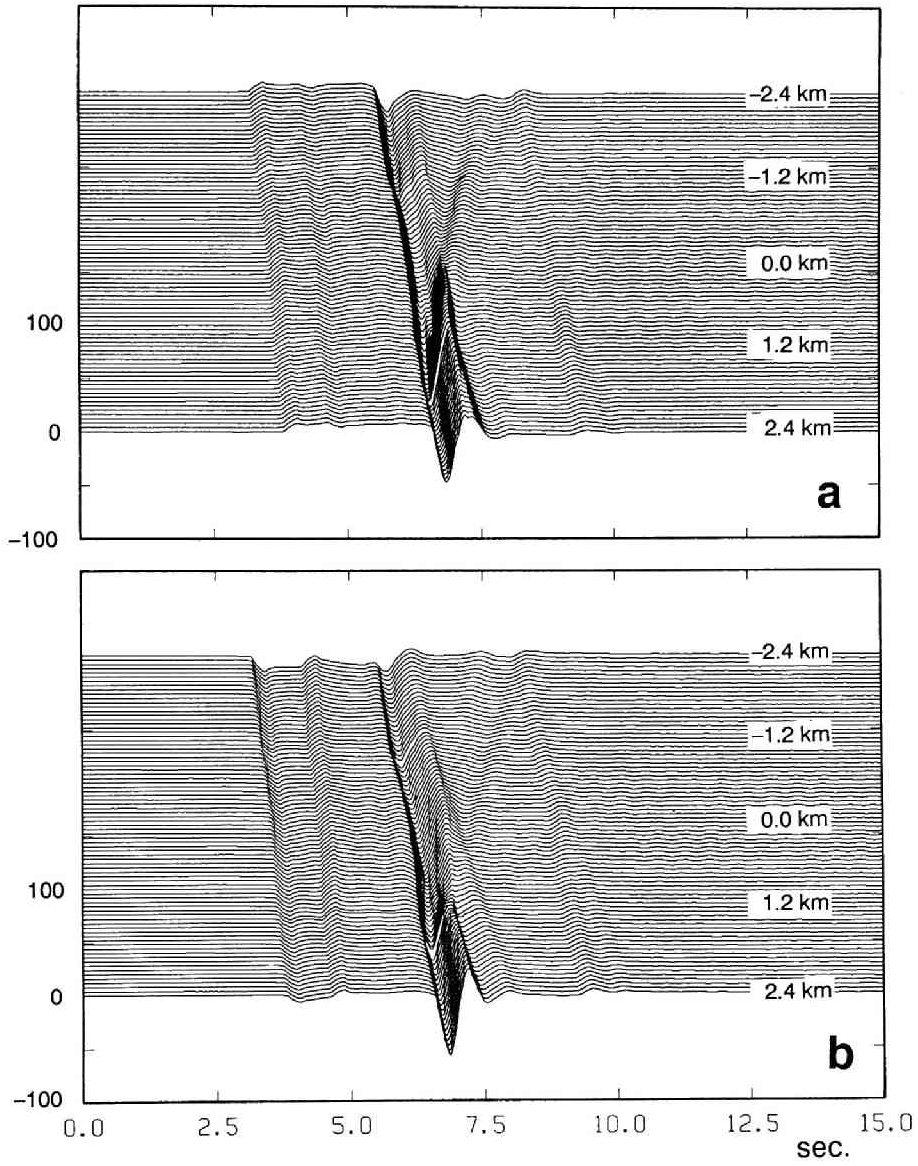

Figure 4.16: Synthetic velocity seismograms along the surface of the hill and the surrounding soil for the Haskell-type fault model with a uniform slip distribution. Amplitude is not normalized (cm/sec). The other conditions are the same as Figure 4.12. The radiation pattern and the directivity effect are recognized when we compare the uppermost and lowermost seismograms.

Note that the maximum amplitude is larger and pulse width is smaller in the lowermost seismogram than in the uppermost one because of the directivity effect. At the hilltop the S-wave stopping phase from the topmost fault tip arrives only 0.66 sec after the arrival of the starting phase from the hypocenter so that all the S-wave energy from the upper segment is concentrated within this short duration. The shape of the intensity VII isoseismal in Figure 4.1 as well as the maximum acceleration contours obtained by Trifunac (1988) seems to reflect this directivity effect in addition to the radiation pattern. The calculated duration of the S wave is about 3.5 sec, about 1.5 sec shorter than the observed (Brady *et al.*, 1988a; Shakal *et al.*, 1988). The difference is expected because both three-dimensional effect of rupture propagation and soil layers are neglected. The effect of the topography is again very similar to the previous cases: the far-side slope of the hill amplifies and the near-side slope deamplifies the surface response.

4.4.4 Bouchon-type fault

Finally a Bouchon-type multiple crack model is considered. Each crack simulates self-similar rupture growth with an elliptical slip distribution along the fault surface (Das and Aki, 1977). The size of each crack is 0.5 km and totally 12 cracks are placed as shown in Figure 4.11. Since the rupture velocity is assumed to be 2 km/sec, each crack completes slip and freezes in 0.25 sec. The total seismic moment is equal to that of the Haskell-type model considered above.

The velocity seismograms in this case are plotted in Figure 4.17. As expected from Bouchon's work (1978), multiple cracks on the upper segment produce major peaks similar to those by the Haskell-type fault since all the observers are located in the direction of rupture propagation. On the other hand, we can see the distinctly separated arrivals from the cracks on the lower segment which propagate away from the observers. These arrivals make the waveform more realistic than that by the Haskell-type fault.

The effect of topography appears again in the same manner as before, but the amplitude fluctuation is larger than that for the Haskell-type fault. The peak amplitude distributions in Figure 4.18 show the difference more clearly. The maximum amplification factor for the Bouchon-type fault reaches 1.8 near the far-side edge.

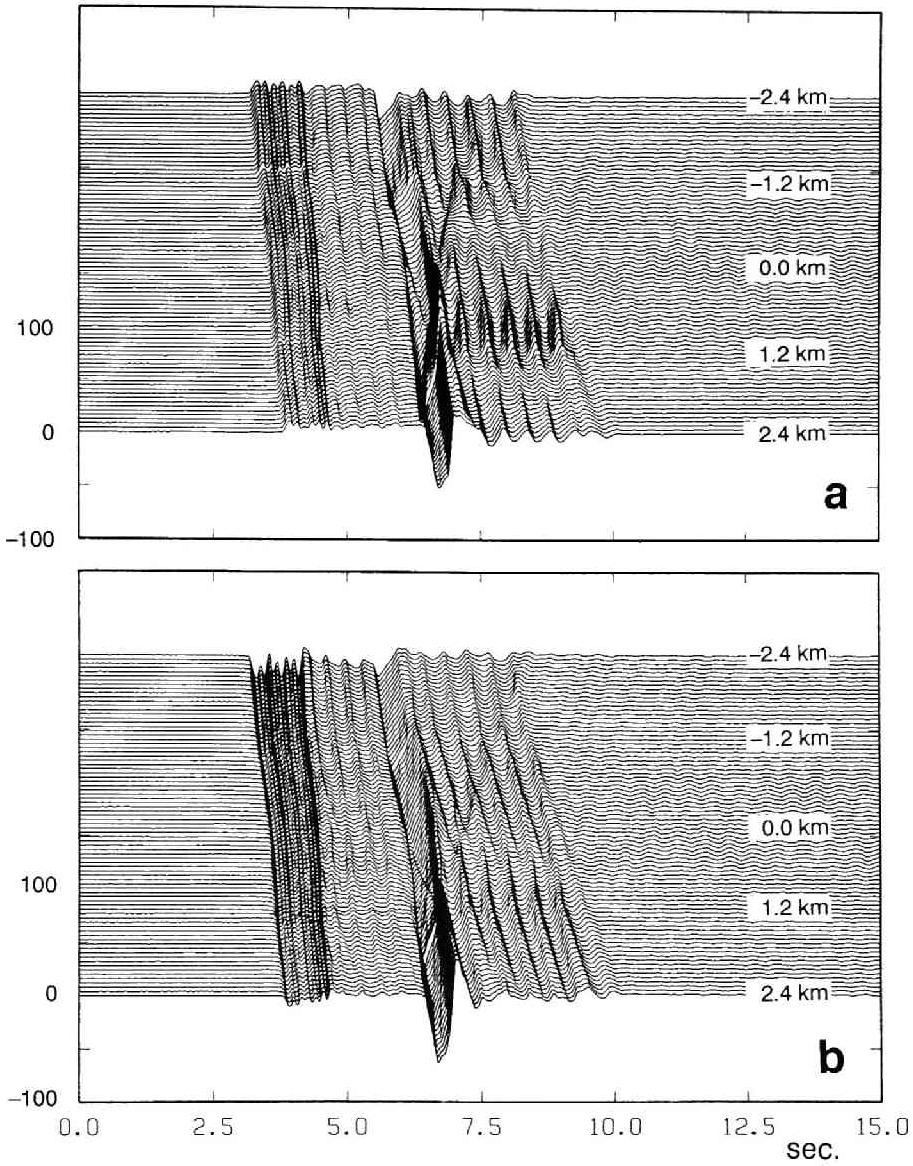

Figure 4.17: Synthetic velocity seismograms along the surface of the hill and the surrounding soil for the Bouchon-type fault model with 12 cracks. Amplitude is not normalized (cm/sec). The other conditions are the same as Figure 4.12. The cracks on the lower segment make periodic fluctuations in the later phase, while cracks on the upper segment give similar peak responses to those by the Haskell-type fault.

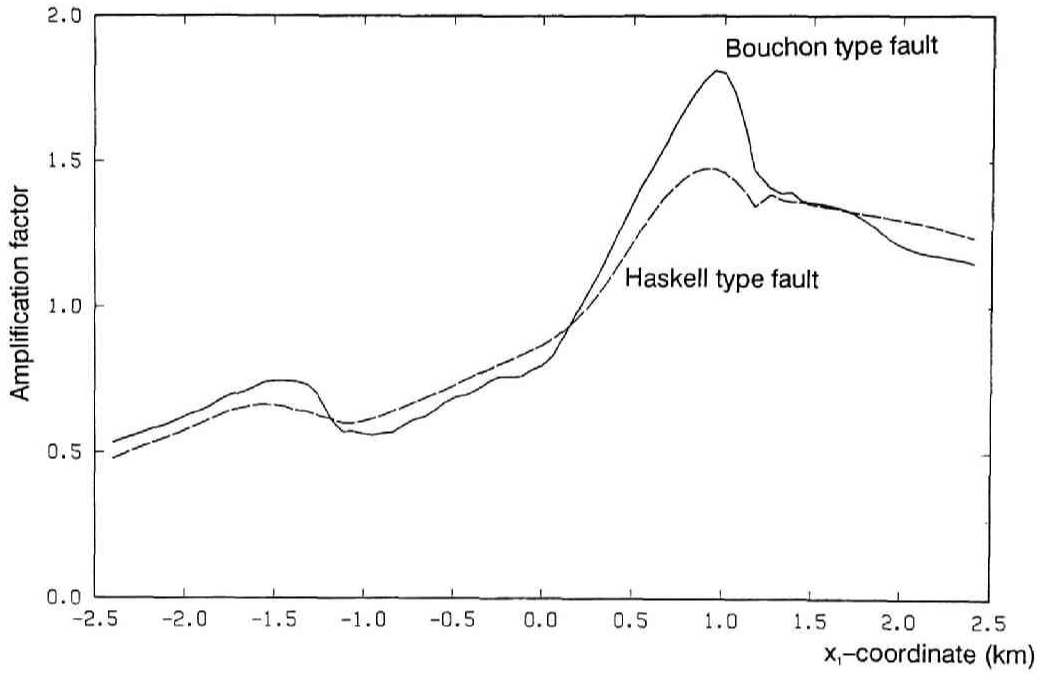

Figure 4.18: Maximum amplitude distributions along the surface of the hill and the surrounding soil for the Haskell-type fault (broken line) and the Bouchon-type fault (solid line). Amplitude is normalized to that of a half-space at x_1=0. The Bouchon-type fault shows stronger effect of the hill than the Haskell-type fault.

4.5 Summary of the results and discussions

The seemingly localized damage pattern due to the Whittier Narrows earthquake of October 1, 1987 showing most severely damaged buildings and water pipes located 8 to 10 km from the epicenter (corresponding to the critical incidence for SV waves) and near topographic irregularities motivated us to conduct a theoretical simulation of ground motion using a 2D model of topographic irregularity for various sources of incident wave.

First we examined the accelerograms obtained at the USGS station (7215 Bright Ave.) nearest to downtown Whittier and conclude that the dominantly east-west motion observed at the station is due to the influence of the building in which accelerograms were recorded. Therefore they are not adequate source of information to describe the ground motion there. We then demonstrate that strong ground motions recorded by 12 stations in the epicentral area show a polarization direction pattern, primarily SV-type, consistent with a simple thrust fault located at the hypocenter.

Then we calculated the response of a two-dimensional hill with the height 0.3 km and the width 2.4 km to i) a plane SV wave with a nearly critical angle of incidence, ii) a horizontal line force, iii) a Haskell-type 2D dislocation source, and iv) a Bouchon-type 2D multiple crack source. The results show that the amplification due to the hill relative to the flat surface is more than 1.5 for all the source models. Since this amplification is nearly independent of the source type and spectrum, we conclude that the combined effect of the topographic irregularity and critically incident SV waves might be responsible for the concentrated damage observed during the Whittier Narrows earthquake.

The maximum amplification factor for the Bouchon-type fault reaches 1.8 near the far-side edge. Since the maximum velocity was 14 cm/sec at the Whittier Narrows Dam, Upstream (Brady *et al.*, 1988b), which is located on a relatively flat surface, the maximum velocity in downtown Whittier might have reached 25 cm/sec. Since the maximum amplification factor in the acceleration response also reaches 1.8 and the acceleration at the Whittier Narrows Dam was 0.30 g, the maximum acceleration in downtown Whittier might have reached 0.54 g. These facts suggest

that the damage concentration in downtown Whittier might be caused by the severe ground motion due to a combined effect of the topography, near-critical incidence, and the directivity of the source.

We cannot deny that the damage concentration in downtown Whittier might be caused by other factors such as rupture focusing, a deep basin structure, soft surface layers, or property of the structures there. However, these solutions seem to have their own shortcomings. For example, rupture focusing or the deep basin structure may create the energy concentration comparable to the size of the fault or the deep structure and therefore they are the candidates of the heavy damage area of the order of tens of km^2, which is significantly larger than the heavy damage area in Whittier. In addition, the results by Wald *et al.* (1988) and Vidale (1989) as well as the authors suggest that a relatively simple model can explain the fundamental characteristics of the observed strong motion, such as response spectra, a radiation pattern, or polarization directions.

On the other hand, soft surface layers can create very localized area of strong shaking. In this case, however, we need a relatively thick soft layer since the shear wave velocity of a typical surface layer in the Los Angeles area is not very low. If, for example, the topmost layer had the average shear wave velocity of 350 m/sec, then its thickness should be 36.5 m to have the fundamental S-wave resonant frequency of 2.4 Hz as observed at BRIG (Figure 4.4). Because the damage concentration appeared along the slope of the hill, it is unlikely to have such a thick layer underneath.

Another possible reason for the damage concentration in downtown Whittier is the property of the structures there, such as the age or type of construction. The detailed surveys on the damaged buildings in Whittier and other areas are not yet completed (Leyendecker *et al.*, 1988; Hart *et al.*, 1988). At present we just emphasize that the damaged building and houses in Whittier are of broad types and that the damaged water pipes showed a similar distribution (Figure 4.2).

A major weakness of the hypothesis here is the assumption of a homogeneous half-space. Even at the hard rock site there exist a layered structure underneath. Its vertical velocity gradient might be small at Puente Hills so that it could not be significant to the effect of the topography. However, it will make the distance larger

from the epicenter to the position at which SV wave is critically incident. Since the effect of small deviation of the incident angle from the critical one have not clarified yet, it should be studied more rigorously in the near future.

Chapter 5

Application to the Mexico Earthquake of 1985

5.1 Description of the problem

The effects of soft surface layers on strong ground motions have been recognized in Japan from as early as the 1930's (Sezawa, 1930; Ishimoto, 1932). Since then they have been studied by many researchers and their importance on the seismic hazard reduction has been demonstrated. An extensive recent review on the effects of surface geology can be found in Aki (1988).

The attempts to correlate the distribution of damage caused by the strong ground motion to some properties of soil such as geologic age, shear wave velocity, or predominant period have been made after many damaging earthquakes (e.g., Zeevaert, 1964; Idriss and Seed, 1968; Seed *et al.*, 1972; Tezcan *et al.*, 1977; Kitagawa and Matsushima, 1982). In these studies it is implicitly assumed that the local structure affecting the ground motion is laterally homogeneous. Actual soft surface layers, however, are not infinitely flat but laterally confined often in the form of a sediment-filled valley or basin. This finiteness of surface layers creates another type of wave, that is, the surface wave which propagates horizontally inside the basin. It sometimes induces a very complicated damage pattern and makes it difficult to correlate the damage pattern simply to any particular soil property. For example, Poceski (1969) attributes the damage concentration caused by the Skopje, Yugoslavia earthquake of 1963 to the lateral heterogeneity of the surface layer. During the Miyagiken-Oki, Japan earthquake of 1978 the damage was mainly concentrated in the transition zone from the mountain area to the alluvial valley (Kubo and Isoyama, 1980).

The destructive Michoacan, Mexico earthquake of 1985 seems to be another example in which the lateral finiteness of the surface layers played an important role. Researchers in Mexico knew before the earthquake that the ground motions

in the Mexico City valley would be strongly amplified by its soft lacustrine layers (Rosenblueth *et al.*, 1960; Zeevaert, 1964). In fact, it has been shown that the heavily damaged area correlates with the thickness (Institute de Ingenieria, UNAM, 1985) or the predominant period (Kobayashi *et al.*, 1986) of the soft layers. The accelerograms recorded on the soft soil during the Michoacan earthquake, however, show a feature which is not easily explained by a simple amplification effect. That feature is the unusually long duration of ground motion in which the later part has a comparable amplitude to the earlier, major part (Quaas *et al.*, 1985; Anderson *et al.*, 1986).

Although it is possible to simulate the response spectra of the observed records by assuming one-dimensional shear wave propagation as done by Romo and Seed (1986), Seed *et al.* (1988), and Romo *et al.* (1988), it is difficult to simulate their time-domain characteristics by a one-dimensional model as Kawase (1987) and Sánchez-Sesma *et al.* (1988) have shown by using the observed record on a hard rock as an input motion. In other words, a large impedance contrast between the soft layer and the bedrock gives a large time-domain amplitude, but not a long duration. Therefore a simple one-dimensional model will fail to generate a prominent later part of the time history recorded in the lake-bed zone. An example of such a failure will be shown in the next section, together with a supporting evidence from Singh *et al.* (1988).

The purpose of this chapter is to study the responses of a soft basin subject to various types of incident waves in the time domain, through which we can examine the possible cause of the long duration observed in Mexico City. Since Kawase (1987) and Bard *et al.* (1988) have already shown that even a strong irregularity of a soft, shallow surface layer contributes little to the prolongation of the response, it is appropriate to start with a deep basin structure whose size is relatively large. Although geotechnical investigations have been in progress after the Michoacan, Mexico earthquake of 1985 (Ovando-Shelley *et al.*, 1988; Romo *et al.*, 1988; Jaime and Romo, 1988), structures and properties of the soil deposits in and around the Mexico City valley, especially those below the soft surface layers, remain uncertain. Thus, the approach here cannot be truly quantitative, but only tries to find a plausible explanation of the observed long duration using possible model structures.

To calculate the response of such a deep basin structure, various methods have been proposed. Among others, a very thorough study of the dependence of vibration mode on structural parameters of the basin and incident wave types was made by Bard and Bouchon (1980a, 1980b) who calculated time-domain responses by the Aki-Larner method (Aki and Larner, 1970) with the Fast Fourier Transform (FFT). Although the Aki-Larner method is efficient in computation, it is limited by two shortcomings: it cannot treat very steep boundaries, and it cannot solve problems of surface wave incidence. The DWBEM overcomes these difficulties (Kawase, 1988). A modified version of the DWBEM is used in this chapter because additional speed in computation is necessary to calculate the response of soft basins (Kawase and Aki, 1989b).

5.2 Observation and 1D analysis

The Mexico City valley is a large sedimentary basin covered by soft lacustrine deposits. Figure 5.1 displays the zoning of the uppermost stratigraphy of the Mexico City valley. The lake-bed zone consists of very soft clays and sand lenses, while the hill zone consists of alluvial and glacial deposits and lava flows. The accelerometer stations SCT and CDAO are located in the lake-bed zone and TACY in the hill zone as shown in Figure 5.1.

The depth profiles of the shear wave velocity, which play a dominant role on the amplification characteristics of the surface layers, have been investigated before and after the Michoacan, Mexico earthquake (Muris, 1978; Sánchez-Sesma *et al.*, 1988; Jaime and Romo, 1988). Profiles for the stations SCT and CDAO interpreted by Seed *et al.* (1988) from the direct borehole measurements are shown in Figure 5.2**a** together with the calculated amplification characteristics under one-dimensional S wave excitation. The Fourier spectral ratios of the observed accelerograms at SCT and CDAO with respect to TACY are also shown in the figure. The calculated amplification factors are considerably smaller and the predominant periods are shorter than those observed. To improve the fit Seed *et al.* (1988) proposed another soil profile for each site based on the predominant period of the earthquake records. The amplification characteristics of these soil models are shown in Figure 5.2**b**. Al-

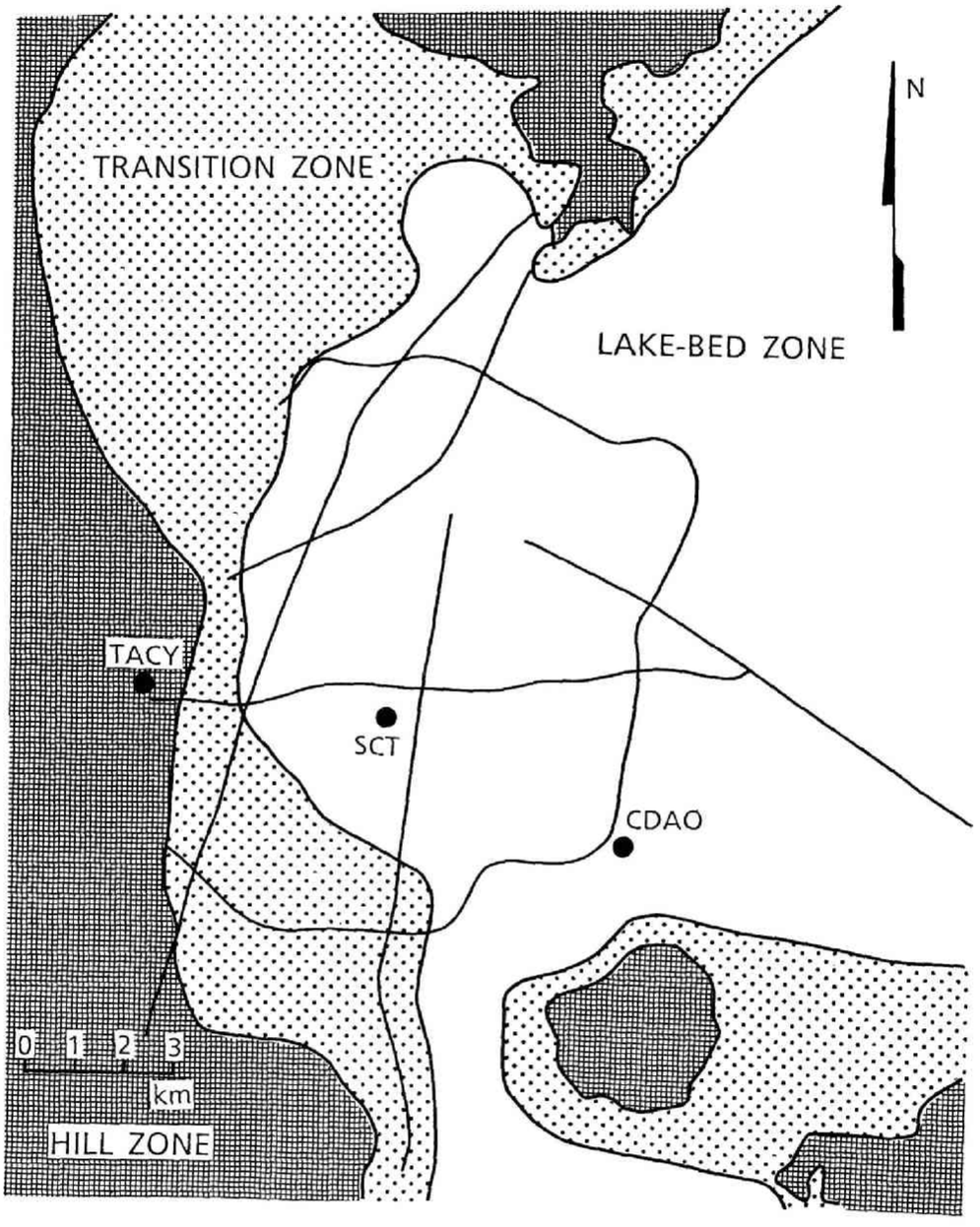

Figure 5.1: Location map of the valley of Mexico City showing hill, transition, and lake-bed zones. Accelerometer stations TACY (Tacubaya), SCT (Secretaria de Comunicaciones y Transportes), and CDAO (Central de Abastos, Office) are also shown.

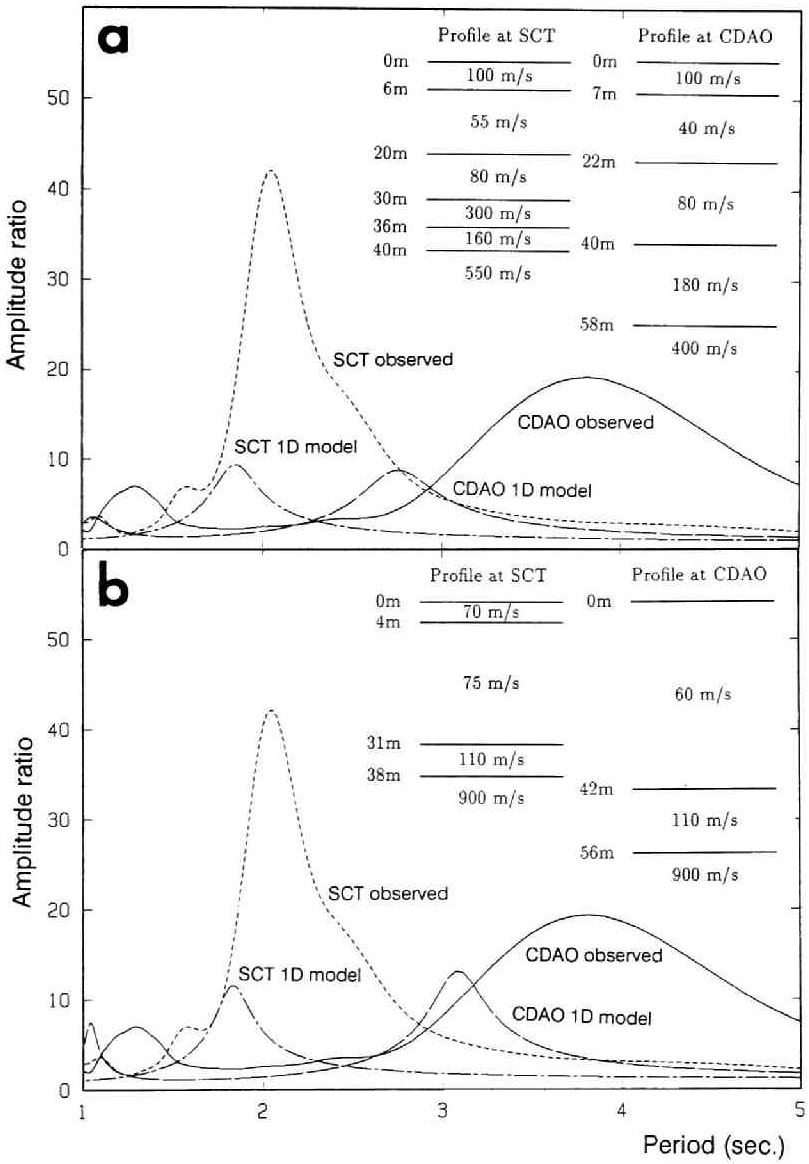

Figure 5.2: Amplification factors calculated by one-dimensional models of soft surface layers. Shear wave velocity profiles at SCT and CDAO, interpreted from direct borehole measurements (**a**), and proposed based on the observed predominant periods (**b**), by Seed *et al.* (1988) are shown inside the corresponding figures. The spectral ratios of accelerograms at SCT and CDAO with respect to TACY averaged for two horizontal components are also shown.

though the discrepancy is slightly reduced, the calculated amplification factors are still much smaller than the observed spectral ratios. It should be mentioned that the discrepancy in the response spectra between the recorded and computed motions shown by Seed *et al.* (1988) is much smaller than the discrepancy in the spectral ratio shown here because damped response spectra saturate easily and so they cannot reflect the difference in duration (Lin, 1976; Sánchez-Sesma *et al.*, 1988). Therefore it is dangerous to discuss the characteristics of the observed records or calculated synthetics just by response spectra.

The data obtained by Singh *et al.* (1988) from the extensive network of strong motion stations scattered over Mexico City show that this spectral deficiency for a one-dimensional model is common to most sites. Figure 5.3 reproduces the peak spectral ratios obtained by Singh *et al.* (1988) from observed accelerograms at 30 stations in the lake-bed zone relative to the station CU in the hill zone. It is found that the average spectral ratio for the period range of 3 to 5 seconds is about 60% larger than that for 1 to 3 seconds as shown by the horizontal lines. Solid curves indicate the amplification for seven subsurface structures identical to the CDAO structure shown in Figure 5.2**b** except that the total thickness of the two layers is chosen as 26m, 36m, 46m, 56m, 66m, 76m, and 86m with the same proportion of the two layer thicknesses. As is well known, one-dimensional models with the same impedance contrast give the same peak amplification irrespective of the layer thickness. Note that the calculated peak amplification nearly corresponds to the minimum level of the observed ratios. The comparison between observation and one-dimensional theory reveals that the additional amplification by 30% to 100% is necessary on the average. If the observed larger amplification is due to the longer duration as observed at SCT or CDAO, the dependence of the peak value on the period suggests that the source structure of the longer duration should have the peak (resonant) period around 3.5 seconds.

In order to further convince the reader about the deficiency of the one-dimensional model a time-domain comparison is shown in Figure 5.4. The top and bottom traces are the observed accelerograms at SCT and CDAO, respectively. The seven time-histories between them are the accelerograms calculated by using the one-dimensional theoretical responses shown in Figure 5.3 and the observed ac-

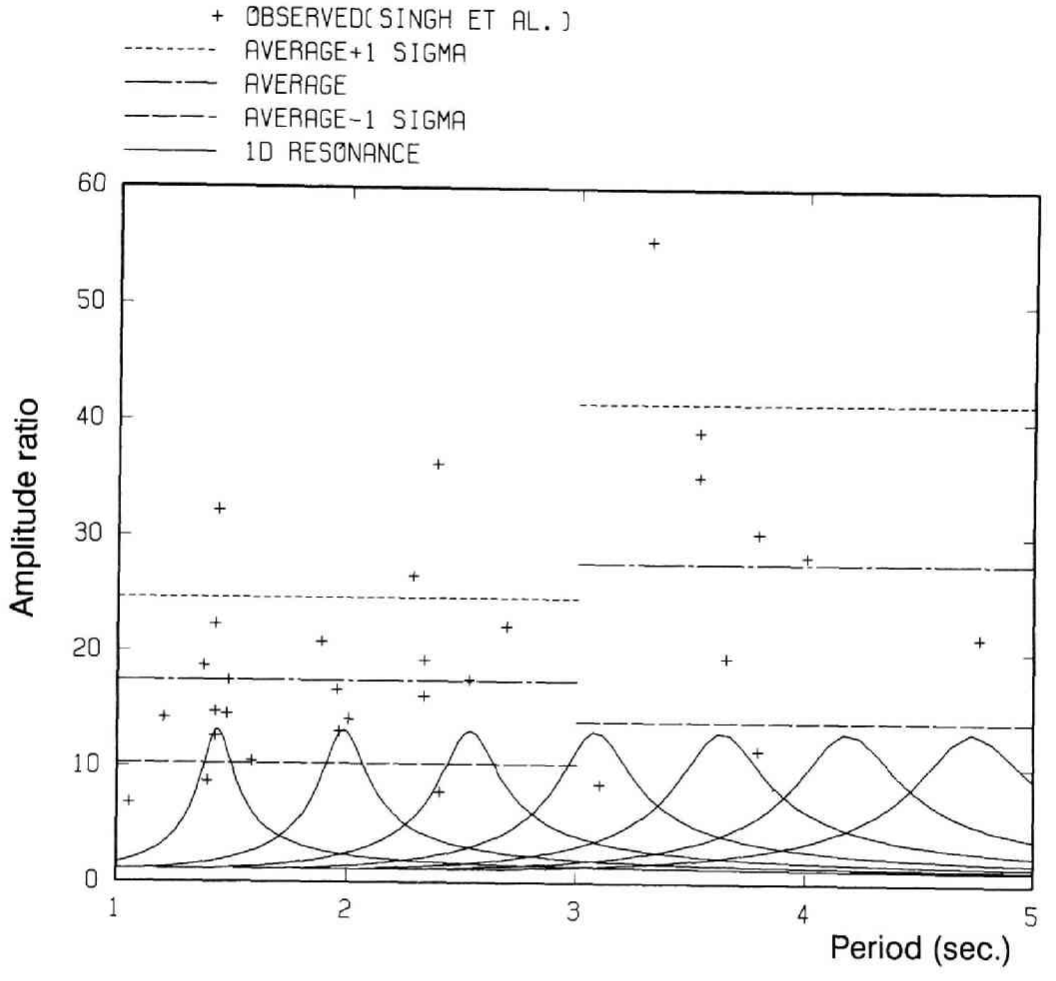

Figure 5.3: Predominant period versus relative amplification compiled from Table 2 in Singh *et al.* (1988). Symbols + denote the observed values at 30 different points scattered inside the valley of Mexico City. Three horizontal lines show the average and the average ± one standard deviation for two period ranges: from 1 to 3 seconds and from 3 to 5 seconds. The solid curves represent the amplification characteristics of the fundamental mode of S wave excitation calculated by seven one-dimensional structures which are identical to the CDAO structure in Figure 5.2**b**, except that the total thickness of the two layers is modified to 26m, 36m, 46m, 56m, 66m, 76m, and 86m.

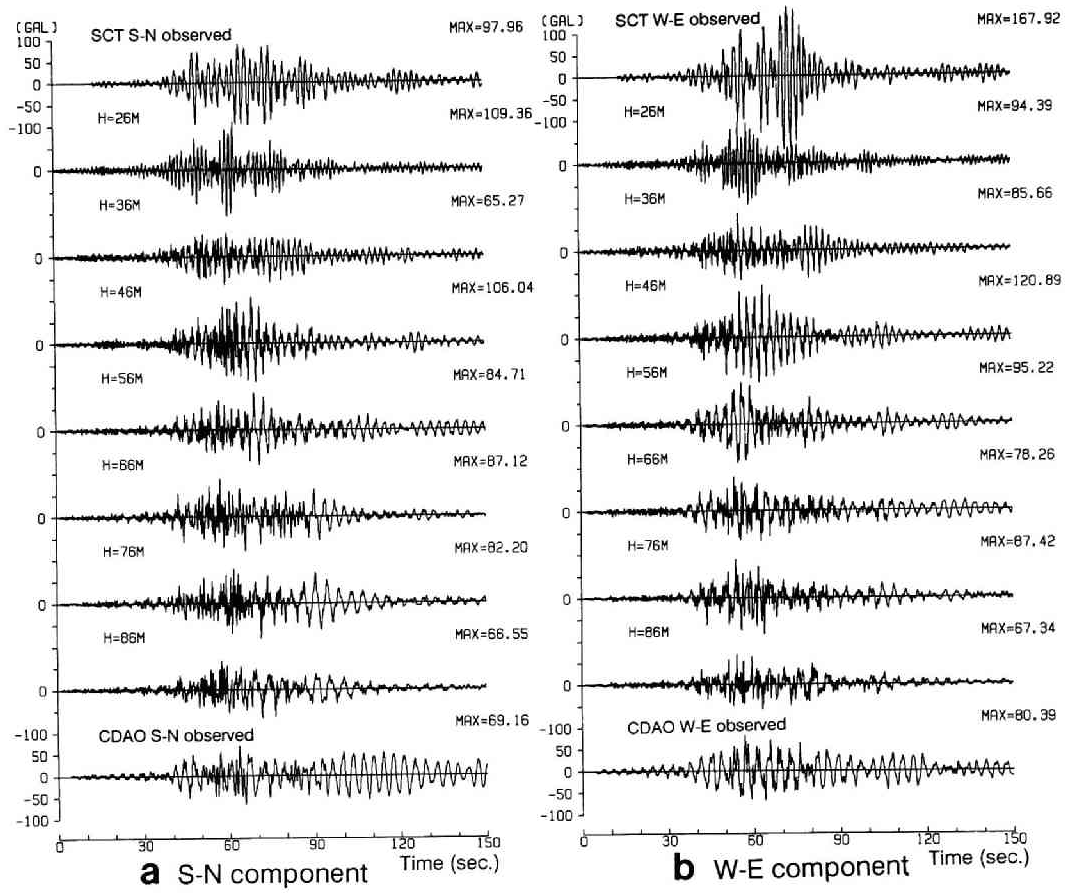

Figure 5.4: Calculated accelerograms by one-dimensional models whose amplification characteristics are shown in Figure 5.3. The accelerogram at TACY is used as an input motion at the bedrock. The observed accelerograms at SCT and CDAO are also plotted at the top and the bottom of the figure. The left and right columns correspond to SN and WE components, respectively.

celerogram at TACY as an input. Note that all of them show deficiency in later phases after 70 to 75 seconds as compared to the observed records at SCT and CDAO.

From these results it is concluded that the observed large spectral ratios must be due to the long duration, which one-dimensional models fail to simulate. In the following sections the effect of two-dimensional structures is studied as a possible cause of the long duration by using the modified DWBEM.

5.3 Method of analysis

Since the DWBEM has been fully described in Chapter 2, only the modified part for the analysis of a basin is presented. Most time-consuming work in the DWBEM is to calculate the functions $G_{ji}(\mathbf{x};\mathbf{x}^*)$ and $H_{ji}(\mathbf{x},\mathbf{n};\mathbf{x}^*)$, which are expressed as infinite sums over the discrete wavenumbers in case of an in-plane problem. The computation becomes longer if the size of a basin is larger and the calculated duration is longer. The worst convergence is achieved when both a source and a receiver are near the free-surface. To improve the efficiency of this computation, the author uses a hybrid scheme, that is, evaluation partially by the exact formula and partially by the discrete-wavenumber summation.

The Green function for a full-space (a homogeneous unbounded medium), ${G_{ji}}^F(\mathbf{x};\mathbf{x}^*)$, can be expressed by the following formula

$$
\begin{aligned}
{G_{ji}}^F(\mathbf{x};\mathbf{x}^*) &= \frac{i}{4\mu}\left[-\delta_{ji}{H_0}^{(2)}(k_\beta r)+\frac{\delta_{ji}}{k_\beta r}\left\{{H_1}^{(2)}(k_\beta r)-\frac{\beta}{\alpha}{H_1}^{(2)}(k_\alpha r)\right\}\right. \\
&\qquad \left.-\frac{\partial r}{\partial x_j}\frac{\partial r}{\partial x_i}\left\{{H_2}^{(2)}(k_\beta r)-\frac{\beta^2}{\alpha^2}{H_2}^{(2)}(k_\alpha r)\right\}\right] \qquad (5.1)
\end{aligned}
$$

for the in-plane problem ($i=1,3\,;\ j=1,3$), where μ is a shear modulus, α and β are P and S wave velocities, $H_m^{(2)}(\cdot)$ is the Hankel functions of the second kind and mth order, and

$$
\begin{aligned}
k_\alpha &= \omega/\alpha, \qquad (5.2)\\
k_\beta &= \omega/\beta, \qquad (5.3)\\
r &= \sqrt{(x_1-x_1^*)^2+(x_3-x_3^*)^2}\,. \qquad (5.4)
\end{aligned}
$$

Since the in-plane Green function for a half-space consists of the Green function for a full-space and the surface term (Chapter 2), we can replace the former with the expression of equation (5.1). We can also separate the surface term into two parts, one of which corresponds to the image-source solution. We replace this image-source part with the same exact formula to get the following advantages. First, the remaining discrete-wavenumber term becomes simpler, which makes the calculation for each wavenumber faster. Second, while the original surface term will be singular if $x_1 = x_1^*$ and $x_3 = x_3^* = 0$, the remaining discrete-wavenumber term is not singular anymore. This makes the wavenumber summation converge faster. As mentioned in Chapter 2, the anti-plane Green function for a half-space needs no discrete-wavenumber term.

The final expression of the Green function for a half-space is

$$
\begin{aligned}
G_{11}^{H}(\mathbf{x};\mathbf{x}^*) &= G_{11}^{F}(\mathbf{x};\mathbf{x}^*) + G_{11}^{F}(\mathbf{x};\tilde{\mathbf{x}}^*) \\
&+ \frac{i}{2Lk_\beta{}^2\mu} \sum_{n=-\infty}^{\infty} \frac{1}{\Delta(k_n)} \\
&\quad \left[\frac{2k_n{}^2(2k_n{}^2 - k_\beta{}^2)^2}{\nu_n} E^{H}_{\nu_n\nu_n} + 4k_n{}^2\gamma_n(2k_n{}^2 - k_\beta{}^2) E^{H}_{\gamma_n\nu_n} \right. \\
&\quad \left. + 4k_n{}^2\gamma_n(2k_n{}^2 - k_\beta{}^2) E^{H}_{\nu_n\gamma_n} + 8k_n{}^2\nu_n\gamma_n{}^2 E^{H}_{\gamma_n\gamma_n} \right] E_{k_n} \qquad (5.5) \\
G_{31}^{H}(\mathbf{x};\mathbf{x}^*) &= G_{31}^{F}(\mathbf{x};\mathbf{x}^*) + G_{31}^{F}(\mathbf{x};\tilde{\mathbf{x}}^*) \\
&+ \frac{i}{2Lk_\beta{}^2\mu} \sum_{n=-\infty}^{\infty} \frac{1}{\Delta(k_n)} \\
&\quad \left[2k_n(2k_n{}^2 - k_\beta{}^2)^2 E^{H}_{\nu_n\nu_n} - 4k_n{}^3(2k_n{}^2 - k_\beta{}^2) E^{H}_{\gamma_n\nu_n} \right. \\
&\quad \left. + 4k_n\nu_n\gamma_n(2k_n{}^2 - k_\beta{}^2) E^{H}_{\nu_n\gamma_n} - 8k_n{}^3\nu_n\gamma_n E^{H}_{\gamma_n\gamma_n} \right] E_{k_n} \qquad (5.6) \\
G_{13}^{H}(\mathbf{x};\mathbf{x}^*) &= G_{13}^{F}(\mathbf{x};\mathbf{x}^*) + G_{13}^{F}(\mathbf{x};\tilde{\mathbf{x}}^*) \\
&+ \frac{i}{2Lk_\beta{}^2\mu} \sum_{n=-\infty}^{\infty} \frac{1}{\Delta(k_n)} \\
&\quad \left[8k_n{}^3\nu_n\gamma_n E^{H}_{\nu_n\nu_n} - 4k_n\nu_n\gamma_n(2k_n{}^2 - k_\beta{}^2) E^{H}_{\gamma_n\nu_n} \right.
\end{aligned}
$$

$$+4k_n{}^3(2k_n{}^2 - k_\beta{}^2)E^H_{\nu_n\gamma_n} - 2k_n(2k_n{}^2 - k_\beta{}^2)^2 E^H_{\gamma_n\gamma_n}\Big] E_{k_n} \quad (5.7)$$

$$\begin{aligned} G_{33}{}^H(\mathbf{x};\mathbf{x}^*) &= G_{33}{}^F(\mathbf{x};\mathbf{x}^*) + G_{33}{}^F(\mathbf{x};\bar{\mathbf{x}}^*) \\ &+ \frac{i}{2Lk_\beta{}^2\mu}\sum_{n=-\infty}^{\infty}\frac{1}{\Delta(k_n)} \\ &\Big[8k_n{}^2\nu_n{}^2\gamma_n E^H_{\nu_n\nu_n} + 4k_n{}^2\nu_n(2k_n{}^2 - k_\beta{}^2)E^H_{\gamma_n\nu_n} \\ &+4k_n{}^2\nu_n(2k_n{}^2 - k_\beta{}^2)E^H_{\nu_n\gamma_n} + \frac{2k_n{}^2(2k_n{}^2 - k_\beta{}^2)^2}{\gamma_n}E^H_{\gamma_n\gamma_n}\Big] E_{k_n}\,, \end{aligned} \quad (5.8)$$

where,

$$\begin{aligned} \bar{\mathbf{x}}^* &= (x_1{}^*, -x_3{}^*) \\ k_n &= (2\pi/L)n \\ \nu_n &= (k_\alpha{}^2 - k_n{}^2)^{1/2} \qquad Im\ \nu_n < 0 \\ \gamma_n &= (k_\beta{}^2 - k_n{}^2)^{1/2} \qquad Im\ \gamma_n < 0 \\ \Delta(k_n) &= (2k_n{}^2 - k_\beta{}^2)^2 + 4k_n{}^2\nu_n\gamma_n\,. \end{aligned} \quad (5.9)$$

The same abbreviations as in equations (2.24) and (2.34) are used in the above equations.

A disadvantage of this hybrid scheme is that it is no longer possible to evaluate analytically the element integration for the full-space and image-source Green functions. We use the Gauss-Legendre quadrature for these terms. If $\mathbf{x} = \mathbf{x}^*$, the singular integral is evaluated by the method of Banaugh and Goldsmith (1963). The discrete-wavenumber terms are always integrated analytically. The accuracy of this hybrid scheme is successfully tested with the ordinary discrete-wavenumber Green function. In short, this hybrid scheme makes the DWBEM possible to improve its computational efficiency at the expense of its accuracy and stability in high frequency range. This expense is minimal because our main concern here is the source of the observed long duration in the relatively long period range, namely, 2 to 4 seconds.

5.4 A deep basin structure

It seems appropriate to start with a deep basin structure whose size is relatively large, since a soft, shallow surface layer alone could not prolong the input motion so much. First the model of a deep basin structure underneath Mexico City is described, then the responses of the surface of the basin due to incident SH, SV, P, and Rayleigh waves are shown.

5.4.1 A model

Figure 5.5 shows the model configuration for a deep basin structure called type 1. This basin has a trapezoidal shape with 1 km depth and 10 km width at the surface. The slope at the edges is 1:2 so that the transition zone is 2 km long along the surface. This model is similar to the type 2 valley used by Bard and Bouchon (1980a, 1980b), which has cosine-shaped side slopes.

It is known that the maximum depth of the Tertiary sediment in Mexico City may reach 2 km (Muris, 1978). From the seismic exploration survey near the southwest end of Texcoco Lake, major discontinuities in P wave velocity were found at depths of 0.5 km and 1.3 km (Marsal and Graue, 1969). Recently Sánchez-Sesma *et al.* (1988) reported the maximum depth of 700m for the deeper deposit (pre-Chichinautzin basin). Therefore the 1 km depth may be appropriate as a representative value of the deeper Mexico City valley sediment. The width of the basin is somewhat greater than 10 km, but this value is chosen for the computational economy. A more quantitative simulation may be justified when more accurate information of the deeper structure underneath Mexico City becomes available.

It is assumed that the shear wave velocities of the layer β_1 and the half-space β_2 are 1.0 km/sec and 2.5 km/sec, respectively. These values are obtained from the observed P wave velocity data (Marsal and Graue, 1969) assuming Poisson's ratio of 1/3. Although the upper part seems to have a smaller shear wave velocity such as 0.4 km/sec or 0.55 km/sec as shown in Figure 5.2a, it must increase with depth. Therefore 1.0 km/sec is a reasonable estimate for the average shear wave velocity of the layer. No material damping and no density contrast are assumed since these values would be small and have a negligible effect.

Again the time dependence of the input signal is a Ricker wavelet defined as

$$u(t) = (2\pi^2 f_c{}^2 t^2 - 1)\exp(-\pi^2 f_c{}^2 t^2), \tag{5.10}$$

where f_c is the characteristic frequency of a wavelet. The shape and spectra are shown in Figure 3.7. The Ricker wavelet is best suited for our aim because we can examine the wave propagation phenomena easily for different frequency ranges. First the response of a basin is obtained in the frequency domain, then it is transformed into the time domain as a convolution with this Ricker wavelet using the FFT algorithm. The calculated amplitude is normalized to the amplitude of an incident wave, except for Rayleigh wave incidence in which it is normalized to the amplitude of the horizontal free-field motion. Most of the results are for the characteristic frequency f_c of 0.25 Hz (4 seconds in period), which corresponds to the fundamental resonant frequency of the plane layer for normally incident S waves. This also corresponds to the predominant frequency observed at CDAO (0.25–0.28 Hz). Several examples for higher or lower characteristic frequency input are also shown for comparison. The frequencies selected in the DWBEM calculation are equally distributed from 0.0 Hz up to 2.0 Hz with 0.025 Hz interval. The periodicity length L is set to 100 km in all in-plane problems.

5.4.2 SH wave incidence

The time domain responses of a soft basin for SH wave incidence were studied thoroughly by Bard and Bouchon (1980a). Our results are simpler mainly due to the simpler shape and the lower impedance contrast of our model as compared to theirs.

The responses (anti-plane component) at the surface of the type 1 basin by a vertically incident SH wave are plotted in Figure 5.6. The distances from the left edge are shown inside the figure. The characteristic frequency f_c is 0.25 Hz (4 seconds). This figure shows the horizontally propagating waves generated by the edges of the basin, which are the fundamental mode of Love waves as pointed out by Bard and Bouchon (1980a). The amplitude of Love waves is smaller than that of the direct wave. Although these Love waves make the total duration longer, the

time interval between the direct wave arrival and the Love wave arrival is less than 10 seconds near the edges. Each arrival of reflected Love waves is well separated.

Figure 5.7 shows the responses for a Ricker wavelet of f_c=0.5 Hz (2 seconds). Very similar phenomena to that shown in Figure 5.6 can be seen, but the amplitude of the Love wave is larger in this case. For frequencies higher than 0.5 Hz, the maximum amplitude of the Love wave decreases because energy splits into the fundamental mode and the first higher mode, as the dispersion curves in Figure 5.10a suggest.

On the other hand, if f_c is as low as 0.167 Hz (6 seconds), the interaction between incident wave and the valley becomes very weak as shown in Figure 5.8.

From the theoretical point of view it is interesting to see how the shape of the transition zone affects the response. As an extreme example the author calculates the response of a rectangular basin, called here the type 1' basin, whose depth and material properties are the same as the type 1 basin. The width of the basin is set to be 8 km. Since the side slopes are vertical, it is not possible for the Aki-Larner method (Aki and Larner, 1970), the ray method (Hong and Helmberger, 1978; Nowack and Aki, 1984; Moczo *et al.*, 1987), nor the discrete wavenumber boundary integral equation method (Bouchon, 1985; Campillo and Bouchon; 1985) to solve this type of irregularity.

Figure 5.9 shows the response of the type 1' basin by a vertically incident SH wave with f_c=0.25 Hz. The main features are remarkably similar to those for the type 1 basin, and only a slight increase of the Love wave amplitude is observed. This means that diffracted wave generated by the displacement discontinuity at the vertical boundary can be transformed into Love waves efficiently. At the same time it suggests that ray approaches may be valid only for basins with smooth and slowly-varying boundaries where strong diffraction never happens.

The reflection coefficient of Love wave at the vertical boundary is larger than that at the slant boundary, which is quite natural. As a result, the type 1' basin can sustain Love wave amplitude longer than the type 1 basin.

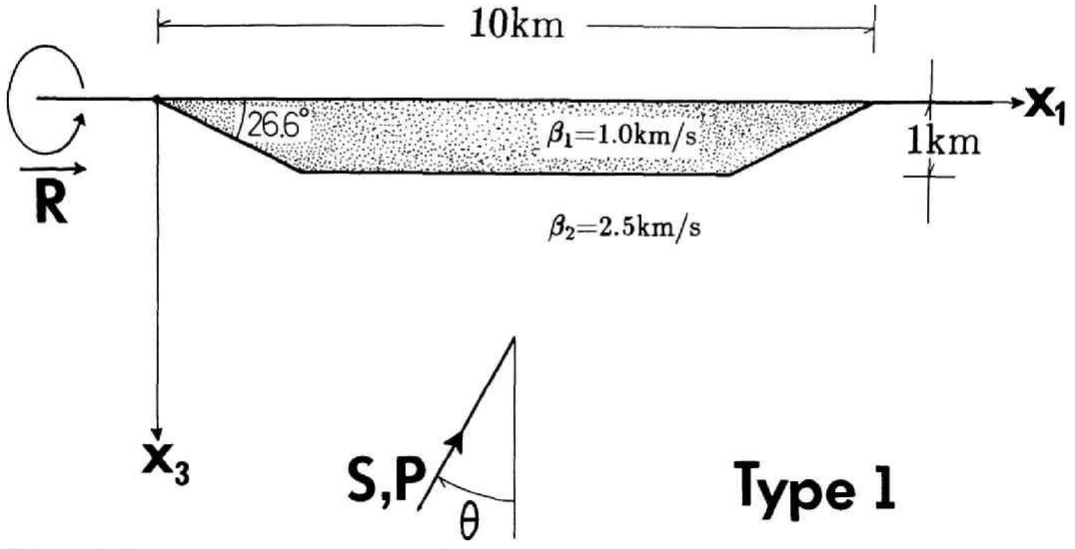

Figure 5.5: A deep basin model used in the analysis. This type 1 basin has a trapezoidal shape with 10 km width and 1 km depth. The shear wave velocities for a basin and a half-space are 1.0 km/sec and 2.5 km/sec, respectively.

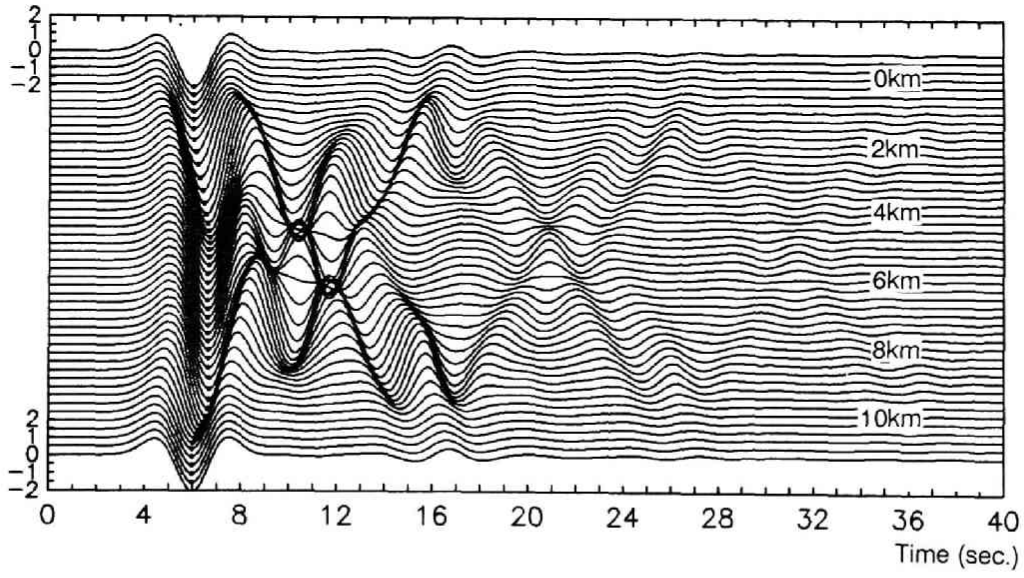

Figure 5.6: Time histories of the responses (anti-plane component) along the surface of the type 1 basin for a vertically incident SH wave. The characteristic frequency of the Ricker wavelet is 0.25 Hz (4 seconds). The distances from the left-side edge are shown inside the figure. The separation distance between two successive traces is 0.25 km. The amplitude is normalized to that of the incident wave.

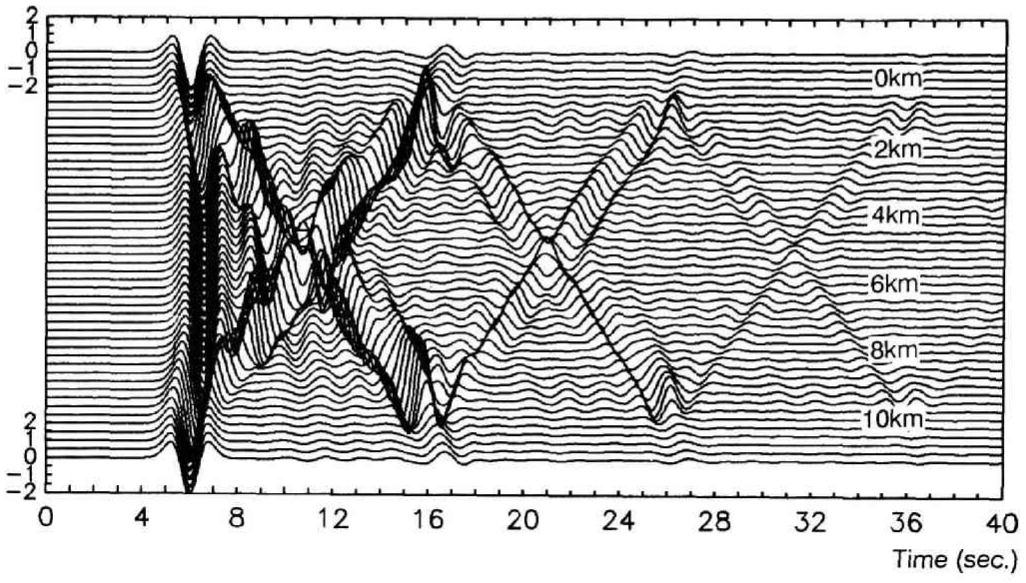

Figure 5.7: The responses of the type 1 basin for a Ricker wavelet of 0.5 Hz (2 seconds). The other conditions are the same as in Figure 5.6. The amplitude of the Love wave near the edges is larger than that for f_c=0.25 Hz.

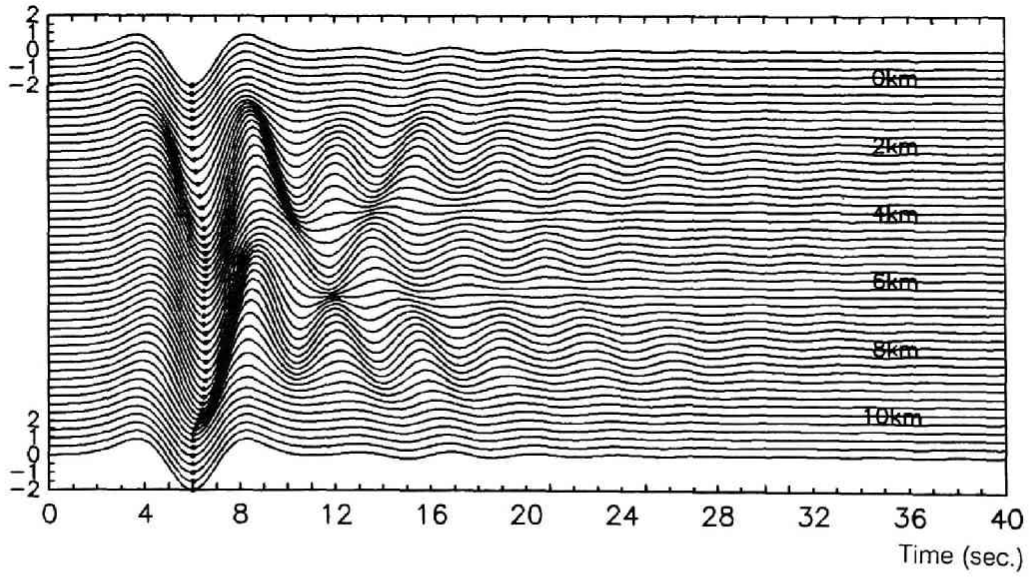

Figure 5.8: The responses of the type 1 basin for a Ricker wavelet of 0.167 Hz (6 seconds). The other conditions are the same as in Figure 5.6.

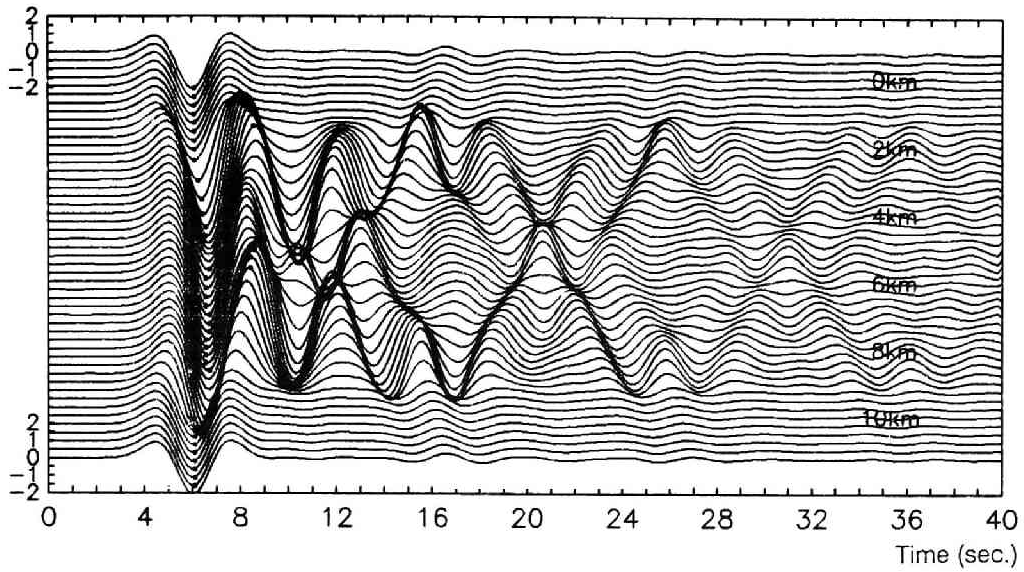

Figure 5.9: The responses of the type 1' basin for a vertically incident SH wave. The other conditions are the same as in Figure 5.6.

5.4.3 SV wave incidence

Now let us consider the cases of incident plane SV waves. Both horizontal (in-plane) component and vertical component are plotted in the same way as in Figure 5.6.

Figure 5.11 shows the responses of the type 1 basin to a vertically incident SV wave with f_c=0.25 Hz (4 seconds). The X-shaped pattern of the surface wave arrivals seen in Figure 5.6 is not present in this figure. Instead, successive wave trains appear in the transition zone (horizontal component) and in the flat part (vertical component). This difference between SH and SV wave incidence is mainly due to the fact that the phase and group velocities of the fundamental mode of Rayleigh waves are considerably higher than those of Love waves in the frequency concerned, as shown in Figure 5.10. The Rayleigh wave generated at the edge needs only 5 seconds to reach the opposite-side edge. So even two folds of back-and-forth propagation inside the basin create only 20 seconds of coda, which is significantly shorter than the observed duration at CDAO shown in Figure 5.4.

Higher frequency input (f_c=0.5 Hz) yields the response shown in Figure 5.12. Unlike the SH wave case in Figure 5.7, two distinctive Rayleigh waves can be seen.

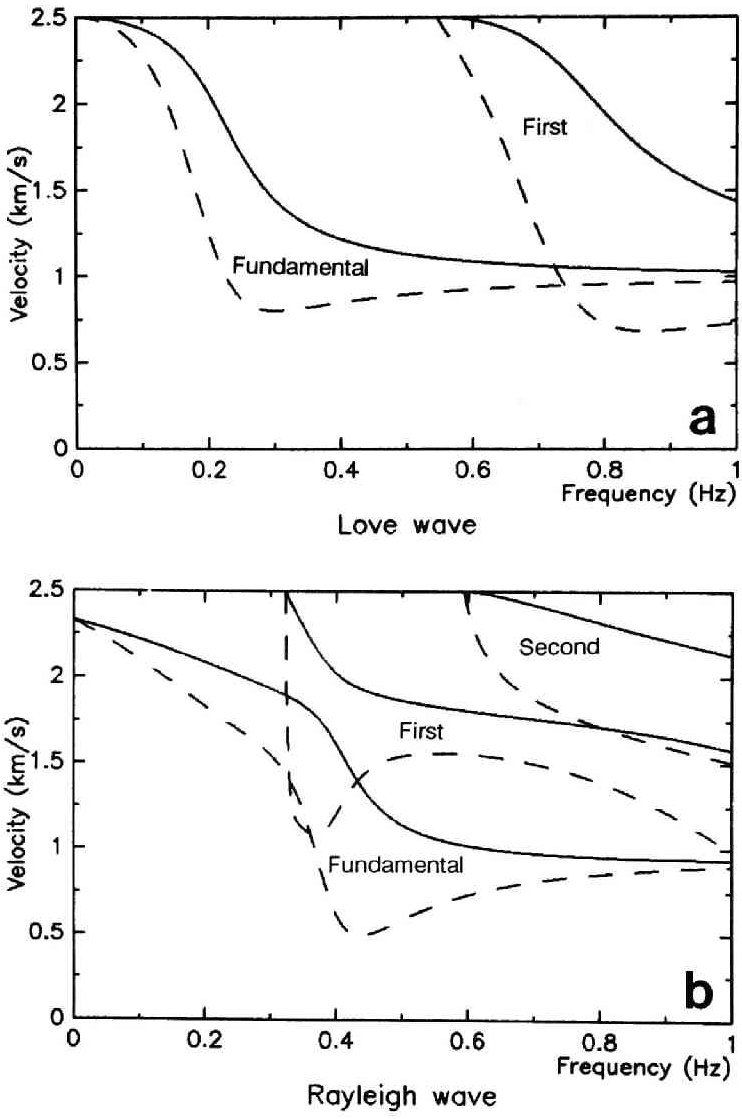

Figure 5.10: Dispersion curves of Love wave (a) and Rayleigh wave (b) for a laterally homogeneous layer overlying a half-space whose material properties correspond to those of a deep basin in Figure 5.5. Solid and broken lines represent the phase and group velocities of the fundamental and several higher modes.

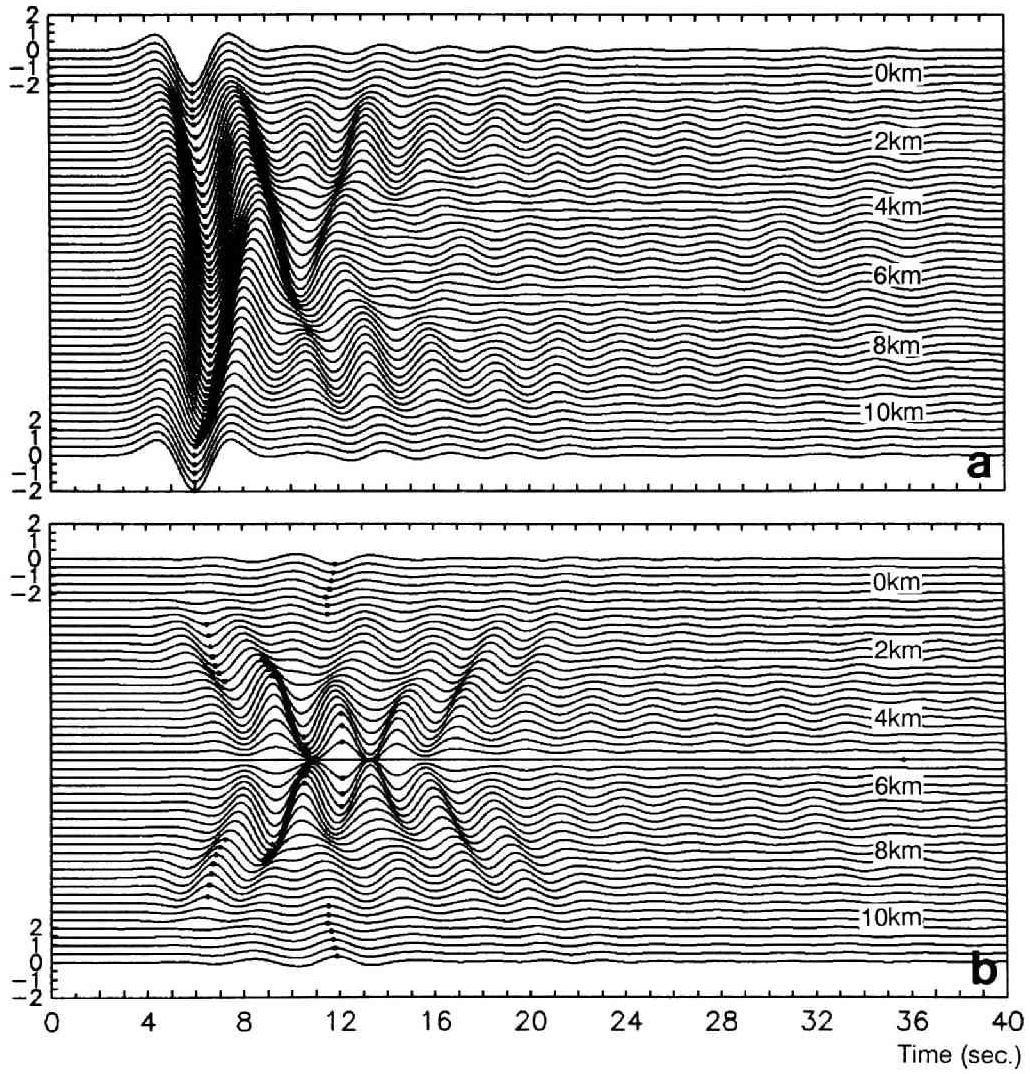

Figure 5.11: Time histories of horizontal (in-plane) component (**a**) and vertical component (**b**) of the type 1 basin for a vertically incident SV wave. The characteristic frequency of the Ricker wavelet is 0.25 Hz (4 seconds). The amplitude of the Rayleigh wave is smaller than that of the Love wave shown in Figure 5.6.

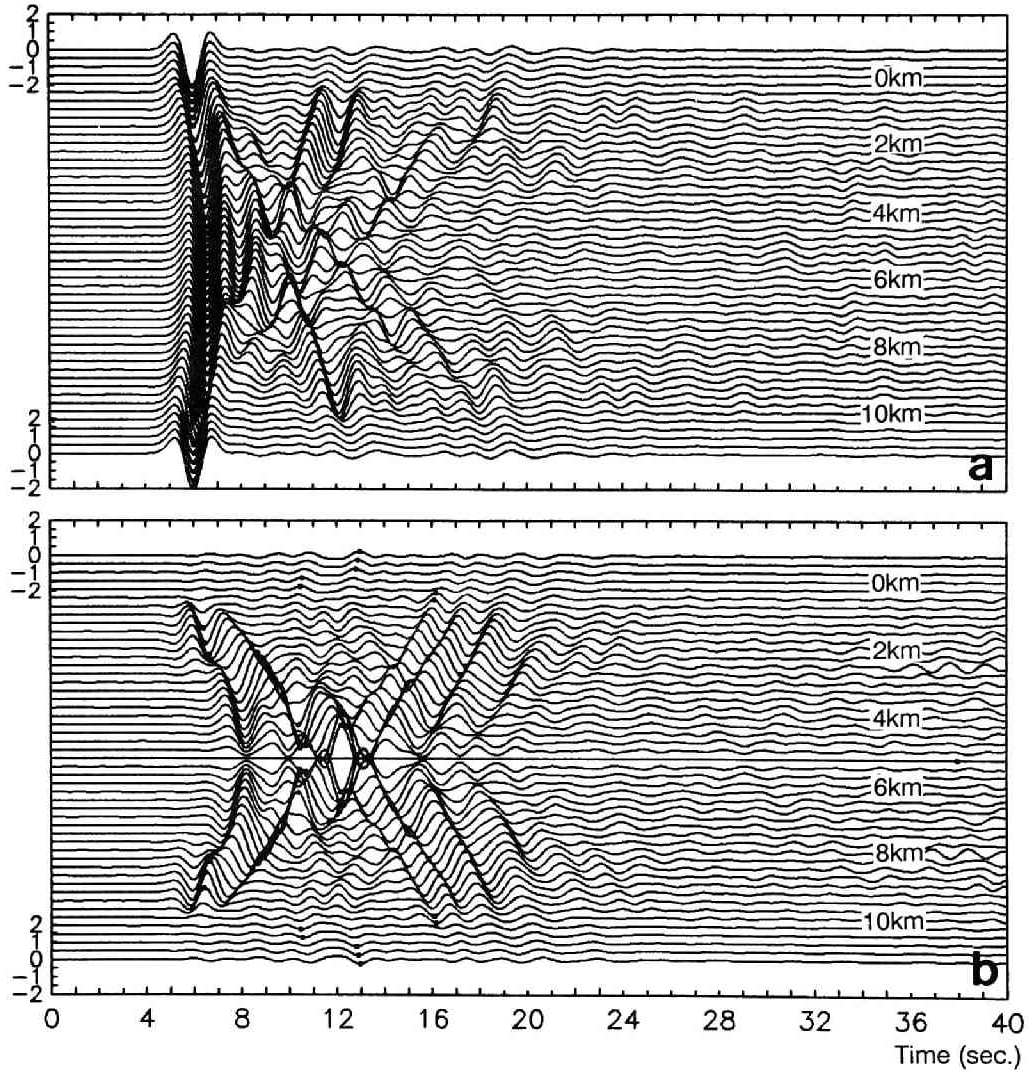

Figure 5.12: The responses of the type 1 basin for a Ricker wavelet of 0.5 Hz (2 seconds). The other conditions are the same as in Figure 5.11. The fundamental and first higher modes of Rayleigh waves are easily distinguishable.

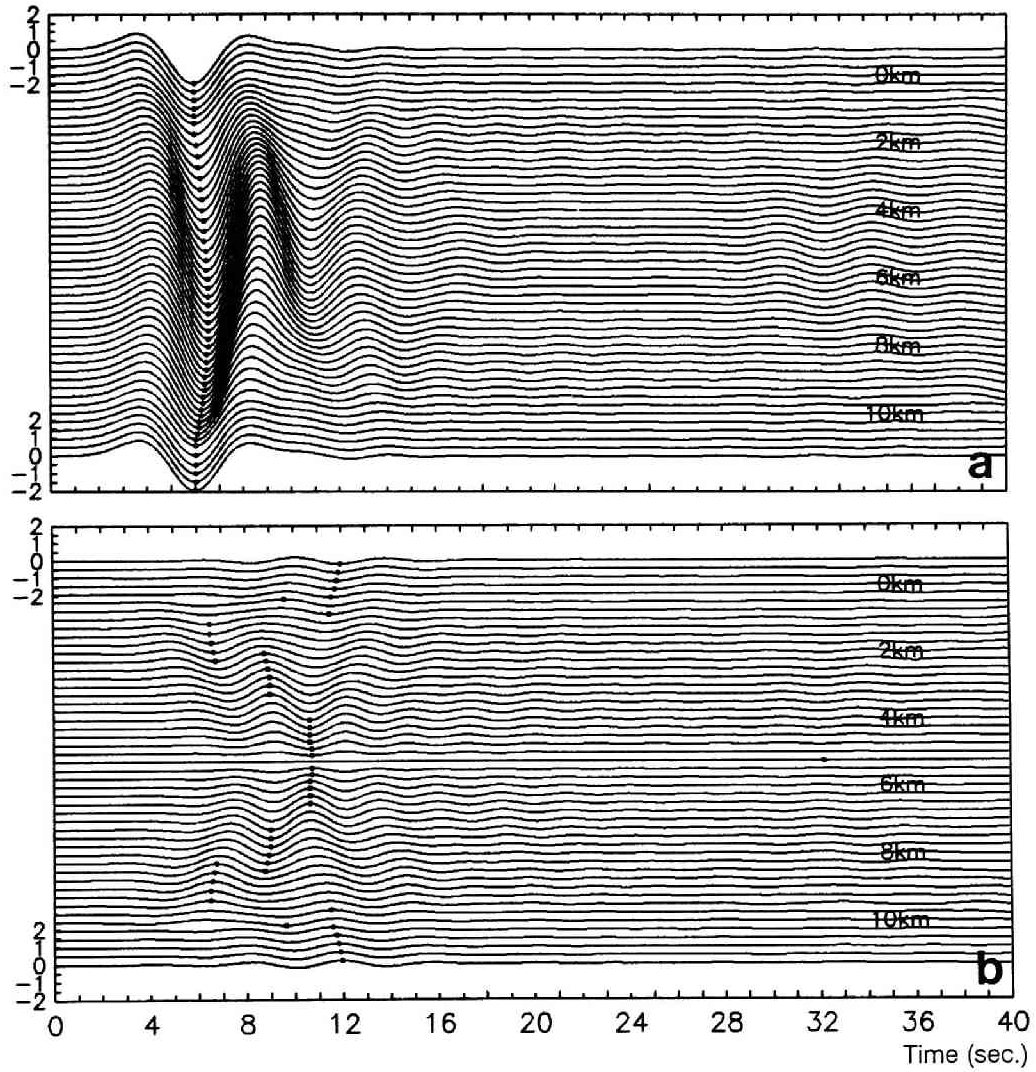

Figure 5.13: The responses of the type 1 basin for a Ricker wavelet of 0.167 Hz (6 seconds). The other conditions are the same as in Figure 5.11.

One is the fundamental mode whose phase velocity is about 0.9 km/sec with dominant vertical motion. The other is the first higher mode whose phase velocity is about 1.8 km/sec with dominant horizontal motion. Due to these two modes of Rayleigh waves the response becomes complex, but still the duration is less than about 20 seconds.

Lower frequency input (f_c=0.167 Hz, i.e., 6 seconds) gives again very weak interaction between incident wave and the valley, as shown in Figure 5.13.

It is found that a considerable difference exists between our results and those of Bard and Bouchon (1980b). In Figure 6 of their paper no clear Rayleigh waves can be seen in either horizontal or vertical components. It seems strange because the fundamental and first higher modes of Rayleigh waves are clearly seen in Figure 1 of their paper for P wave incidence. As shown later, the fundamental mode of Rayleigh waves for P wave incidence calculated here appears similarly to that for SV wave incidence. After checking carefully both our results and theirs, it is found that the responses for SV wave incidence obtained by Bard and Bouchon (1980b) are severely contaminated by scattered waves from neighboring fictitious structures because of their choice of insufficient periodicity length L.

In principle, the periodicity length L should be large enough so that the scattered waves from fictitious structures appear outside the time-window. This requires that $L \geq T \cdot v$, where T is the time-window size (i.e., calculated duration) and v is the velocity of the scattered wave. Since scattered P waves decay quickly and therefore affect the response negligibly, L=100 km is used which is large enough to prevent contamination by scattered S and Rayleigh waves in the 40 seconds time-window. Bard and Bouchon (1980b) used the periodicity length L of 12.8 km for the type 2 valley. This means that Rayleigh waves radiated from the edges of the neighboring fictitious structures arrive at the basin of interest within one second. The responses of the type 2 valley in their paper were calculated using the same parameters but with two different L, 12.8 km and 112.8 km. The comparison revealed that the responses of the L=12.8 km case are indeed contaminated by the scattered waves from fictitious structures.

Figure 5.14 shows the responses of the type 1 basin for an incident SV wave with the angle of 30°, which exactly corresponds to the critical angle for the half-

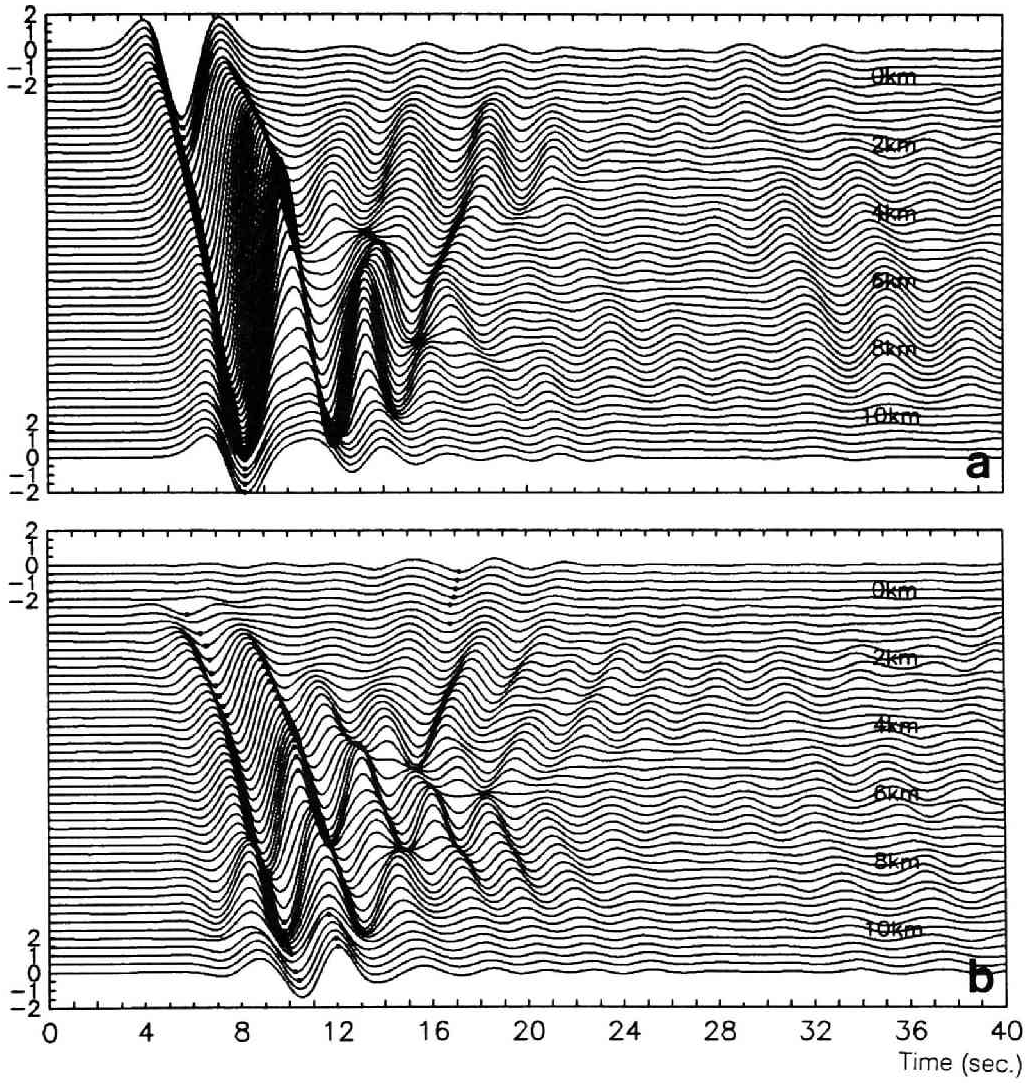

Figure 5.14: The responses of the type 1 basin for a critically (30°) incident SV wave. The other conditions are the same as in Figure 5.11.

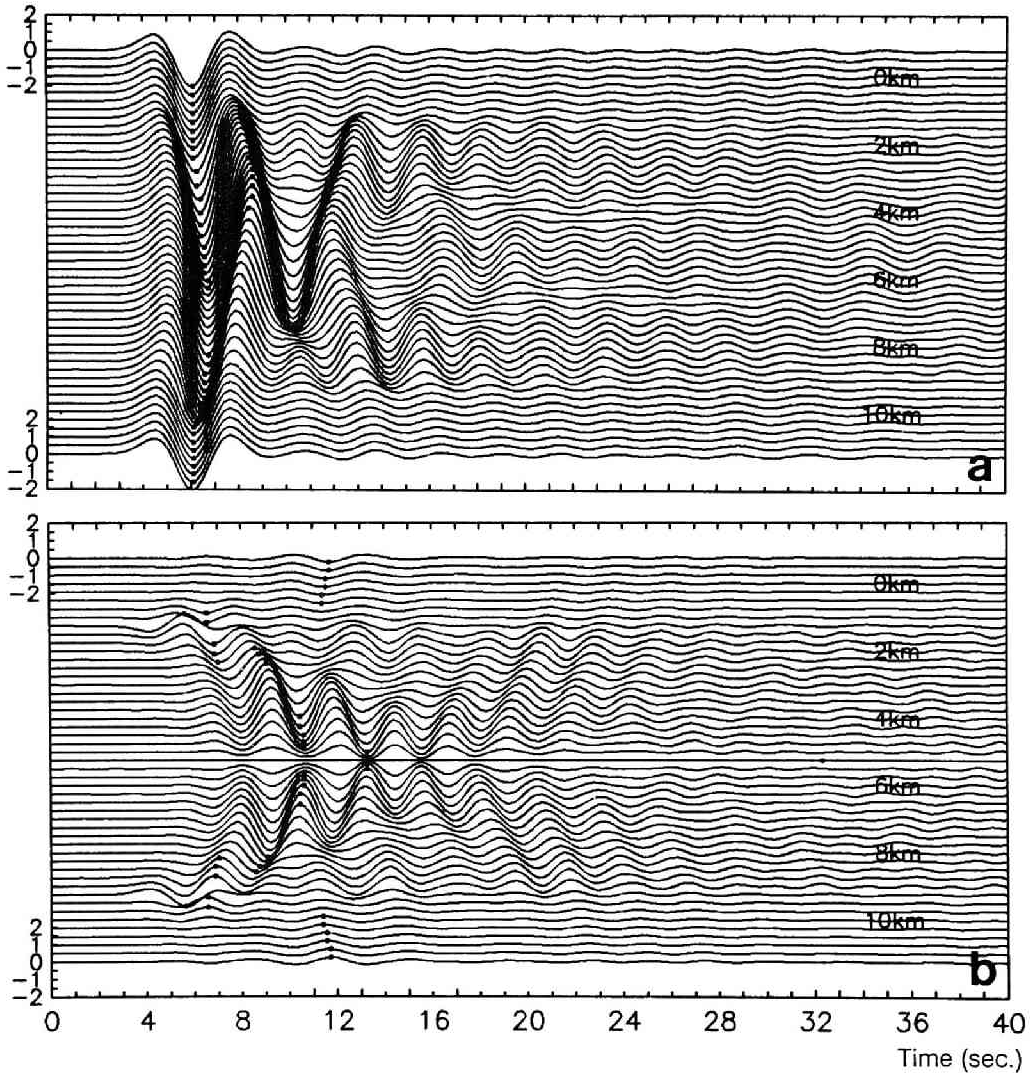

Figure 5.15: The responses of the type 1' basin for a vertically incident SV wave. The other conditions are the same as in Figure 5.11.

space. The peak amplitude of the direct wave, which is equal to –3.46 at the horizontal surface, looks almost the same throughout the basin. However, the second peak, which starts from about 2, gradually grows as the wave propagates toward the rear-side edge, and finally reaches its maximum of about 8. This large second peak may be due to the constructive interference of i) a Rayleigh wave whose phase velocity is 2.0 km/sec, ii) an inhomogeneous P wave whose apparent velocity is also 2,0 km/sec, and iii) refracted and reverberated SV waves. It is found that the inhomogeneous P wave must play an important role since this large amplification occurs only at or just over the critical incidence. The wave that arrives at about 30 seconds in the top trace of Figure 5.14 is the inhomogeneous P wave radiated from the adjacent basin. This fictitious arrival offers another evidence of the strong involvement of the inhomogeneous P wave.

The response of the type 1' basin, shown in Figure 5.15, is again similar to those for the type 1 basin.

5.4.4 P wave incidence

It is of little practical importance to study the responses for P wave incidence, however, it is worth while from a theoretical point of view. Time-histories of the first 20 seconds for the type 1 basin due to a vertically incident P wave are plotted in Figures 5.16 and 5.17. As mentioned earlier, later arrivals in the vertical component are very similar to those for SV wave incidence.

5.4.5 Rayleigh wave incidence

The responses of the type 1 basin to a Rayleigh wave incoming from the left were also investigated. Figures 5.18 and 5.19 show the surface responses due to an incident Rayleigh wave with the characteristic frequency f_c of 0.25 Hz (4 seconds) and 0.5 Hz (2 seconds), respectively.

At f_c=0.25 Hz, the second peak becomes about 8 times larger than the incident amplitude. The dispersion generates successive peaks and yields the maximum duration of about 20 seconds near the right edge. In case of a higher frequency input, the response becomes more complex, mainly due to the existence of two

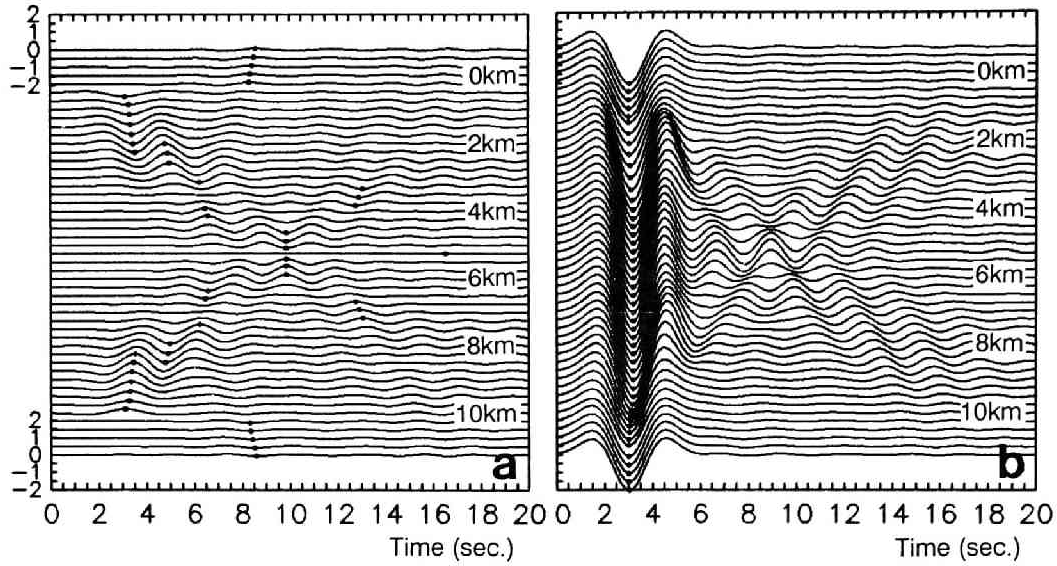

Figure 5.16: Time histories of horizontal (in-plane) component (a) and vertical component (b) of the type 1 basin for a vertically incident P wave. The characteristic frequency of a Ricker wavelet is 0.25 Hz (4 seconds). Only the first 20 seconds are shown since the amplitude of the later part is small.

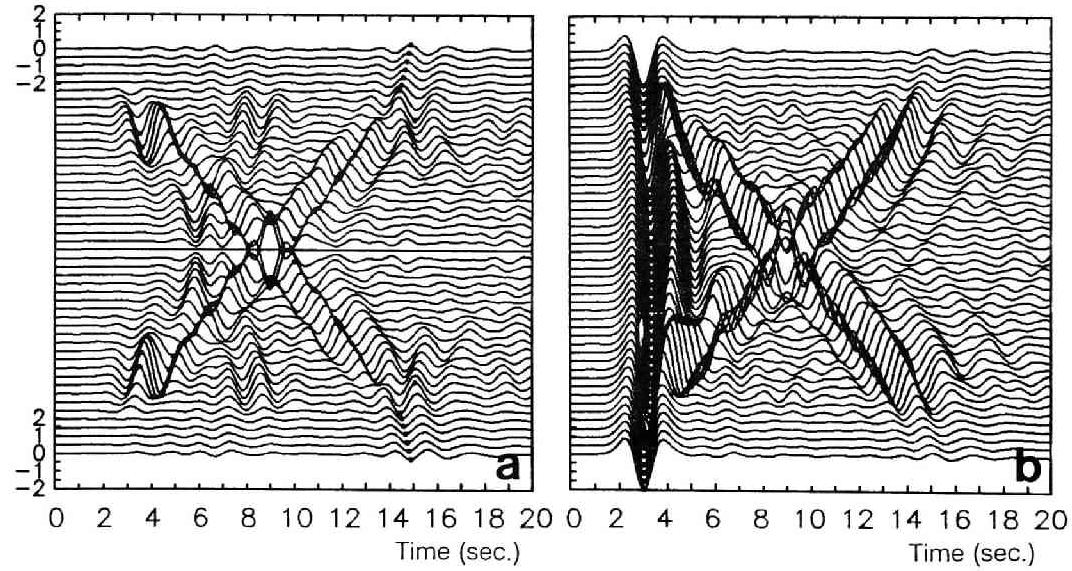

Figure 5.17: The responses of the type 1 basin for a Ricker wavelet of 0.5 Hz (2 seconds). The other conditions are the same as in Figure 5.16.

Rayleigh wave modes. The very late arrivals in Figure 5.18b may be due to the numerical inaccuracy at higher frequencies.

5.5 A deep basin structure with a soft layer

Through the detailed study of the response of a deep basin structure, it is found that although surface waves travel large distances, their effect on the duration is expected to be 20 seconds at most for the assumed model parameters. Another important difference between the theoretical and observed results is in the pattern of amplitude decay. While the calculated records show monotonically decreasing coda, the observed records at CDAO show two distinctive phases before and after about 75 seconds whose maximum amplitudes are almost the same (Figure 5.4).

It has been shown that the lateral variation of the soft surface layer in Mexico City cannot generate a ground motion with a very long duration (Kawase, 1987; Bard *et al.*, 1988). The response will converge rapidly to that of a plane horizontal layer as the distance between an observation point and the irregularity increases. Thus we cannot attribute the possible cause of the observed long duration solely to the irregularity of the surface layer. However, if the irregularity of the surface layer is coupled with the irregularity in the deeper structure, the results may be different. Because the surface waves generated by the deeper structure may be amplified and their propagation speeds may be slowed down when they encounter a shallower surface layer, they may appear with large amplitude at a much later time from the direct waves. This may be the case in Mexico City since its sedimentary basin consists of many layers (Marsal and Graue, 1969; Muris, 1978). To study the validity of this hypothesis, a deep basin structure with a soft surface layer is assumed.

5.5.1 A model

The assumed model is shown in Figure 5.20 as the type 2 basin. The shear wave velocity and the thickness of the soft layer are set to 0.25 km/sec and 0.25 km. The soft layer covers half of the basin. Although the shear wave velocity of the uppermost clay layer of the Mexico City valley is considered to be less than

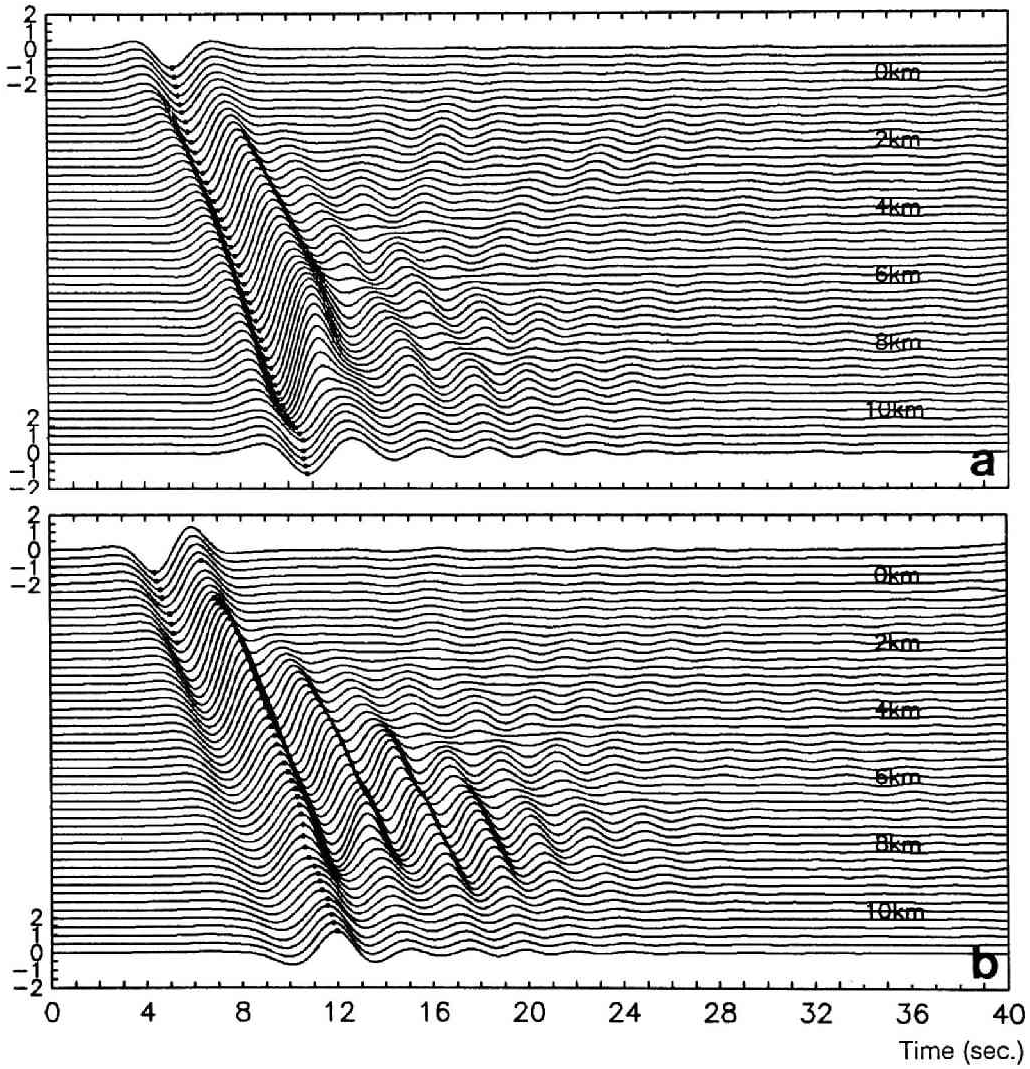

Figure 5.18: Time histories of horizontal (in-plane) component (**a**) and vertical component (**b**) of the type 1 basin for an incident Rayleigh wave. The characteristic frequency of a Ricker wavelet is 0.25 Hz (4 seconds). The response is normalized by the horizontal amplitude of an incident Rayleigh wave.

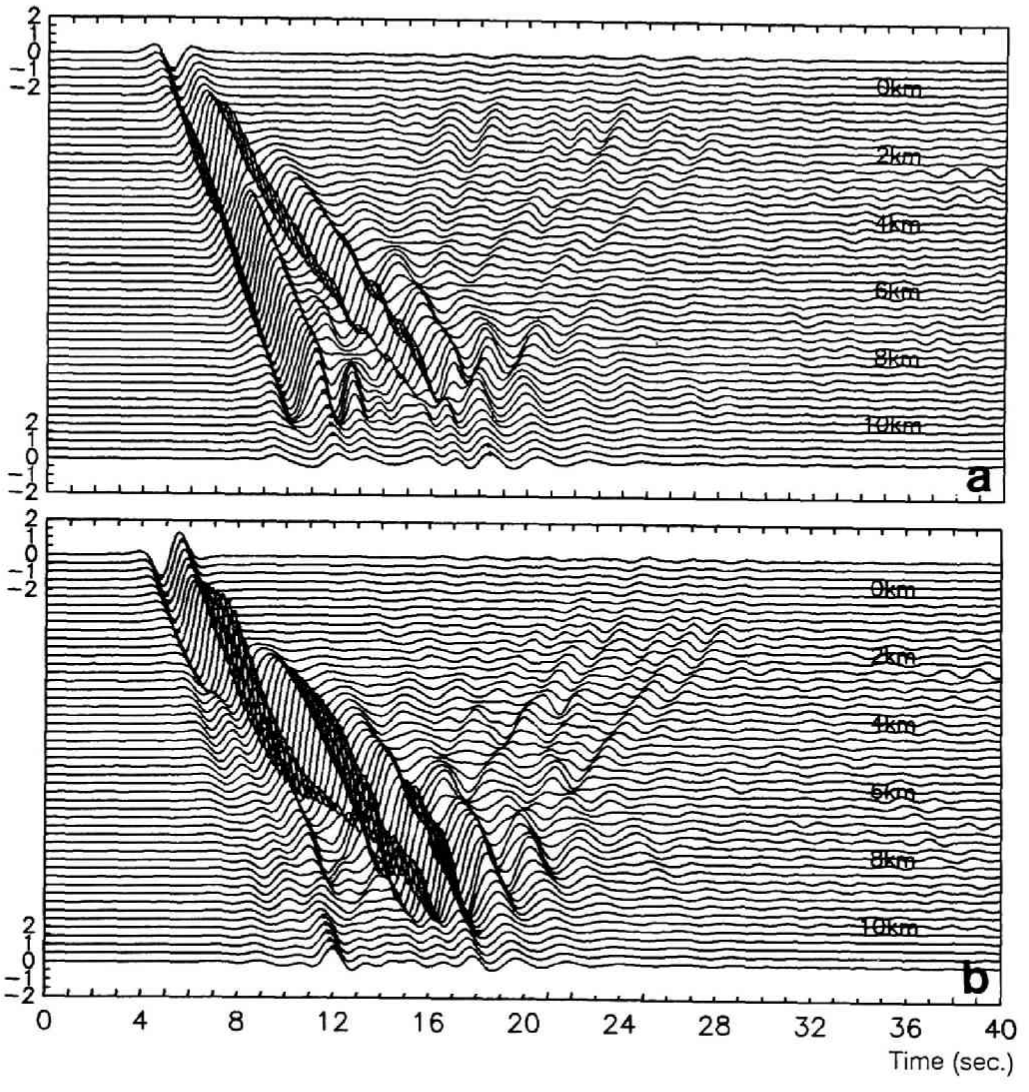

Figure 5.19: The responses of the type 1 basin for a Ricker wavelet of 0.5 Hz (2 seconds). The other conditions are the same as in Figure 5.18.

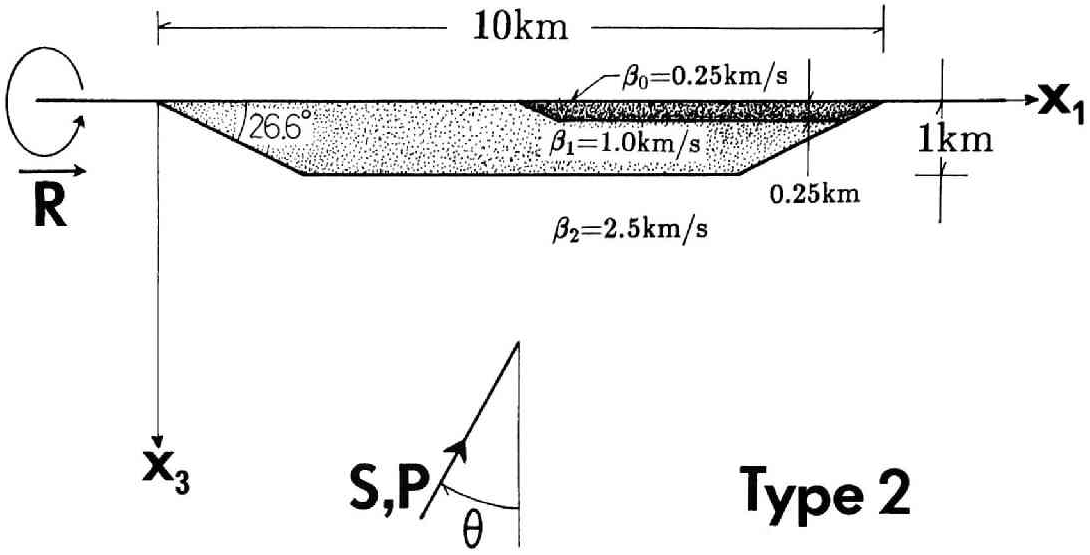

Figure 5.20: A deep basin structure with a soft surface layer. This type 2 basin has a softer layer which covers half of the basin surface. The depth of this layer is 0.25 km and its shear wave velocity is 0.25 km/sec. The other conditions are the same as the type 1 basin.

0.1 km/sec as shown in Figure 5.2, 0.25 km/sec is a practical limit imposed by the computer time needed to apply our method. The frequency increment in the DWBEM is decreased to 0.0125 Hz to accommodate the expected long duration. The rest of the parameters are the same as before.

5.5.2 SH wave incidence

First the response by a vertically incident SH wave is examined. Figure 5.21 shows the surface response of the type 2 basin for a Ricker wavelet of f_c=0.25 Hz (4 seconds). The surface waves that hit the left edge of the soft layer are clearly propagating back and forth in the similar manner to those in Figure 5.6, but with much lower apparent velocity and larger amplitude. It should be noted, however, that the amplitude, the predominant period, and the group velocity of the surface waves propagating from left to right are quite different from those propagating from right to left. This shows the importance of the deeper structure beneath the soft surface layer and the boundary configuration at the edges.

The calculated duration is comparable to those observed in Mexico City even though a Ricker wavelet is used as an input motion. Note that two distinctive phases exist, namely, the reverberated SH waves which last for less than 20 seconds

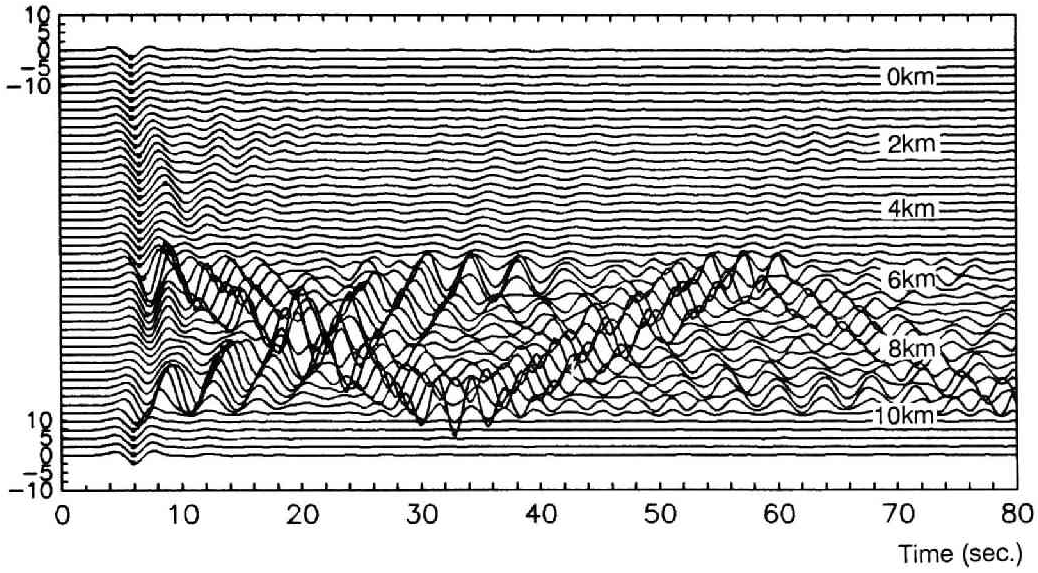

Figure 5.21: The responses of the type 2 basin for a vertically incident SH wave with the characteristic frequency of 0.25 Hz (4 seconds). The amplitude scale is expanded from ± 2 to ± 10 to focus on the wave propagation in the soft-layered zone. The Love wave appears 25 seconds after the first motion near the right edge of the basin. Note that the characteristics of the Love waves generated at the left and right edges are apparently different.

and the surface waves which appear 25 seconds after the first arrival near the edges and last for more than 50 seconds. The amplitude of the surface waves comparable to or even greater than that of the reverberated SH waves makes the synthetic time-histories similar to those observed at CDAO.

5.5.3 SV wave incidence

Next the case for a vertically incident SV wave is shown in Figure 5.22. The apparent velocity of the Rayleigh wave is much higher than that of the Love wave shown in Figure 5.21. The amplitude of the Rayleigh wave is somewhat smaller than that of the Love wave so that the propagation of the Rayleigh wave is not as clear as that of the Love wave. Despite these differences, the duration and the amplitude of the later arrivals relative to the first arrival show similar characteristics to those for the SH wave case, and to those observed in Mexico City. Note that the amplitude of the Rayleigh wave propagating from left to right is much larger than that propagating from right to left.

It should be mentioned that responses shown in Figure 5.22 are contaminated after about 50 seconds by the Rayleigh wave arrivals from adjacent fictitious structures since the periodicity length L (=100 km) is chosen for a time-window of 40 seconds, not 80 seconds. Although the contamination seems insignificant judging from the amplitude outside the soft layered zone, the waveforms after 50 seconds are unreliable.

5.6 Summary of the results and discussions

The responses of two types of soft basins for incident SH, SV, P, and Rayleigh waves in a two-dimensional elastic half-space are investigated with special reference to the long duration of strong motions observed in Mexico City during the Michoacan, Mexico earthquake of 1985. First the difficulty for simple one-dimensional models to reproduce the later part of the accelerogram observed in Mexico City is shown. Then the effect of a two-dimensional deep basin structure of a relatively large scale (10 km wide and 1 km deep) and a moderate impedance ratio (2.5) is studied. The results show that surface waves generated at the edges of the basin

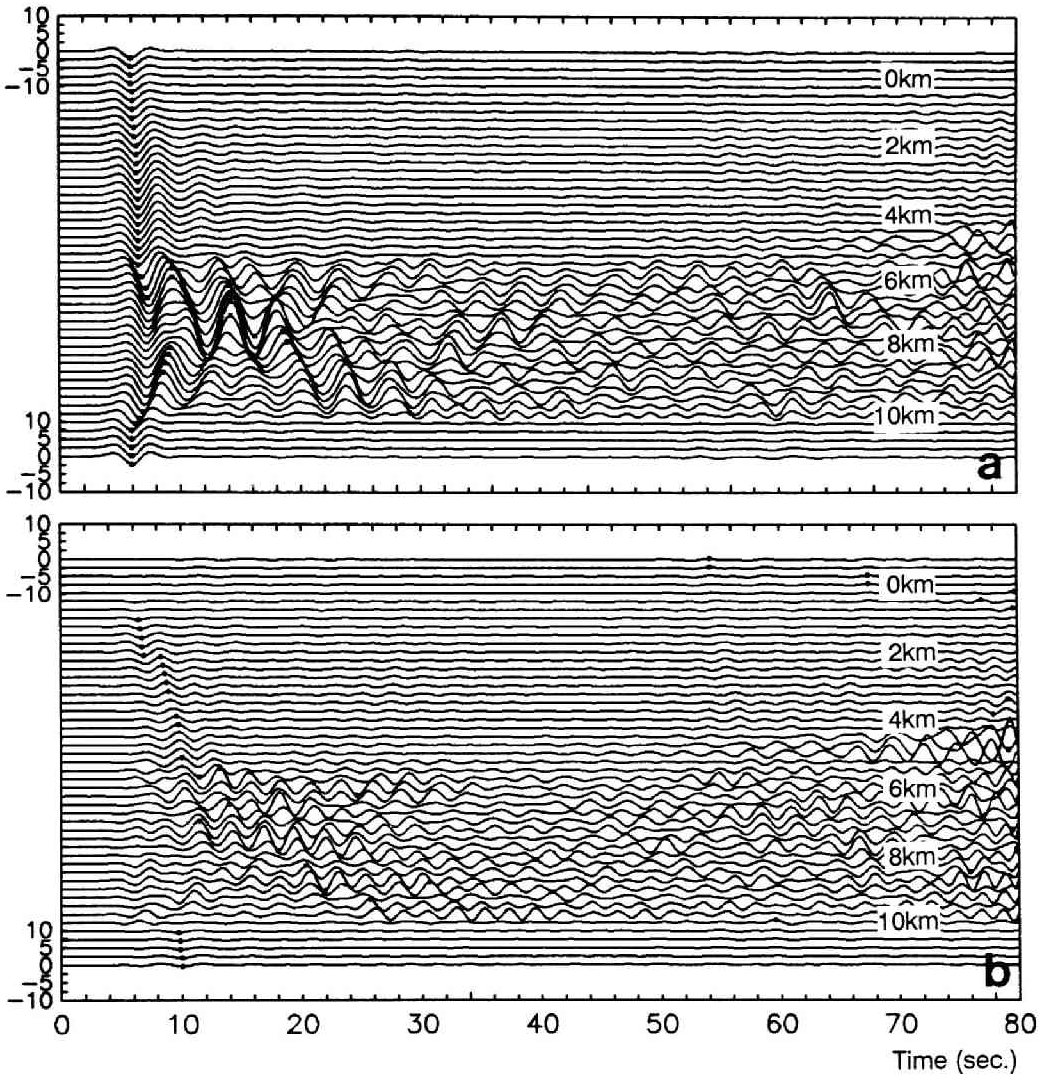

Figure 5.22: The responses of the type 2 basin for a vertically incident SV wave with the characteristic frequency of 0.25 Hz (4 seconds). Note that the amplitude of the Rayleigh wave generated at the right edge of the basin is much smaller than that generated at the left edge.

are clearly propagating inside the basin back and forth. However, the increase in duration by these surface waves is 20 seconds at most. Introducing another much softer layer inside the basin it is found that the calculated durations and envelope shapes become very similar to those observed because of the slowness of surface wave propagation. These theoretical studies suggest that the exceptionally long duration observed in Mexico City might be caused by a strong, constructive interaction of soft surface layers with a deep basin structure beneath the city.

The primary purpose of this chapter is to examine the possible cause of the extraordinary characteristics of strong ground motion observed at SCT and CDAO in Mexico City during the Michoacan, Mexico earthquake of 1985. It has been shown that one-dimensional S wave resonance of the soft surface layers yields smaller spectral values and shorter durations than those observed. It has also been shown that a deep basin structure generates surface waves which can lengthen the total duration up to 20 seconds, but that it fails to generate the observed duration with two distinctive phases. It is unlikely for the soft surface layer alone to cause the observed long duration even if the unrealistic variation of the thickness is assumed (Kawase, 1987; Bard *et al.*, 1988). However, the combination of a deep basin structure and a soft surface layer, as represented by the type 2 basin, reproduces successfully the extraordinary duration characteristics of the ground motion observed at CDAO. We found:

1. The duration calculated by the type 2 basin is comparable to the observed duration even though a Ricker wavelet was used as an input.

2. The time-histories near the left edge for SH wave incidence show two distinctive phases: the first one is due to the reverberated SH waves and the second one is due to Love waves. The observed records at CDAO also have two distinctive phases.

3. The amplitude of the later phase is comparable to or greater than that of the earlier phase, which is difficult to simulate by other models proposed so far.

The actual combined effect of a deep basin and soft shallow layers in Mexico City may be even stronger than that calculated by the type 2 basin, because the

number of actual layers and their shear wave velocity contrast may be greater than those assumed in the model.

The proposed model has the following limitations:

1. The type of an incident wave is oversimplified. Incident wave field may be more complex than the vertically incident plane S waves as assumed here.

2. The waveform of an input motion is oversimplified. The observed ground motions in the hill zone such as TACY have at least 40 seconds of duration.

3. The damping is neglected. If significant damping exists, surface waves cannot propagate over a large distance so that the calculated duration will decrease.

4. The long duration appears prominently on the record at CDAO, while the record at CDAF (Central de Abastos, Frigorífico), which is located about 1.3 km southeast of CDAO, does not share the same feature. If the hypothesis is true, we have to explain why these differences exist.

5. The actual ground may behave as a three-dimensional structure, rather than a two-dimensional one as assumed here.

Some of the above limitations are, however, probably not very serious. As for the type of incident wave, it has been shown that the general response characteristics of the type 2 basin are roughly the same for either SH or SV wave incidence. It is also true for inclined S wave and Rayleigh wave incidence, which was omitted here. These facts suggest that the type of an incident wave may be insignificant in our case. A similar statement was made by Campillo *et al.* (1988) for SH and L_g wave incidence. The simplicity of the input waveform is not a real limitation, because the effect of longer duration of an input motion is easily predictable as long as the response is linear.

The effect of the damping could be significant, especially if the shear wave velocity of the surface layer is very low. However, a relatively high shear wave velocity is assumed for the soft surface layer and the amplification and the duration are probably underestimated. Thus the effect of damping may be cancelled by the effect of softer surface layers. Furthermore, recent laboratory measurements reveal

that the soil of the soft surface layer in Mexico City shows very small damping coefficient of about 1% to 2% in the strain range up to 0.1% (Romo *et al.*, 1988).

The fourth point is more difficult to address at this time. However, it should be noted that the depths of the surface layer and the deeper layer are decreasing rapidly along the line from CDAO to CDAF (Sánchez-Sesma *et al.*, 1988). We believe that it may be possible to suppress the amplitude of later arrivals by a local variation of the layer thickness because later arrivals are restricted in a narrow frequency band and are vulnerable to scattering loss caused by a sudden thickness change. An example of such suppressing phenomena can be found in Baba *et al.* (1988).

Finally, the three-dimensional effects have not been fully investigated yet and should be done in near future. Even though our models are two dimensional, it is not feasible for current computers to perform a realistic simulation using detailed information of the Mexico City valley sediments because the lateral extent of the basin is too large ($\sim$10 km to $\sim$50 km) and the shear wave velocity contrast is too high ($\sim$0.04 km/sec to $\sim$2.5 km/sec).

A very important remark that the simulation in this chapter reveals is that the interaction between a soft surface layer with a deep basin structure is very strong if both of them share the predominant periods and therefore it is almost impossible to separate the effects of soft surface layers from those of deep basin structures. It should be noted that the information of the geological structure for very wide area, vertically and laterally, is needed for the quantitative simulation of strong ground motion in the sediment-filled valley on which large cities are resting, such as Tokyo, Osaka, Nagoya and most of major cities in Japan, San Francisco, Los Angeles, and capitals in Central and South America, not jsut Mexico City.

Chapter 6

Summary and Conclusions

The discrete wavenumber boundary element method (DWBEM) that combines the Green function calculated by the discrete wavenumber summation with the direct boundary element technique has been presented. The proposed method is proved to be efficient in computation and accurate and stable for wide frequency range. After solving simple topographic irregularities to understand the fundamental feature of the wave scattering phenomena, the author applies the method to the actual ground in order to scrutinize the possible cause of the extraordinary features observed during the recent major earthquakes. The work done in the previous chapters can be summarized as follows.

In Chapter 2, the DWBEM is fully described for both two- and three-dimensional wave field. Analytical evaluation of the element integration is formulated. A economical technique of the Green function evaluation that makes full use of the Hilbert transform relationship between real part and imaginary part of the Green function is briefly mentioned. As a result of a combination of the direct BEM and the discrete wavenumber Green function, many advantages, namely, efficiency in computation, flexibility for boundary configurations, and the accuracy and the stability of the solution even in high frequency range, are achieved. The applications in the following three chapters prove these advantages of the DWBEM. It is mentioned that the DWBEM is best suited for analyses of periodic structures or randomly inhomogeneous media.

In Chapter 3, time-domain responses of canyons and a ridge subject to incident SH, SV, P and Rayleigh waves with a Ricker wavelet shape are studied. The DWBEM is proved to have a strong applicability to various types of irregularities and incident waves for wide frequency range. Since the conventional BIEM or BEM requires considerable computational effort for in-plane problems, one can hardly find results expressed in time domain for even simple topography so far. In addi-

tion conventional techniques tend to lose their stability and give inaccurate results in higher frequency range, which also prevents us from calculating the time-domain response because even small amount of error in frequency domain will result in the violation of causality in time domain. On the other hand the DWBEM is efficient in computation, thanks to the discrete wavenumber Green functions, and accurate and stable even in high frequency range, thanks to the exact element integration and direct constraint for boundary conditions. Thus it gives us the causal and physically explainable time-histories as shown here. We can learn a great deal from such time-histories on the fundamental characteristics of wave scattering by topographic irregularities.

In case of a canyon, the diffracted waves originated at the edges of the canyon are observed propagating along the canyon surface with the apparent velocity of S or P waves, which may be called the *creeping* waves. For SV wave incidence Rayleigh waves generated at the edges of the canyon carry significant portion of energy outward, while for SH wave incidence the direct and reflected waves play a major role. In case of a ridge, the diffracted waves are increasing their amplitude as they propagate along the ridge surface owing to the convex shape of the ridge surface. For in-plane problems the *creeping* Rayleigh wave dominates over other types of *creeping* waves on the ridge surface. It is pointed out that the amplitude fluctuation in frequency domain does not always mean that in time domain because different arrival time of wavelets results in the fluctuation in spectral amplitude even if each wavelet propagates with the same shape and amplitude. The time-domain response contains both amplitude and phase spectral information, and therefore expresses more complete physical picture of the wave propagation phenomena.

In Chapter 4, the DWBEM is applied to the actual ground problem in which heavy damage concentration was observed during the Whittier Narrows, California earthquake of 1987. It is intended to show the possibility that this anomalous damage concentration is due to the amplification by the topographic irregularity when SV waves are near-critical incidence. First the author examined the accelerograms obtained at the USGS station nearest to downtown Whittier and conclude that the dominantly east-west motion observed at the station is due to the influence of the building in which accelerograms were recorded. We next demonstrate

that strong ground motions recorded by 12 stations in the epicentral area show a polarization direction pattern that is primarily SV-type, which is consistent with a simple thrust fault located at the hypocenter. Then we calculated the response of a two-dimensional hill with the height 0.3 km and the width 2.4 km to i) a plane SV wave with a nearly critical angle of incidence, ii) a horizontal line force, iii) a Haskell-type 2D dislocation source, and iv) a Bouchon-type 2D multiple crack source. The results show that the amplification due to the hill relative to the flat surface is more than 1.5 for all the source models. Since this amplification is nearly independent of the source type and spectrum, it is concluded that the combined effect of the topographic irregularity and critically incident SV waves might be responsible for the concentration of damage observed during the Whittier Narrows earthquake.

In Chapter 5, the responses of two types of soft basins for incident SH, SV, P, and Rayleigh waves in a two-dimensional elastic half-space are investigated with special reference to the long duration of strong motions observed in Mexico City during the Michoacan, Mexico earthquake of 1985. First the difficulty for simple one-dimensional models to reproduce the later part of the accelerogram observed in Mexico City is shown. Then the effect of a two-dimensional deep basin structure of a relatively large scale (10 km wide and 1 km deep) and a moderate impedance ratio (2.5) is studied. The results show that surface waves generated at the edges of the basin are clearly propagating inside the basin back and forth. However, the increase in duration is 20 seconds at most. Introducing another much softer layer inside the basin it is found that the calculated durations and envelope shapes become very similar to those observed because of the slowness of surface wave propagation. These theoretical studies suggest that the exceptionally long duration observed in Mexico City might be caused by a strong, constructive interaction of soft surface layers with a deep basin structure beneath the city.

The results presented in this study shows additional evidences that the effects of the surface and subsurface irregularities are substantially large and that it is difficult to predict the damage pattern without considering their effects. At the same time, it is found that the precise information on the geological properties and structures is crucial for the quantitative simulation of observed records and hence

the definitive prediction for design-basis strong ground motions. One important remark that this study reveals is that the interaction between soft surface layers with deep basin structures is stronger than previously thought so that the attempt to separate the effect of soft surface layers from deep basin structures may lead us to a completely different type of phenomena from the observation.

Since the advent of supercomputers it has become feasible to calculate the response of a soft basin with large scale for wide frequency range. Recently, even the analyses of three-dimensional soft basin structures have been attempted (e.g., Jiang and Kuribayashi, 1988; Etgen and Yomogida, 1988; Sato, 1989; Eshraghi and Dravinski, 1989; Mossessian and Dravinski, 1989). On one hand of the study we should develop more efficient computational technique which can represent the complicated irregularity of the earth and can produce accurate results without much precautions. It is desirable to include the effects of source and path as well since the separation of these effects from those of local site geology is not always possible (e.g., Hisada *et al.*, 1988; Sato, 1989). On the other hand of the study we should proceed further the current programs of the observation network scattered throughout the soft basin in the population concentrated area. In such programs it is recommended that the measurement should be done by seismometers which have wide frequency range and good amplitude and phase linearity. The correct absolute-time recording system is also necessary for the travel-time information. Finally, we should gather information further on the geological structures underneath the target city as wide and deep as possible without which we cannot predict design-basis strong ground motions. Both of them are crucial for the seismic hazard mitigation for future earthquakes.

References

Aki, K. (1988). Local site effect on ground motion, in *Earthquake engineering and soil dynamics II — Recent advances in ground-motion evaluation*, J. Lawrence Von Thun, Editor, Am. Soc. Civil Eng. Geotechnical Special Publication **20**, 103-155.

Aki, K. and K. L. Larner (1970). Surface motion of a layered medium having an irregular interface due to incident plane SH waves, *J. Geophys. Res.*, **75**, 933-954.

Aki, K. and P. G. Richards (1980). *Quantitative seismology: Theory and methods*, W. H. Freeman and Co., San Fransisco, California, U.S.A.

Anderson, J. G., P. Bodin, J. N. Brune, J. Prince, S. K. Singh, R. Quaas, and M. Ofiate (1986). Strong ground motion from the Michoacan Mexico earthquake, *Science*, **233** 1043-1049.

Apsel, R. J. and J. E. Luco (1983). On the Green's functions for a layered half-space, part II, *Bull. Seism. Soc. Am.*, **73**, 931-951

Baba, K., Y. Inoue, and T. Nishigaki (1988). Dynamical behavior of a slightly alluvial basin due to plane wave turbulences, *Proc. of 9th World Conf. Earthquake Eng.*, **2**, Tokyo, Japan, 689-694.

Banaugh, R. P. and W. Goldsmith (1963). Diffraction of steady acoustic waves by surfaces of arbitrary shape, *J. Acoust. Soc. Am.*, **35**, 1590-1601.

Bard, P.-Y. (1982). Diffracted waves and displacement field over two dimensional elevated topographies, *Geophys. J. R. astro. Soc.*, **71**, 731-760.

Bard, P.-Y. and M. Bouchon (1980a). Seismic response of sediment-filled valleys, Part 1: The case of incident SH waves, *Bull. Seism. Soc. Am.*, **70**, 1263-1286.

Bard, P.-Y. and M. Bouchon (1980b). Seismic response of sediment-filled valleys, Part 2: The case of incident P and SV waves, *Bull. Seism. Soc. Am.*, **70**, 1921-1941.

Bard, P.-Y. and M. Bouchon (1985). The two-dimensional resonance of sediment-

filled valleys, *Bull. Seism. Soc. Am.*, **75**, 519-541.

Bard, P.-Y., M. Campillo, F. J. Cháves-Garcia, and F. J. Sánchez-Sesma (1988). The Mexico earthquake of September 19, 1985 — A theoretical investigation of large- and small-scale amplification effects in the Mexico City valley, *Earthquake Spectra*, 4, 609-633.

Bard, P.-Y. and B. E. Tucker (1985). Ridge and tunnel effects: comparing observation with theory, *Bull. Seism. Soc. Am.*, **75**, 905-922.

Bard, P.-Y. and B. E. Tucker (1987). Predictability of sediment site amplification: a case study, preprint.

Benites, R. and K. Aki (1989). Boundary integral-Gaussian beam method for seismic wave scattering: SH waves in two-dimensional media, *J. Acoust. Soc. Am.*, **86**, 375-386.

Boore, D. M. (1970). Love waves in nonuniform wave guides: finite difference calculations, *J. Geophys. Res.*, **75**, 1512-1527.

Boore, D. M. (1972). A note on the effect of simple topography on seismic SH wave, *Bull. Seism. Soc. Am.*, **62**, 275-284.

Boore, D. M. K. L. Larner, and K. Aki (1971). Comparison of two independent method for the solution of wave scattering problems: response of sedimentary basin to vertically incident SH waves, *J. Geophys. Res.*, **76**, 558-569.

Boore, D. M., S. C. Harmsen and S. T. Harding (1981). Wave scattering from a step change in surface topography, *Bull. Seism. Soc. Am.*, **71**, 117-125.

Bouchon, M. (1973). Effect of topography on surface motion, *Bull. Seism. Soc. Am.*, **63**, 615-632.

Bouchon, M. (1978). A dynamic source model for the San Fernando earthquake, *Bull. Seism. Soc. Am.*, **68**, 1555-1576.

Bouchon, M. (1985). A simple complete numerical solution to the problem of diffraction of SH waves by an irregular surface, *J. Acoust. Soc. Am.*, **77**, 1-5.

Bouchon, M. and K. Aki (1977). Discrete wave-number representation of seismic-source wave field, *Bull. Seism. Soc. Am.*, **67**, 259-277.

Brady, A. G., E. C. Etheredge, and R. L. Porcella (1988a). The Whittier Narrows, California earthquake of October 1, 1987 — Preliminary assessment of strong ground motion records, *Earthquake Spectra*, **4**, 55-74.

Brady, A. G., P. N. Mork, and L. C. Seekins (1988b). Processed strong-motion records, Whittier Narrows, California earthquake October 1, 1987, *U.S. Geol. Surv. Open File Report*, No.88-354, U.S.A.

Brebbia, C. A. (1978). *The boundary element method for engineers*, Pentech Press, London.

Campillo, M. and M. Bouchon (1985). Synthetic SH seismograms in a laterally varying medium by the discrete wavenumber method, *Geophys. J. R. astro. Soc.*, **83**, 307-317.

Campillo, M., P.-Y. Bard, F. Nicollin, and F. J. Sánchez-Sesma (1988). The Mexico earthquake of September 19, 1985 — The incident wave field in Mexico City during the great Michoacan Earthquake and its interaction with deep basin, *Earthquake Spectra*, **4**, 591-608.

Chapman, C. H. and J. A. Orcutt (1985). The computation of body wave synthetic seismograms in laterally homogeneous media, *Review of Geophysics*, **23**, No.2, 15-163

Das, S. and K. Aki (1977). Fault plane with barriers: a versatile earthquake model, *J. Geophys. Res.*, **82**, 5658-5670.

Davis, L. L., and L. R. West (1973). Observed effects of topography on ground motion, *Bull. Seism. Soc. Am.*, **63**, 283-298.

Drake, L. A. (1972). Love and Rayleigh waves in non-horizontal layered media, *Bull. Seism. Soc. Am.*, **62**, 1241-1258.

Dravinski, M. (1982). Influence of interface depth upon strong ground motion, *Bull. Seism. Soc. Am.*, **72**, 596-614.

Dravinski, M. and T. K. Mossessian (1987). Scattering of plane harmonic P, SV and Rayleigh waves by dipping layers of arbitrary shape, *Bull. Seism. Soc. Am.*, **77**, 212-235.

Eshraghi, H., and M. Dravinski (1989). Scattering of plane harmonic SH, SV, P, and Rayleigh waves by non-axisymmetric three-dimensional canyons: a wave function expansion approach, *Earthquake Eng. Struct. Dyn.*, **18**, 983-998.

Etgen, J. and Yomogida, K. (1988). Three dimensional wave propagation in the Los Angeles basin, *EOS*, Abstract of AGU fall meeting, **69**, No.44, 1325-1325

Franz, W. (1954). Über die Greenschen Funktionen des Zylinders und der Kugel, *Z. Naturforsch*, **9a**, 705-716.

Frazer, L. N. and J. F. Gettrust (1984). On a generalization of Filon method and the computation of the oscillatory integrals of seismology, *Geophys. J. R. astro. Soc.*, **76**, 461-481

Fukushima, Y. and H. Kawase (1986). The irregular ground analysis of Mexico City focused on the time-varying characteristics of the strong ground motion records for the Michoacan earthquake of 1985, *Proc. of 7th Japan Earthquake Engineering Symposium*, Tokyo, Japan, 325-330.

Fukuwa, N., T. Sato, H. Kawase and S. Nakai (1985). Effects of surface irregularities on strong ground motion, *Proc. of 31st Japan Structural Engineering Symposium*, Tokyo, Japan, 1-10.

Fuyuki, M. and Y. Matsumoto (1980). Finite difference analysis of Rayleigh wave scattering at a trench, *Bull. Seism. Soc. Am.*, **70**, 2051-2069.

Geli, L., P.-Y. Bard, and B. Jullien (1988). The effect of topography on earthquake ground motion: a review and new results, *Bull. Seism. Soc. Am.*, **78**, 42-63.

Griffith, D. W. and G. A. Bollinger (1979). The effect of Appalachian Mountain topography on seismic waves, *Bull. Seism. Soc. Am.*, **69**, 1081-1105.

Hart, G. C., J. Kariotis, and J. L. Noland (1988). The Whittier Narrows, California earthquake of October 1, 1987 — Masonry building performance survey, *Earthquake Spectra*, **4**, 181-196.

Haskell, N. (1964). Total energy and energy spectral density of elastic wave radiation from propagating faults, *Bull. Seism. Soc. Am.*, **54**, 1811-1842.

Hayashi, Y. and H. Katsukura (1990). Effective time-domain soil-structure interaction analysis based on FFT algorithm with causality condition, *Earthquake*

Eng. Struct. Dyn., **19**, in press.

Hauksson, E., L. Jones, T. Davis, L. K. Hutton, A. G. Brady, P. Reasenberg, A. J. Michael, R. F. Yerkes, P. Williams, G. Reagor, C. Stover, A. Bent, A. Shakal, E. Etheredge, R. Porcella, C. Bufe, M. Johnston, and E. Cranswick (1988). The Whittier Narrows earthquake in the Los Angeles metropolitan area, California, *Science*, **239**, No.4846, 1409-1412.

Hisada, Y., S. Yamamoto, and S. Tani (1988). Analysis of strong ground motion of plain and basin being composed of soft soil by fault model and boundary element method, *Proc. of 9th World Conf. Earthquake Eng.*, **2**, Tokyo, Japan, 701-706.

Hong, T. L. and D. V. Helmberger (1978). Glorified optics and wave propagation in non planar structures, *Bull. Seism. Soc. Am.*, **68**, 1313-1330.

Idriss, I. M. and H. B. Seed (1968). Analysis of ground motions during the 1957 San Francisco earthquake, *Bull. Seism. Soc. Am.*, **58**, 2013-2032.

Ilan, A. (1977). Finite difference modelling for P-pulse propagation in elastic media with arbitrary polygonal surface, *J. Geophys.*, **43**, 41-58.

Instituto de Ingenieria de la UNAM (1985). *El temblor del 19 de septiembre de 1985 y sus efectos en las construcciones de la Ciudad de Mexico*, UNAM, Mexico City, Mexico.

Ishii, H. and M. M. Ellis (1970). Multiple reflection of plane SH waves by a dipping layer, *Bull. Seism. Soc. Am.*, **60**, 15-28.

Ishimoto, M. (1932). Comparaison accélérométrique des secousses sismiques dans deux parties de la ville de Tôkyô, *Bull. Earthquake Research Inst.*, Univ. of Tokyo, **10**, 171-187.

Izumi, M., H. Katsukura, and S. Ohno (1988). Studies on separation and synthesis of nonstationary seismic waves using FFT technique based on hyperfunction theory, *J. of Structural and Construction Engineering*, Trans. of AIJ, **390**, 18-26

Jaime, A. and M. P. Romo (1988). The Mexico earthquake of September 19, 1985 — Correlations between dynamic and static properties of Mexico City clay,

Earthquake Spectra, 4, 787-804.

Jiang, T. and E. Kuribayashi (1988). The three-dimensional resonance of axisymmetric sediment-filled valleys, *Soils and Foundations*, **28**, No.4, 130-146.

Jones, B. G. and C. N. Nicolaides (1988). The Whittier Narrows, California earthquake of October 1, 1987 — Buildings at risk, *Earthquake Spectra*, **4**, 35-42.

Jones, L. and E. Hauksson (1988). The Whittier Narrows, California earthquake of October 1, 1987 — Seismology, *Earthquake Spectra*, **4**, 43-53.

Kawase, H. (1987). Irregular ground analysis to interpret time-characteristics of strong motion recorded in Mexico City during 1985 Mexico earthquake, in *Ground Motion and Engineering Seismology*, A. S. Cakmak, Editor, Development in Geotechnical Engineering **44**, Elsevier Scientific Publishing Co., Amsterdam, Holland, 467-476.

Kawase, H. (1988). Time-domain response of a semicircular canyon for incident SV, P, and Rayleigh waves calculated by the discrete wavenumber boundary element method, *Bull. Seism. Soc. Am.*, **78**, 1415-1437.

Kawase, H., K. Yoshida, S. Nakai, and Y. Koyanagi (1982). Dynamic Response of structure on a layered medium — A dipping layer and a flat layer —, *Proc. of 6th Japan Earthquake Engineering Symposium*, Tokyo, Japan, 1641-1648.

Kawase, H., T. Sato, S. Sato, and G. Tanaka (1985). Analytical and observational study on seismic scattering property of a site with geological irregularity, *Proc. of 8th Int. Conf. Structural Mechanics in Reactor Technology*, Paris, France, **K(a)**, 1-6.

Kawase, H. and K. Aki (1989a). Economical seismogram synthesis using causality with FFT, *Bull. Seism. Soc. Am.* **79**, 1294-1299.

Kawase, H. and K. Aki (1989b). A study on the response of a soft basin for incident S, P, and Rayleigh waves with special reference to the long duration observed in Mexico City, *Bull. Seism. Soc. Am.* **79**, 1361-1382.

Kawase, H. and K. Aki (1990). Topography effect at the critical SV-wave incidence: possible explanation of damage pattern by the Whittier Narrows, California earthquake of 1 October 1987, *Bull. Seism. Soc. Am.* **80**, 1-22.

Kitagawa, Y. and Y. Matsushima (1982). Evaluation of dynamic ground characteristics and seismic microzoning, *Proc. of 6th Japan Earthquake Engineering Symposium*, Tokyo, Japan, 33-40.

Kobayashi, H., K. Seo and S. Midorikawa (1986). Report on seismic microzoning studies of the Mexico earthquake of September 19, 1985, *Tokyo Institute of Technology*, Tokyo, Japan.

Kobori, T. and Y. Shinozaki (1978). Dynamic soil-structure interaction under topographical site condition, *Proc. of 5th Japan Earthquake Engineering Symposium*, Tokyo, Japan, 489-496.

Kohketsu, K. (1987). 2-D reflectivity method and synthetic seismograms in irregularly layered structures, Part I: SH-wave generation, *Geophys. J. R. astro. Soc.*, **89**, 821-838.

Kubo, K. and R. Isoyama (1980). Damage to buried utility pipes in the 1978 Miyagiken-Oki earthquake, *Proc. of 7th World Conf. Earthquake Eng.*, **8**, Istanbul, Turkey, 225-232.

Lamb, H. (1904). On the propagation of tremors over the surface of elastic solid, *Phil. Trans. Royal Soc. London*, A, **203**, 1-42.

Lee, V. W. (1982). A note on the scattering of elastic plane waves by a hemispherical canyon, *Soil Dyn. Earthquake Eng.*, **1**, 122-129.

Leyendecker, E. V., L. M. Highland, M. Hopper, E. P. Arnold, P. Thenhaus, and P. Powers (1988). The Whittier Narrows, California earthquake of October 1, 1987 — Early results of isoseismal studies and damage surveys, *Earthquake Spectra*, **4**, 1-10.

Lin, Y. K. (1976). *Probabilistic theory of structural dynamics*, Robert E. Krieger Publishing Co., Huntington, New York, U.S.A.

Marsal, R. J. and R. Graue (1969). *El subsuelo de Lago de Texcoco, el hundimiento de la Ciudad de Mexico y Proyecto Texcoco*, Nabor Carrillo Conmemorative Volume, Secretaria de Hacienda y Credito Publico, Mexico.

Mossessian, T. K., and M. Dravinski (1989). Scattering of elastic waves by three-dimensional surface topographies, *Wave Motion*, **11**, 579-592.

Moczo, P., P.-Y. Bard, and I. Pšenčik (1987). Seismic response of two-dimensional absorbing structures by the ray method, *J. Geophy.*, **62**, 38-49.

Muris, R. C. (1978). *Ciudad de Mexico, el subsuelo y la ingenieria de cimentaciones en la area urbana del Valle de Mexico*, Simposio 10 de marzo de 1978, SMMS, Mexico.

Newmark, N. M. and E. Rosenblueth (1971). *Fundamentals of earthquake engineering*, Prentice-Hall, Inc., Englewood Cliffs, New Jersey, U.S.A.

Nowack, R. and K. Aki (1984). The two-dimensional Gaussian beam synthetic method: testing and applications, *J. Geophys. Res.*, **89**, 7797-7819.

Ohtsuki, A. and K. Harumi (1983). Effect of topography and subsurface inhomogeneities on seismic SV waves, *Earthquake Eng. Struct. Dyn.*, **11**, 441-462.

Ohtsuki, A. H. Yamahara, and T. Tazoh (1984). Effect of lateral inhomogeneity on seismic waves, Part II: Observations and analysis, *Earthquake Eng. Struct. Dyn.*, **12**, 795-816.

Ovando-Shelley E., M. Mendoza and M. P. Romo (1988). The Mexico earthquake of September 19, 1985 — Deformability of Mexico City hard deposites under cyclic loading, *Earthquake Spectra*, **4**, 753-770.

Papoulis, A. (1962). *The Fourier integral and its applications*, McGraw-Hill, Berkeley, California, U.S.A.

Poceski, A. (1969). The ground effect of the Scopie July 26 1963 earthquake, *Bull. Seism. Soc. Am.*, **59**, 1-22.

Press, W. H., B. P. Flannery, S. A. Teukolski and W. T. Vetterling (1986). *Numerical recipes — the art of scientific computing*, Cambridge University Press, New York, U.S.A.

Quaas, R., J. Prince, E. Mena, M. Torres, L. Alcantara, P. Perez, D. Almora, G. Chavez, R. Delgado, C. Carmona and M. A. Onate (1985). Los dos acelerogramas del sismo de septiembre 19 de 1985, Obtenidos en la Central de Abastos en Mexico D. F., *Instituto de Ingenieria, UNAM*, Informe IPS-10C, Mexico City, Mexico.

Ricker, N. H. (1977). *Transient waves in visco-elastic media*, Elsevier Scientific Publishing Co., Amsterdam, Holland.

Romo, M. P. and H. B. Seed (1986). Analytical modeling of dynamic soil response in the Mexico earthquake of Sept. 19, 1985, in *The Mexico Earthquakes — 1985*, M. A. Cassaro and E. M Romero, Editors, Am. Soc. Civil Eng., 148-162.

Romo, M. P., A. Jaime, and D. Reséndiz (1988). The Mexico earthquake of September 19, 1985 — General soil conditions and clay properties in the valley of Mexico, *Earthquake Spectra*, **4**, 731-752.

Rosenblueth, E. (1960). The earthquake of 28 July in Mexico City, *Proc. of 2nd World Conf. Earthquake Eng.*, Tokyo, Japan, 359-378.

Sánchez-Sesma, F. J. (1978). Ground motion amplification due to canyons of arbitrary shape, *Proc. of 2nd Int. Conf. on Microzonation*, San Fransisco, U.S.A., 729-738.

Sánchez-Sesma, F. J. and J. A. Esquivel (1979). Ground motion on alluvial valley under the incident plane SH waves, *Bull. Seism. Soc. Am.*, **69**, 1107-1120.

Sánchez-Sesma, F. J., M. A. Bravo, and I. Herrera (1985). Surface motion of topographical irregularities for incident P, SV, and Rayleigh waves, *Bull. Seism. Soc. Am.*, **75**, 263-269.

Sánchez-Sesma, F. J., S. Chávez-Pérez, M. Suárez, M. A. Bravo, and L. E. Pérez-Rocha (1988). The Mexico earthquake of September 19, 1985 — On the seismic response of the valley of Mexico, *Earthquake Spectra*, **4**, 569-589.

Sato, T. (1989). A hybrid approach for theoretical seismograms using thin layer element and axisymmetric finite element and its application to simulation of earthquake ground motions, *Doctoral thesis, Tohoku University*, Sendai, Japan.

Schiff, A. J. (1988). The Whittier Narrows, California earthquake of October 1, 1987 — Response of lifelines and their effect on emergency response, *Earthquake Spectra*, **4**, 339-366.

Seed, H. B., R. V. Whitman, H. Dezfulian, R. Dobry, and I. M. Idriss (1972). Soil conditions and building damage in the 1967 Caracas earthquake, *J. Am. Soc. Civil Eng., SM division*, **98**, 787-806.

Seed, H. B., H. M. Romo, J. I. Sun, A. Jaime, and J. Lysmer (1988). The Mexico earthquake of September 19, 1985 — Relationship between soil conditions and earthquake ground motions, *Earthquake Spectra*, **4**, 687-729.

Sezawa, K. (1930). Possibility of the free-oscillations of the surface-layer excited by the seismic-waves, *Bull. Earthquake Research Inst.*, Univ. of Tokyo, **8**, 1-11.

Shakal, A., M. J. Huang, C. E. Ventura, D. L. Parke, T. Q. Cao, R. W. Sherburne, and R. Blazquez (1987). CSMIP strong-motion records from the Whittier Narrows, California earthquake of October 1, 1987, *Calif. Div. Mines and Geol. CSMIP Report*, No.OSMS 87-05, Sacramento, California, U.S.A.

Shakal, A., M. J. Huang, and T. Q. Cao (1988). The Whittier Narrows, California earthquake of October 1, 1987 — CSMIP strong motion data, *Earthquake Spectra*, **4**, 75-100.

Sills, L. B., (1978). Scattering of horizontally polarized shear waves by surface irregularities, *Geophys. J. R. astro. Soc.*, **54**, 319-348.

Singh, S. K., J. Lermo, T. Dominguez, M. Ordaz, J. M. Espinosa, E. Mena, and R. Quaas (1988). The Mexico earthquake of September 19, 1985 — A study of amplification of seismic waves in the valley of mexico with respect to a hill zone site, *Earthquake Spectra*, **4**, 653-673.

Smith, W. D. (1975). The application of finite element analysis to body wave propagation problems, *Geophys. J. R. astro. Soc.*, **42**, 747-768.

Takizawa, H. (1982). Work done by earthquake ground shaking upon various types of dynamic systems, *Proc. of 6th Japan Earthquake Engineering Symposium*, Tokyo, Japan, 1065-1072.

Tezcan, S. S., H. B. Seed, R. V. Whitman, N. Serff, J. T. Christian, H. T. Durgunoglu, and M. Yegian (1977). Resonant period effects in the Gediz, Turkey earthquake of 1970, *Earthquake Eng. Struct. Dyn.*, **5**, 157-179.

Thomson, W. T. and T. Kobori (1963). Dynamical compliance of rectangular foundations on an elastic half-space, *J. Appl. Mech.*, Am. Soc. Mech. Eng., **30**, 579-584

Tierney, K. (1988). The Whittier Narrows, California earthquake of October 1, 1987 — Social aspects, *Earthquake Spectra*, **4**, 11-23.

Trifunac, M. D. (1971). Surface motion of a semi-cylindrical alluvial valley for incident plane SH waves, *Bull. Seism. Soc. Am.*, **61**, 1755-1770.

Trifunac, M. D. (1972). Interaction of a shear wall with the soil for incident plane SH waves, *Bull. Seism. Soc. Am.*, **62**, 63-83.

Trifunac, M. D. (1973). Scattering of plane SH waves by a semi-cylindrical canyon, *Earthquake Eng. Struct. Dyn.*, **1**, 267-281.

Trifunac, M. D. (1988). The Whittier Narrows, California earthquake of October 1, 1987 — Note on peak accelerations during the 1 and 4 October earthquakes, *Earthquake Spectra*, **4**, 101-113.

Tucker, B. E., J. L. King, D. Hatzfeld, and I. L. Nersesov (1984). Observations of hard-rock site effects, *Bull. Seism. Soc. Am.*, **74**, 121-136.

Vidale, J. E. (1989). Influence of focal mechanism on peak accelerations of strong motions of the Whittier Narrows, California earthquake and an aftershock, *J. Geophys. Res.*, **94**, 9607-9613.

Vidale, J. E. and D. V. Helmberger (1988). Elastic finite-difference modeling of the 1971 San Fernando, California earthquake *Bull. Seism. Soc. Am.*, **78**, 122-141.

Wald, D., P. G. Somerville, and L. J. Burdick (1988). The Whittier Narrows, California earthquake of October 1, 1987 — Simulation of recorded accelerations *Earthquake Spectra*, **4**, 139-156.

Wolf, J. P. (1985). *Dynamic soil-structure interaction*, Prentice-Hall, Inc., Englewood Cliffs, New Jersey, U.S.A.

Wong, H. L. (1979). Diffraction of P, SV and Rayleigh waves by surface topographies, *Dept. of Civil Eng., Univ. of Southern California*, No.CE79-05, Los Angeles, California, U.S.A.

Wong, H. L. (1982). Effect of surface topography on the diffraction of P, SV, and Rayleigh Waves, *Bull. Seism. Soc. Am.*, **72**, 1167-1183.

Wong, H. L. and M. D. Trifunac (1974). Surface motion of a semi-elliptical alluvial valley for incident plane SH waves, *Bull. Seism. Soc. Am.*, **64**, 1389-1408.

Wong, H. L. and P. C. Jennings (1975). Effect of canyon topography on strong ground motion, *Bull. Seism. Soc. Am.*, **65**, 1239-1257.

Yamanaka, H., K. Seo, and T. Samano (1989). Effects of sedimentary layers on surface-wave propagation, *Bull. Seism. Soc. Am.*, **79**, 631-644.

Zahradnik, J. and L. Urban, (1984). Effect of a simple mountain range on underground seismic motion, *Geophys. J. R. astro. Soc.*, **79**, 167-183.

Zeevaert, L. (1964). Strong ground motions recorded during earthquakes of May the 11th and 19th 1962 in Mexico City, *Bull. Seism. Soc. Am.*, **54**, 209-231.

Appendix A

Wave Field by Fault Models in Chapter 4

In Chapter 4 the author uses four different types of sources for the analysis of the topography near downtown Whittier. The incident and reflected wave field by a plane SV wave incidence can be found in any textbooks for the elastic wave theory. The displacement field due to a horizontal line force has already been described in equation (2.33). The theoretical expressions for two kinematic fault models, the Haskell-type uniform slip model and the Bouchon-type multiple crack model, are summarized here for readers' quick reference. The complete procedures for deriving the following equations can be found in Haskell (1964) and Bouchon and Aki (1977) for the former and Bouchon (1978) for the latter.

Consider an in-plane shear dislocation in a two-dimensional half-space where rupture starts at (x_1^s, x_3^s) and propagates over a plane surface of length L_f as shown in Figure A.1. The displacement at $(x_1, 0)$ due to such a dislocation source can be expressed by using the discrete wavenumber method as

$$u_i = \sum_{n=-\infty}^{\infty} e^{-ik_n x_1} \sum_{l=1}^{2} R_{li}(n) e^{-i(k_n x_1^s - \eta_n x_3^s)} \int_0^{L_f} D(\xi, \omega) e^{-iB_n \xi} d\xi \qquad \text{(A.1)}$$

where,

$$\begin{aligned}
R_{11}(n) &= \{\sin 2\theta (2k_n^2 - k_\alpha^2) - \cos 2\theta k_n \nu_n\} \frac{2k_n \gamma_n}{L\Delta(k_n)} \\
R_{13}(n) &= \{\sin 2\theta (2k_n^2 - k_\alpha^2) - \cos 2\theta k_n \nu_n\} \frac{-(2k_n^2 - k_\beta^2)}{L\Delta(k_n)} \\
R_{21}(n) &= \{2 \sin 2\theta k_n \gamma_n + \cos 2\theta (2k_n^2 - k_\beta^2)\} \frac{(2k_n^2 - k_\beta^2)}{L\Delta(k_n)} \\
R_{23}(n) &= \{2 \sin 2\theta k_n \gamma_n + \cos 2\theta (2k_n^2 - k_\beta^2)\} \frac{2k_n \nu_n}{L\Delta(k_n)},
\end{aligned} \qquad \text{(A.2)}$$

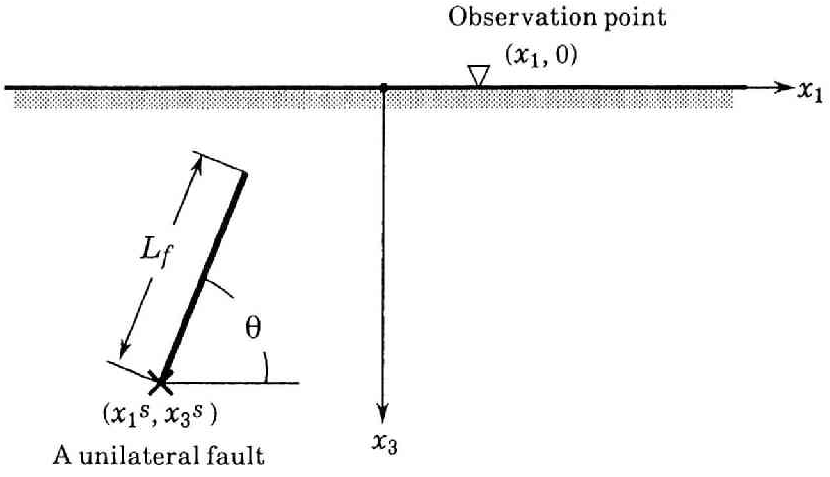

Figure A.1: Dimensions of the assumed 2D fault characterized by its length L_f, the dip angle θ, and the hypocenter (x_1^s, x_3^s). Only one unilateral fault is assumed here since a bilateral fault or any multiple-segment faults can be represented as the sum of two or more unilateral faults.

$$\eta_n = \begin{cases} \nu_n & \text{if } l = 1 \\ \gamma_n & \text{if } l = 2\,, \end{cases} \tag{A.3}$$

$$B_n = k_n \cos\theta + \eta_n \sin\theta\,. \tag{A.4}$$

The definition of wavenumbers such as k_β or k_n and the Rayleigh function $\Delta(k_n)$ can be found in equation (2.18), equation (2.21), and equation (A). The last integral term in equation (A.1) is the so-called dynamic source factor $S_n(\omega)$ which is the function of the rupture propagation pattern along the fault surface.

The rupture process in the Haskell-type fault with the ramp function can be expressed in time-domain as

$$D(\xi,t) = \begin{cases} 0 & \text{for } 0 < t < \xi/c \\ \frac{D_\infty}{T_{rise}}(t - \frac{\xi}{c}) & \text{for } \xi/c \le t \le \xi/c + T_{rise} \\ D_\infty & \text{for } \xi/c + T_{rise} < t\,, \end{cases} \tag{A.5}$$

in which c denotes the rupture velocity, D_∞ the final slip, and T_{rise} the rise time. Taking the Fourier transform of the above $D(\xi,t)$ and performing the integration along the fault surface analytically, we obtain the dynamic source factor for the 2D Haskell-model as follows:

$$S_n(\omega) = -\frac{D_\infty(1-e^{-i\omega T_{rise}})}{\omega^2 T_{rise}} \frac{c}{B_n c - i\omega} \left\{ e^{(B_n c - i\omega)\frac{L_f}{c}} - 1 \right\} . \qquad \text{(A.6)}$$

The rupture process in the Bouchon-type fault can be represented as a semi-elliptic crack that grows linearly with time until the rupture stops. The slip function in time-domain is then

$$D(\xi,t) = \begin{cases} 0 & \text{for } 0 < t < \xi/c \\ \frac{D_\infty(center)}{L_f}\sqrt{\xi(ct-\xi)} & \text{for } \xi/c \le t \le L_f/c \\ \frac{D_\infty(center)}{L_f}\sqrt{\xi(L_f-\xi)} & \text{for } L_f/c < t\,, \end{cases} \qquad \text{(A.7)}$$

where $D_\infty(center)$ denotes the final slip at the center of the crack. The direct evaluation of the Fourier transform and the subsequent integration from the above expression is not so easy that Bouchon (1978) divides the contour of the semi-ellipse into M arcs and replaces each arc by the linear segment. The resulting form of the dynamic source factor for a single crack can be expressed as follows:

$$\begin{aligned} S_n(\omega) \;=\; & \frac{i}{\omega}\left\{ e^{-\frac{i\omega L_f}{c}} \left[\sum_{m=1}^{M-1} e^{B_n m \Delta L_f} d_m \left(\frac{c^2}{\omega^2 e_m + i\omega B_n c} - \frac{c}{i\omega B_n} \right) \right.\right. \\ & \left. - \frac{b_1 c}{i\omega B_n} - \frac{b_M c}{B_n{}^2 c - i\omega B_n} e^{B_n L_f} \right] \\ & - \sum_{m=1}^{M-1} \frac{c^2}{\omega^2 e_m + i\omega B_n c} \\ & \left. + \frac{b_M c^2}{\omega^2 + i\omega B_n c} \right\} , \end{aligned} \qquad \text{(A.8)}$$

where,

$$\begin{aligned} a_m &= \frac{D_\infty(m) - D_\infty(m-1)}{\Delta L_f} \\ b_m &= \frac{m D_\infty(m-1) - (m-1) D_\infty(m)}{L_f} \end{aligned}$$

$$
\begin{aligned}
d_m &= b_{m+1} - b_m \\
e_m &= M/m \\
\Delta L_f &= L_f/M\,. \qquad \text{(A.9)}
\end{aligned}
$$

In these equations $D_\infty(m)$ represents the final slip at the end tip of the m-th segment.

The numbers of total segments M should be a function of the maximum frequency considered and the accuracy required. It is found that 20 segments are enough for the purpose of the study here. The response by the multiple cracks used in Chapter 4 can be obtained as the superposition of contribution from each crack. It should be noted that the final solution in Bouchon (1978), which is presented as equation (11) in his paper, contains zero-value terms such as f_m and g_m that are omitted from equation (A.8).